

Tomographic particle image velocimetry and its application to turbulent boundary layers

Gerrit E. Elsinga

Tomographic particle image velocimetry and its application to turbulent boundary layers

PROEFSCHRIFT

ter verkrijging van de graad van doctor
aan de Technische Universiteit Delft,
op gezag van de Rector Magnificus prof. dr. ir. J.T. Fokkema,
voorzitter van het College voor Promoties,
in het openbaar te verdedigen op dinsdag 3 juni 2008 om 12:30 uur

door

Gerrit Einte ELSINGA
ingenieur luchtvaart- en ruimtevaart techniek
geboren te Groenlo

Dit proefschrift is goedgekeurd door de promotoren:

Prof. dr. ir. P.G. Bakker

Prof. dr. F. Scarano

Samenstelling promotiecommissie:

Rector Magnificus,	voorzitter	
Prof. dr. ir. P.G. Bakker,	Technische Universiteit Delft,	promotor
Prof. dr. F. Scarano,	Technische Universiteit Delft,	promotor
Prof. dr. ir. J. Westerweel,	Technische Universiteit Delft	
Prof. dr.-ing. dr.-ing. habil. C. Tropea,	Technische Universität Darmstadt	
Prof. dr. ir. W. van de Water,	Technische Universiteit Eindhoven	
Prof. dr. M. Stanislas,	Université des Sciences et Technologies de Lille	
B. Wieneke, M.Sc.,	LaVision, Göttingen	

Copyright © 2008 G.E. Elsinga

All rights reserved.

ISBN 978-90-9023158-7

Printed by PrintPartners Ipskamp B.V.

Contents

Summary	viii
Samenvatting	x
1 Introduction	1
1.1 Views on turbulence in relation to experimental techniques	1
1.2 Aim of the thesis	2
1.3 Outline of the thesis	3
PART I: Development of the experimental technique	4
2 Particle image velocimetry	5
2.1 Planar PIV	5
2.1.1 Working principle of PIV	5
2.1.2 Particle imaging	6
2.1.3 Evaluation of particle image displacement	7
2.1.4 Stereoscopic PIV	9
2.2 Overview of existing 3D PIV techniques	10
2.2.1 Holographic PIV	10
2.2.2 Scanning PIV	11
2.2.3 3D Particle tracking velocimetry	12
3 Tomographic particle image velocimetry	15
3.1 Motivation for development	15
3.2 Principles of Tomographic-PIV	15
3.3 Tomographic reconstruction techniques	17
3.4 3D calibration and calibration correction	23
4 Theoretical and numerical assessment	27
4.1 Estimate for the number of ghost particles	27
4.2 Parametric study	29
4.3 Three-dimensional simulation	35
4.4 Conclusions	38
5 Experimental assessment	39
5.1 Circular cylinder wake flow	39
5.2 Experimental setup	40
5.3 Accuracy of the tomographic reconstruction	42

5.4 Assessment of the velocity measurement	46
5.5 Quantitative comparison with Stereoscopic PIV	48
5.6 Instantaneous velocity results	51
5.7 Conclusions	55
6 Challenges in the application of PIV to supersonic flows	57
6.1 Particle lag	57
6.2 Refractive index effects	59
PART II: Experimental investigation of turbulent boundary layers	64
7 Coherent structures in the turbulent boundary layer	65
7.1 Terminology	65
7.2 Structural elements in the outer layer	67
7.2.1 Overview	67
7.2.2 Supersonic boundary layers	72
7.2.3 Turbulence modeling using coherent structures	73
7.3 Visualization of coherent structures	74
7.3.1 Vortex detection	74
7.3.2 Conditional averaging by linear stochastic estimation	75
8 Low speed turbulent boundary layer ($Re_\theta = 1900$)	77
8.1 Introduction	77
8.2 Experimental setup	78
8.3 Instantaneous flow organization	81
8.3.1 Vortical structures	81
8.3.2 Low speed zones and hairpin packets	85
8.3.3 Ejections and sweeps	88
8.4 Conclusions	91
9 On the life of a hairpin	93
9.1 Introduction	93
9.2 Experimental setup	94
9.3 Results	96
9.3.1 Life	98
9.3.2 Birth	102
9.3.3 Death	102
9.4 Conclusions	103
10 Supersonic turbulent boundary layer ($Re_\theta = 34,000$, $M = 2.1$)	107
10.1 Introduction	107
10.2 Experimental setup	108
10.3 Results	111

10.3.1 Instantaneous flow structure	111
10.3.2 Hairpins	115
10.3.3 Large-scale and very large-scale motion	118
10.4 Discussion	126
10.5 Conclusions	128
11 Overall conclusions and outlook	129
11.1 Conclusions	129
11.2 Outlook	131
References	133
List of publications	139
Acknowledgements	141
Curriculum Vitae	142

Summary

The first part of the thesis describes the principles of a novel 3D PIV system based on the illumination, recording and reconstruction of tracer particles within a three-dimensional measurement volume. The technique makes use of several simultaneous views of the illuminated particles and their three-dimensional reconstruction as a light intensity distribution by means of optical tomography. The technique is therefore referred to as Tomographic Particle Image Velocimetry (Tomographic-PIV, chapter 3). The reconstruction is performed with the MART algorithm, yielding a 3D array of light intensity discretized over voxels. The reconstructed tomogram pair is then analyzed by means of 3D cross-correlation with an iterative multigrid volume deformation technique, returning the three-component velocity vector distribution over the measurement volume. The principles and details of the tomographic algorithm are discussed and a parametric study is carried out by means of a computer-simulated Tomographic-PIV procedure (chapter 4). The study focuses on the accuracy of the light intensity field reconstruction process. The simulation also identifies the most important parameters governing the experimental setup and the tomographic algorithm parameters, showing their effect on the reconstruction accuracy. A computer simulated experiment of a 3D particle motion field describing a vortex ring demonstrates the capability and potential of the proposed system with four cameras. The capability of the technique in real experimental conditions is assessed with the measurement of the turbulent flow in the near wake of a circular cylinder at a Reynolds number of 2700 based on the cylinder diameter (chapter 5). The assessment covers both the accuracy of the reconstruction and the returned velocity vectors. Furthermore, the challenges related to the application of PIV in supersonic flows will be discussed (chapter 6).

The Tomographic-PIV technique is applied in the second part of the thesis to study coherent structures in turbulent boundary layers. The first experimental investigation deals with the instantaneous three-dimensional flow organization in a low-speed (incompressible) turbulent boundary layer at $Re_\theta = 1900$ (chapter 8). A relatively large amount of data exists in literature at similar conditions, which allows a comparison of the results. In the lower half of the boundary layer, mainly asymmetric hairpin vortices and hairpin packet structures are observed, which agrees with earlier studies. It is shown that the alignment of hairpin vortex structures in streamwise as well as wall-normal direction yield important contributions to the instantaneous Reynolds shear stress. Further away from the wall a variety of individual vortex structures are found, which appear to be randomly distributed. The time evolution of the flow structures is visualized in a second experiment, in which the Tomographic-PIV technique is applied to nearly time-resolved image sequences recorded at 1.5 kHz (chapter 9). The growth and convection rates of the hairpin vortices are established, and examples of rare, highly dynamic events such as the birth and death of a hairpin vortex are presented. Finally the technique is applied to a high Reynolds number supersonic turbulent boundary layer ($Re_\theta = 34,000$; $M = 2.1$; chapter 10), for which no 3D quantitative visualizations of the coherent structures have been reported previously. The instantaneous results show a range of flow scales from individual hairpin vortices to hairpin packets and

very-large-scale low speed zones extending over at least three boundary layer thicknesses in streamwise direction (limited by the observation domain). The instantaneous hairpins and conditional averaged eddies appear to have sizes and shapes very similar to those found in the subsonic low Reynolds number boundary layer, when scaled with the boundary layer thickness δ . Low-pass filtering of the velocity volumes reveals the signatures of large-scale hairpins and streamwise vortices. These large-scale hairpins are observed to be aligned in the streamwise direction, creating the very-large-scale low speed zones, but also display a preferential alignment in spanwise direction along the 45 degrees diagonal with the respect to the streamwise direction.

Samenvatting

Het eerste deel van dit proefschrift beschrijft het principe van een nieuw 3D PIV systeem gebaseerd op de belichting, beeldopname and reconstructie van tracer-deeltjes in een drie dimensionaal meetvolume. Deze techniek maakt gebruik van verschillende simultane aanzichten van de verlichte deeltjes en van hun drie dimensionale reconstructie in de vorm van een intensiteitsverdeling doormiddel van tomografie. De techniek wordt daarom Tomographic Particle Image Velocimetry genoemd (Tomographic-PIV, hoofdstuk 3). Voor de tomografische reconstructie wordt het MART algoritme toegepast, wat resulteert in 3D lichtintensiteitsveld op discrete voxel elementen. Vervolgens wordt de drie-componenten snelheidsvector distributie in het volume gevonden door de analyse van het tomogram-paar met een iteratief multigrid cross-correlatie algoritme met window deformatie. De details van het tomografische algoritme worden verder uitgewerkt samen met een parametrische studie met behulp van computer simulaties van de experimentele procedure (hoofdstuk 4). Deze studie richt zich op de nauwkeurigheid van de reconstructie van de lichtintensiteitsverdeling. De simulaties identificeren ook de belangrijkste parameters en laten hun effect op de reconstructie zien. De simulatie van een 3D deeltjesverplaatsingsveld dat een werveling beschrijft, demonstreert de mogelijkheden van een Tomographic-PIV systeem met 4 cameras. De mogelijkheden van de techniek onder realistische experimentele condities wordt beoordeeld door middel van een meting van een turbulente stroming direct achter een cilinder bij een Reynoldsgetal van 2700 gebaseerd op de cilinderdiameter (hoofdstuk 5). Zowel de nauwkeurigheid van de reconstructie als van de gemeten snelheid wordt besproken. Voorts worden de specifieke uitdagingen betreffende de toepassing van PIV in supersonische stromingen besproken (hoofdstuk 6).

De Tomographic-PIV techniek is toegepast in het tweede deel van het proefschrift ter bestudering van coherente structuren in turbulente grenslagen. De eerste experimentele studie betreft de instantane driedimensionale stromingsorganisatie in een turbulente grenslaag bij lage snelheid (onsamendrukbaar) en $Re_\theta = 1900$ (hoofdstuk 8). Voor deze condities is een relatief grote hoeveelheid literatuur beschikbaar waarmee de resultaten vergeleken kunnen worden. In de onderste helft van de grenslaag worden voornamelijk asymmetrische haarspeldwervels en haarspeldwervel-pakketten gevonden, hetgeen in overeenstemming is met eerder werk. De resultaten laten zien dat de organisatie van haarspeldwervels in stromingsrichting, maar ook in de richting loodrecht op de wand, een belangrijke bijdrage levert aan de instantane Reynolds-schuifspanning. Verder van de wand af wordt een grotere variëteit aan individuele wervel structuren gevonden. Deze lijken wanordelijk verdeeld in de ruimte. De ontwikkeling van de coherente structuren in de tijd is gevisualiseerd in een tweede experiment, waarin de Tomographic-PIV techniek is toegepast bij een opnamefrequentie van 1,5 kHz (hoofdstuk 9), waarmee de stroming in de tijd te volgen is. De groei en de convectiesnelheid van de haarspeldwervels zijn bepaald en voorbeelden worden gegeven van zeldzame, zeer dynamische gebeurtenissen zoals de geboorte en de dood van een haarspeldwervel. Tot slot wordt de techniek toegepast op een supersonische turbulente grenslaag bij een hoog Reynoldsgetal ($Re_\theta = 34,000$; $M = 2.1$;

hoofdstuk 10) waarvoor tot nu toe nog geen 3D kwantitatieve visualisaties gerapporteerd zijn. De instantane resultaten laten een bereik van schalen in de stroming zien van individuele haarspeldwervels tot haarspeldwervel-pakketten en zeer lange structuren van lage snelheid die zich uitstrekken over tenminste drie grenslaagdikten in stromingsrichting (de observatie is gelimiteerd door de grootte van het meetvolume). Zowel de instantane haarspeldwervels als de conditioneel gemiddelde eddies hebben een grootte en vorm die sterk overeenkomen met die in de subsonische, laag Reynoldsgetal grenslaag wanneer deze geschaald worden met de grenslaagdikte δ . Na het laag-doorlaat filteren van het snelheidsveld worden de signaturen van grootschalige haarspeldwervels en wervels in stromingsrichting zichtbaar. Deze grootschalige haarspeldwervels lijken zich te ordenen langs lijnen in stromingsrichting, waarbij ze de zeer lange structuren van lage snelheid vormen. Bovendien vertonen ze ordening in de dwarsrichting langs de 45 graden diagonaal ten opzichte van de stromingsrichting.

Chapter 1

Introduction

One of the most important challenges in experimental fluid dynamics today is the ability to accurately measure the three-dimensional structure of turbulent flows. Turbulence is characterized by seemingly disorderly fluctuations and is of interest, not only as it remains one of the greatest unsolved problems in physics, but also because of its important implications to many engineering applications. In this respect one can think of the associated increase in mixing and wall shear stress (drag). Out of all turbulent flows, the boundary layer over a (flat) surface (figure 1.1) has perhaps received most attention, because of its effect on the drag of moving objects such as aircraft. The general perception, therefore, is that improved understanding of boundary layer turbulence may have potential for control strategies, which allow modifying the flow in order to reduce drag. Ultimately drag reduction will in turn reduce the fuel consumption, hence environmental impact, of transport.

Below a historical background to the present development of a three-dimensional velocimetry technique for turbulence measurements is given, which is followed by stating the aim and outlining the approach undertaken in this thesis.

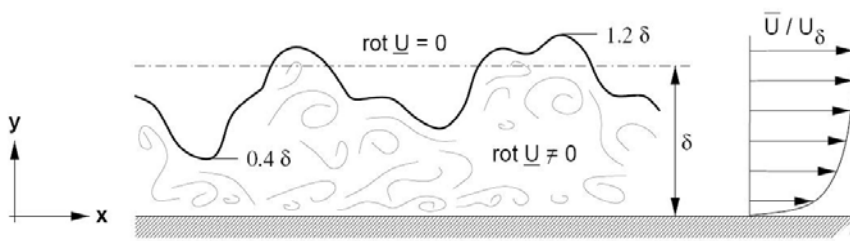


Figure 1.1. A schematic representation of the instantaneous fluid motions within a turbulent boundary layer and the mean velocity profile. (Jischa 1982, reproduced from Kähler 2004)

1.1

Views on turbulence in relation to experimental techniques

Historically, the perspective on the turbulence phenomenon has very much changed with the increase in experimental capabilities. In the early days (say 1920-1950, see Cantwell 1981, Robinson 1991 and references therein), a statistical description was generally adopted in which random (velocity) fluctuations were superimposed onto the mean flow. These fluctuations were characterized by statistical quantities such as standard deviations and correlation functions. This view on turbulence resulted mainly from the fact that (single) probe measurements (e.g. pressure probes, hot-wire and laser-Doppler anemometry) were available that provided only pointwise flow statistics. With the use of planar flow visualization (from say 1950s) and later in the 1980s quantitative planar velocity

measurements (in particular Particle Image Velocimetry, PIV, which will be discussed in more detail in chapter 2) the two-dimensional flow pattern and instantaneous planar velocity distribution became accessible, leading to the discovery of nonrandom, repeating, spatially coherent motions (or structures) within turbulent flow. It became apparent that these coherent structures were statistically relevant in the sense that they occurred frequently and were found to contribute significantly to the turbulence statistics as established previously by the probe measurements. Furthermore, they were believed to play an important role in the dynamics of turbulent flow, for example in the production of turbulent kinetic energy near the wall in boundary layers. However, with these planar techniques the structures were observed in two-dimensional space, whereas turbulence and its structure are essentially three-dimensional, leaving open questions regarding the full structure and dynamics.

Fully 3D quantitative turbulence information first became available not from experiments but from Direct Numerical Simulations (DNS, starting around the 1980s) in which the flow governing equations are solved numerically without turbulence modeling, resolving the whole range of spatial and temporal scales in the flow on a fine computational mesh. DNS returned a very detailed picture of the coherent structures confirming some of the models inferred from the planar measurements. Moreover, it further clarified the spatial relationship between different types of structures. However, much computational effort is required to perform these simulations, which moreover increases strongly with the Reynolds number as the range of flow scales that need to be resolved increases. Therefore, DNS has restricted use (i.e. applicable to relatively low Reynolds number and simple geometrical configurations). Furthermore, the simulation generally requires some input from experimental observations, such as the computational domain size needed to capture the largest relevant flow scales.

Therefore, 3D experimental velocimetry techniques yielding the instantaneous velocity distribution in a volume remain relevant and interesting, especially for the case of high Reynolds number turbulent flows. Developments towards such experimental capability have emerged recently, leading to a number of different approaches based on PIV principles. However, the available techniques are not widely used, due to the various restrictions and complexities of each method (see chapter 2 for a more complete discussion). Therefore, this field of research is still very much active. As a general remark: it will be difficult, if not impossible, to obtain the spatial resolution and level of detail offered by DNS experimentally, but for a good representation of the flow it is not always necessary to resolve all scales. Notably, most of the turbulent kinetic energy is contained in the larger scales of motion. In contrast, spatial resolution in DNS simulations can be critical for correct modeling of the physics, even if only the larger scales are of interest.

Besides revealing the ‘complete’ flow topology, 3D velocity information has additional advantages, which include: access to the full velocity gradient tensor (appearing in the equations describing the fluid flow) and the vorticity vector.

1.2

Aim of the thesis

The primary goal of the present work is the development of a three-dimensional digital Particle Image Velocimetry technique suitable for application in a wide range of flow regimes: low speed, high speed and supersonic flow. Especially robustness, spatial resolution and accuracy are considered key properties for the new technique in order to be successful in achieving this objective and to be, finally, of practical interest to the fluid dynamics community. This combination of capabilities and properties is not found in current

3D approaches and is achieved here by the use of tomographic principles. Hence the new technique will be referred to as Tomographic Particle Image Velocimetry (Tomographic-PIV).

A second objective of the present thesis is to apply the developed technique in the investigation of the 3D coherent structures in turbulent boundary layers at low and high Reynolds number (in the incompressible and supersonic flow regime respectively). The novel aspect is that these structures can be obtained directly from quantitative measurements without going through the process of inferring the instantaneous 3D structure from their reduced dimensional signatures, as in planar and single point measurements. Hence the results are not affected by assumptions or prior knowledge usually needed to produce the signatures. In addition, instantaneous 3D velocity data in supersonic turbulence, with associated high Reynolds number, does not exist presently; not from direct numerical simulation nor from experiment.

1.3

Outline of the thesis

The thesis consists of two parts. The first part outlines the development of the experimental technique starting in chapter 2 with the introduction of the working principle of planar PIV and with an overview of the current approaches to three dimensional PIV measurements. In reaction to this, the development of 3D Tomographic-PIV is further motivated and its working principle is given in chapter 3. Chapter 4 presents the assessment of the new technique by means of simulated experiments. The results are used to describe how the measurement accuracy relates to the experimental setup. Then, the experimental assessment by actual measurements of a cylinder wake flow is shown in chapter 5 showing the achieved accuracy as a function of the most relevant experimental parameters as identified in chapter 4. Furthermore, the application of PIV to supersonic flows brings some specific challenges, which will be discussed in chapter 6.

The second part of the thesis presents the application of the new technique to investigate coherent flow structures in turbulent boundary layers. Chapter 7 introduces the concept of coherent structures and briefly reviews results from earlier studies. Then, the structures obtained by Tomographic-PIV in a low speed, low Reynolds number turbulent boundary layer are presented in chapter 8. This case is well documented allowing a comparison with literature to be made. Furthermore, a nearly time-resolved measurement of a low Reynolds number tripped boundary layer (chapter 9) reveals some of the dynamical aspects associated to the coherent structures. The last application presented in chapter 10 shows the structures in a supersonic high Reynolds number turbulent boundary layer.

Finally chapter 11 summarizes the main conclusions from the present study. Moreover, future developments related to the Tomographic-PIV technique and its application to wall bounded turbulence are anticipated.

Part I
Development of the experimental technique

Chapter 2

Particle image velocimetry

The present chapter presents the basic working principle of planar Particle Image Velocimetry (PIV) together with an overview of existing three-dimensional PIV techniques to provide a perspective to the technique developments outlined in subsequent chapters. The 3D methods considered are holographic PIV, scanning PIV and 3D Particle Tracking Velocimetry, which will be discussed with applications and references to literature for further detailed reading.

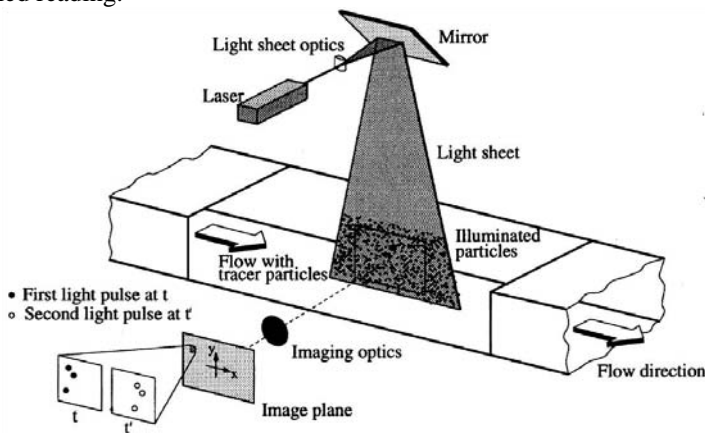


Figure 2.1: Principle of Particle Image Velocimetry. (Raffel et al. 1998)

2.1 Planar PIV

2.1.1 Working principle of PIV

Particle Image Velocimetry (PIV) techniques measure the instantaneous flow velocity distribution by evaluation of the motion of tracer particles suspended in the flow (see for example Adrian 1991, Westerweel 1993, Raffel et al. 1998). A typical PIV experimental arrangement is presented in figure 2.1, where tracer particles are added to the flow in a wind tunnel. These particles must be small enough, so it can be assumed that they move with the local flow velocity (see section 6.1 for more detail), and at the same time must be large enough to be visible when illuminated. In planar (2C) PIV the particles are illuminated twice by a (laser) light sheet, with the time delay Δt between the light pulses depending on the flow velocity and the magnification at imaging. Their images are recorded by a CCD camera onto two frames each corresponding to an illumination pulse. Between frames the tracer particles have moved in the illuminated plane by $\Delta \mathbf{x} = (\Delta x, \Delta y)$, which is measured by image

cross-correlation considering the ensemble of particles in sub-domains of the recordings (known as interrogation windows, section 2.1.2). As an example, figure 2.1 shows three particle images shifting to the right between time t and $t' = t + \Delta t$ within such a small part of the total recorded image. Then the measured local in-plane velocity V is obtained from the particle displacement Δx using:

$$V = \frac{\Delta x}{\Delta t} = \frac{1}{\Delta t} \int_{\Delta t} V(t) dt \quad (2.1)$$

where $V(t)$ is the particle ensemble velocity in time. It can be seen from the above that the measured velocity represents a temporal averaging over the pulse separation Δt as well as a spatial averaging over the particle ensemble within the recording sub-domain. Finally combining the information from all sub-domains returns the velocity vector distribution in the measurement plane.

2.1.2

Particle imaging

One important aspect in PIV is the imaging of the micrometer sized tracer particles. The particle image is determined by its geometric image and the point response function of the lens. Commonly the lens is diffraction limited, hence the response function is the Airy disk (Hecht 1998) of diameter d_{diff} , which is given by (Raffel et al. 1998):

$$d_{diff} = 2.44 f_{\#} (M + 1) \lambda \quad (2.2)$$

where $f_{\#}$ is the f-number defined as the focal length of the lens f divided by the aperture diameter, M is the magnification factor and λ is the wavelength of the scattered light. Alternatively, the geometric image diameter d_g is constructed from geometrical optics, which for a particle in the plane of focus returns $d_g = M \cdot d_p$, where d_p is the diameter of the particle. The final particle image diameter d_{pi} results from a convolution of the geometric image with the Airy disk, which can be approximated by (Adrian and Yao 1985):

$$d_{pi} = \sqrt{d_g^2 + d_{diff}^2} \quad (2.3)$$

In thin light sheets the geometric image diameter d_g is usually much smaller than d_{diff} allowing a simplification to: $d_{pi} = d_{diff}$. Hence the particle image diameter can be adjusted by changing the lens $f_{\#}$. Raffel et al. (1998) show an optimum 2 pixels diameters for lowest velocity measurement uncertainty. However, $f_{\#}$ cannot be chosen freely, as the lens aperture and consequently the amount of light collected by the imaging system reduces with increasing $f_{\#}$, which may cause the particles to become undetectable.

The particle images can be considered sharp when the geometrical particle image diameter due to blur is equal to the diffraction diameter d_{diff} . The distance in viewing direction over which this holds is known as the depth of focus or depth of field δz and is given by (Raffel et al. 1998):

$$\delta z = 4.88 f_{\#}^2 \left(\frac{M + 1}{M} \right)^2 \lambda \quad (2.4)$$

In practice the magnification factor M and the light wavelength λ are determined by the required field of view and the illumination source. Therefore, the depth of focus is primarily set through the $f_{\#}$. Consequently expanding the thin light sheet for planar PIV to thicker illumination volumes for 3D-PIV requires increasing $f_{\#}$ in order to have well focused particle images. Unfortunately, this also reduces the particle image intensity in the recordings.

2.1.3

Evaluation of particle image displacement

From the recordings, the particle image displacement is obtained on a statistical bases using cross-correlation. The displacement in the recordings is equivalent to the physical particle displacement in the measurement plane apart from a scaling factor (i.e. magnification factor), which is determined in a calibration.

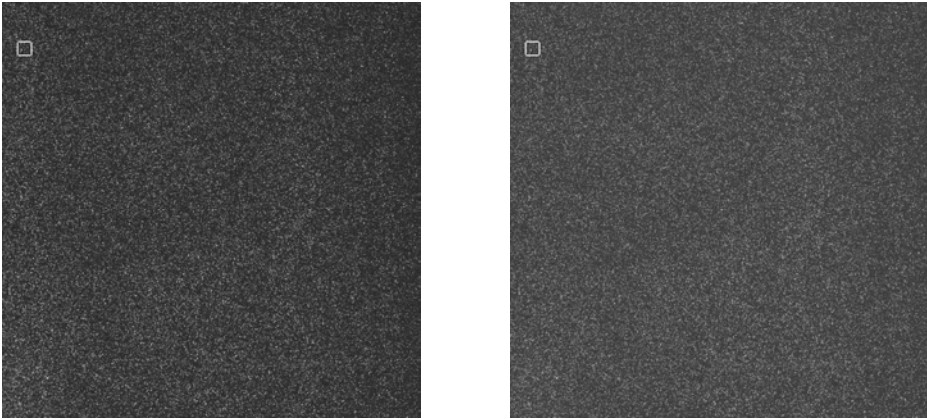


Figure 2.2: Double frame particle image recording. The first frame (artificially colored red, left) and second frame (artificially colored blue, right) represents the particle distribution at time t and $t+\Delta t$ respectively. The white square in the upper left corner indicates an interrogation window.

In the analysis, the complete recording (figure 2.2) is first divided into small sub-domains of $I \times J$ pixels size known as interrogation windows. Figure 2.3-left presents the image intensity distribution in the interrogation window indicated by the white square in figure 2.2, where the intensity distribution in the first frame I_a (in red) and second frame I_b (in blue) are shown overlaid. By eye a shift of the particle images, representing the flow velocity, can be noticed. The cross-correlation coefficient map R corresponding to these intensity distributions I_a and I_b is given by:

$$R_{I_a, I_b}(\Delta x, \Delta y) = \frac{\sum_{i=1}^I \sum_{j=1}^J I_a(i, j) I_b(i - \Delta x, j - \Delta y)}{\sigma_{I_a} \sigma_{I_b}} \quad (2.5)$$

where σ is the standard deviation of the intensity distribution and Δx and Δy are discrete pixel shifts in horizontal and vertical direction. The correlation map for the present example is presented in figure 2.3-right showing a maximum near $\Delta x = 4$ pixels. The peak location in the cross-correlation map can be determined with sub-pixel accuracy by a Gaussian peak fit around the maximum (Raffel et al. 1998) yielding the measured particle displacement between frames, hence velocity, within the interrogation window. Finally, by combining the results from all interrogation windows, the complete in-plane velocity distribution is obtained. Figure 2.4 shows the velocity distribution corresponding to the recordings in figure 2.2.

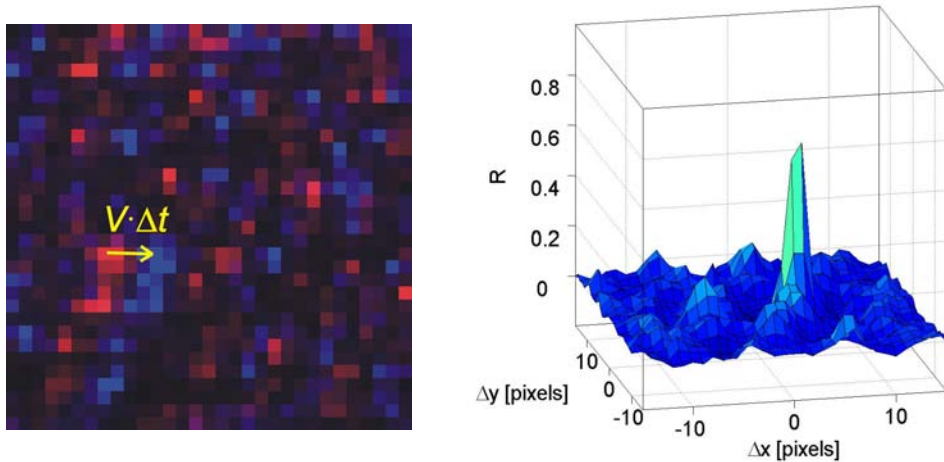


Figure 2.3: Overlay of the two image intensities in a 31×31 pixel interrogation window (first frame red, second frame blue) (left) and corresponding cross-correlation map (right).

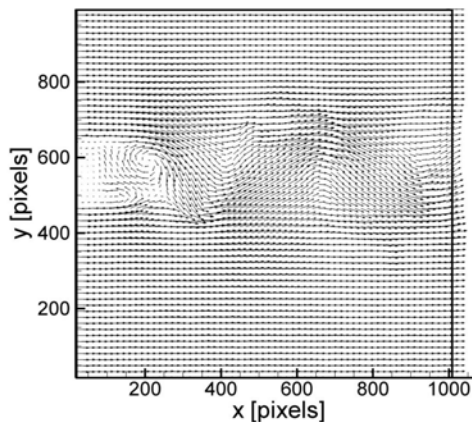


Figure 2.4: Vector field measured from the recording shown in figure 2.2.

The procedure outlined above represents a very basic cross-correlation algorithm. The PIV recordings in the present study have been analyzed using a more advanced iterative

multigrid window deformation technique (*WIDIM*, Scarano and Riethmuller 2000), which offers a higher dynamic range largely independent of spatial resolution due to progressively decreasing the interrogation window size in the first iterations. Furthermore, the measurement accuracy and spatial resolution are increased by deforming the windows according to the velocity gradient as predicted from the results of the previous iteration. For a complete discussion of iterative deformation methods is referred to Scarano (2002).

2.1.4

Stereoscopic PIV

The capabilities of PIV can be extended to yield all three components of velocity in the plane of the light sheet by applying two cameras that observe the tracer particle motion from different viewing directions (figure 2.5). This technique is referred to as stereoscopic-PIV (Arroyo and Greated 1991, Willert 1997, Prasad 2000).

Each camera observes a different projection of the local velocity vector in an interrogation window, which is perpendicular to its viewing direction (inset figure 2.5). Knowing the local viewing direction from a calibration for each camera (see section 3.4), the three components of the velocity vector can be constructed from its two projections using geometric relations, which can be found in Willert (1997) and Raffel et al. (1998).

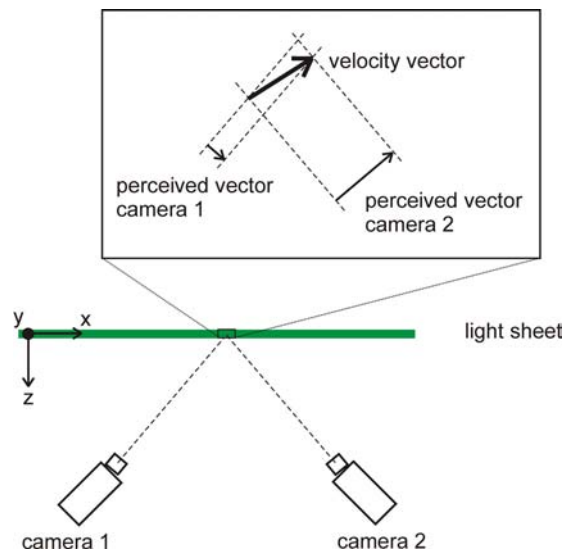


Figure 2.5: Principle of stereoscopic-PIV showing a top view of the experimental arrangement and the different projections of the particle velocity vector as perceived by the cameras (inset).

2.2 Overview of existing 3D PIV techniques

2.2.1 Holographic PIV

Among the different 3D velocimetry techniques presently available Holographic-PIV has received most attention (Hinsch 2002, Chan et al 2004, Arroyo and Hinsch 2007). It uses the interference pattern of a reference light beam with light scattered by a particle, which is recorded on a hologram, to determine the particle location in depth. The in-plane position in principle is given by the position of the diffraction pattern in the image. Illumination of the hologram with the reference light beam reproduces the original light intensity field in the measurement volume at the time of recording, the intensity being highest at the original particle location. The reconstructed intensity field is scanned by a sensor, e.g. a CCD, to obtain a digital intensity map, which can be used for cross-correlation yielding the velocity field. So far Holographic-PIV has shown a great potential in terms of a high data yield. However its drawbacks are that the recording medium is a holographic film requiring wet processing, which makes the process time consuming and somehow inaccurate due to misalignment and distortion when re-positioning the hologram for the object reconstruction. Moreover, the recoding of time-series on film for the study of dynamic flow phenomena is a technical challenge. Therefore, holographic-PIV studies generally use only a few recordings and do not present velocity statistics.

The holographic technique was successfully applied to measure for instance a vortex ring in air (Pu and Meng 2000), an artificially generated hairpin in an air channel flow (Svizher and Cohen 2006), a cylinder wake flow in air and a free air nozzle flow (Herrmann et al. 2000) returning large numbers of vectors (around 100,000 using individual particle pairing) at a single time instant. Figure 2.6 presents the instantaneous velocity field in the wake of a mixing tab in water obtained by Pu and Meng (2000). The volume is $44 \times 56 \times 32 \text{ mm}^3$ in size and contains 400,000 vectors, which have been interpolated from the 80,000 vectors originally measured by particle pairing. Part of the vector volume has been cut to reveal the flow structures inside the volume. The results demonstrate the capability of measuring the velocity in nearly cubic volumes at a good spatial resolution.

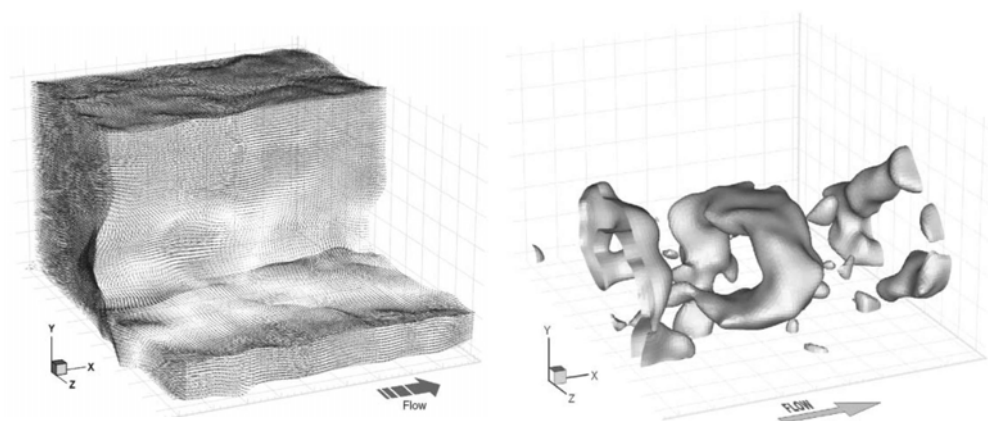


Figure 2.6: Holographic-PIV result showing the 3D velocity field behind a mixing tab (left) and the corresponding vorticity iso-surface (right). (Pu and Meng 2000)

Instead of recording on a photographic plate, the hologram can also be captured directly by a CCD sensor (Digital-Holographic-PIV, Coëtmelec et al 2001). In that case the light intensity distribution in the measurement volume is evaluated numerically, usually by solving the Fresnel diffraction formula on the hologram (near-field diffraction, Pan and Meng 2002). CCD sensors, however, have a very limited spatial resolution compared to the photographic plate returning about 2 to 3 orders less particle images and velocity vectors. Moreover the large pixel pitch requires that the recording is obtained at a relatively small angle (a few degrees between reference beam and scattered light) in order to resolve the interference pattern, hence strongly limiting the numerical aperture and depth resolution (Hinsch 2002).

2.2.2

Scanning PIV

The scanning-PIV technique is directly derived from standard 2C or stereo PIV with the light sheet scanning through the measurement volume (Brücker 1995). The volume is sliced by the laser sheet at sequential depth positions where the particle image pattern is recorded. The second recording at that depth position can be taken either directly after the first or after the complete scan of the volume. The procedure returns planar velocity fields obtained slightly shifted in space and time, which can be combined to return a 3D velocity field. The strong points of this technique are that it maintains the high spatial resolution of planar PIV and that the analysis of the recordings is straightforward. However, for any practical application scanning-PIV requires high-repetition systems (kHz) to ensure that the complete volume recording is almost simultaneous. The underlying hypothesis of scanning-PIV is that the volume scanning time needs to be small if compared with the characteristic time scale of the investigated flow structure. Cameras with a high recording rate are thus required, which is not a problem in low speed flow as, for example, shown by Hori and Sakakibara (2004) and Burgmann et al. (2006) measuring a turbulent jet and a laminar separation bubble both in water. However the technique is unsuited for air flows and in particular in high speed flows. Moreover high repetition rate lasers are expensive and provide relatively low pulse energy. It should also be remarked that the experimental setup is significantly more complicated by the addition of a scanning mechanism.

Figure 2.7 presents an example of scanning PIV results showing the velocity field and vorticity structure in a turbulent jet in water (Hori and Sakakibara 2004). The setup consisted of two CMOS cameras in stereoscopic-PIV configuration, which recorded images at 500 Hz resulting in a scanning time of 0.22 s for the complete $100 \times 100 \times 100 \text{ mm}^3$ volume. In this volume located 45 jet diameters downstream of the exit, approximately 40^3 velocity vectors are returned, where the maximum measured velocity is rather low at 24 mm/s. At this velocity, the flow structures convect by 5.3 mm during the volume scan. For a similar measurement in air at 5 m/s allowing the same shift of the flow structures during the scan, a recording rate of 100 kHz is required, which is clearly beyond the reach of current hardware. This illustrates that the scanning PIV technique is not suitable for the instantaneous 3D characterization of air flows.

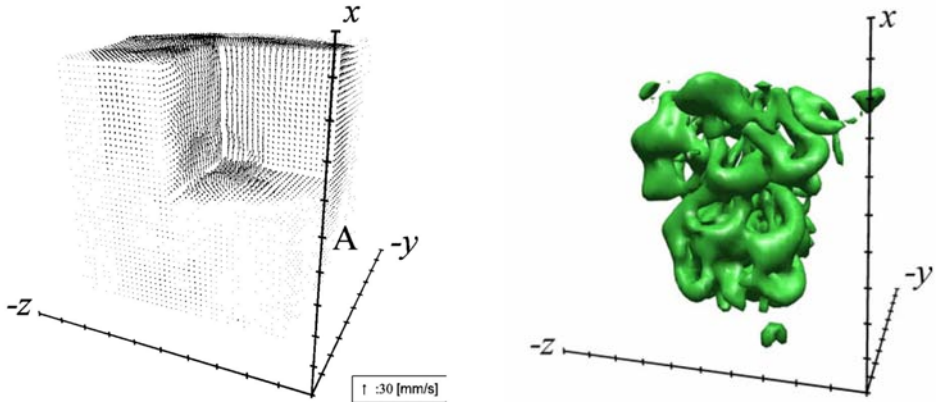


Figure 2.7: Scanning-PIV result showing the 3D velocity field (left) and vorticity iso-surface (right) in a water jet. (Hori and Sakakibara 2000)

As an alternative to scanning, dual plane stereo PIV (Kähler and Kompenhans 2000) records the particle images in different planes simultaneously using light polarization or different colors to distinguish the scattered light from the two planes (Mullin and Dahm 2006). In principle, measurements can be performed over more than two planes with each plane requiring a double-pulse laser, however separation by polarization is the most commonly adopted solution and is possible only over two planes. Furthermore using different colors complicates the optical arrangement.

2.2.3

3D Particle tracking velocimetry

Three-dimensional Particle Tracking Velocimetry (3D-PTV, Maas et al 1993) and defocusing PIV (Pereira et al 2000) rely on the identification of individual particles in the PIV recordings. The exact position of the particle within the volume is given by the intersection of the lines of sight corresponding to a particle image in the recordings from several viewing directions (typically three or four). The implementation of the particle detection and location varies with the methods. In comparison with the previous two methods, the 3D-PTV approach offers the advantage of being fully digital and fully three-dimensional without the requirement for moving parts. The velocity distribution in the volume is obtained from either particle tracking or by 3D-cross-correlation of the particles pattern (Schimpf et al 2003). Combining the particle tracking approach with time-resolved particle image recoding makes the technique successful in obtaining Lagrangian motion and determining Kolmogorov length and time scales in turbulent flows (Virant and Dracos 1997). However the procedure for individual particle identification and pairing can be complex and as it is common for planar PTV several algorithms have been proposed, which significantly differ due to the problem-dependent implementation. The main limitation reported in literature is the relatively low seeding density to which these techniques apply in order to keep a low probability of false particle detection and of overlapping particle images. Moreover, the precision of the volume calibration or in the description of the imaging optics is finite. This means that the lines of sight for a particle almost never truly intersect and an intersection criterion is needed. Consequently the

maximum seeding density in 3D PTV is kept relatively low. Maas et al (1993) report a seeding density of typically 0.005 particles per pixel (ppp) for a 3 camera system (compare with 0.05 to 0.10 ppp typically used in planar PIV).

A typical 3D-PTV result is presented in figure 2.8 showing particle tracks in isotropic turbulence in water (Lüthi et al. 2005). In this experiment the measurement volume was $20 \times 20 \times 15 \text{ mm}^3$ and contained approximately 800 particles. The imaging system consisted of 4 cameras, which recorded 640×480 pixel images at 60 Hz resulting in an image seeding density of 0.003 ppp. The particles were tracked with an efficiency of 60%, meaning that around 470 particles could be followed long enough (over 20 time steps) to obtain trajectories with particle accelerations. These trajectories in figure 2.8 are returned only at the position of the detected particles resulting in an unstructured measurement grid as seen in the plot, which is characteristic for particle tracking.

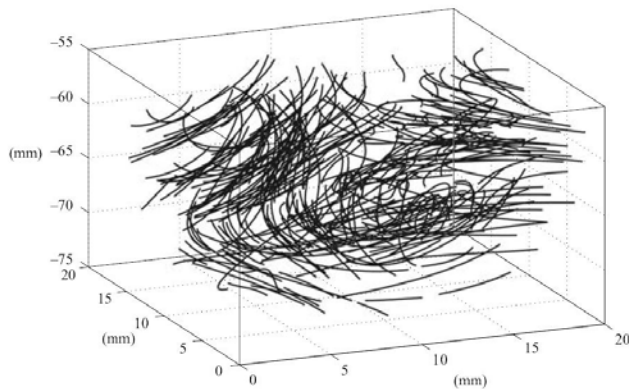


Figure 2.8: 3D-PTV result showing the particle tracks in isotropic turbulence in water. (Lüthi et al. 2005)

Chapter 3

Tomographic particle image velocimetry

3.1

Motivation for development

The development of the proposed Tomographic-PIV technique is motivated by the need to achieve a digital 3D measurement system that combines the simple optical arrangement of the photogrammetric approach with a robust particle volume reconstruction procedure, which does not rely on particle identification. As a consequence the seeding density can be increased, with respect to 3D PTV, to around 0.05 particles per pixel (as will be shown in chapters 4 and 5). The robustness of the velocimetry technique is further increased by applying particle pattern cross-correlation instead of individual particle tracking.

The particle image density used in Tomographic-PIV is similar to planar experiments and consequently the total number of velocity vectors in the 3D domain is comparable or slightly higher than obtained in planar PIV. Therefore scanning PIV is expected to remain the digital 3D PIV technique with the largest data yield in a single volume. However, as discussed in the previous chapter, scanning is limited to low speed flows and always requires high-repetition rate PIV hardware. In contrast photogrammetric techniques feature the instantaneous flow field measurement opening the possibility to perform 3D measurements in several conditions irrespective of the flow velocity magnitude using standard low-repetition rate hardware (see chapter 10 for a high speed application). High-repetition rate PIV hardware is not required, but can be used to further extend the measurement technique's capability to a three-dimensional time-resolved flow diagnostic tool, as has already been demonstrated in a recent study (see chapter 9 and Schröder et al 2006, 2008).

The application of digital imaging devices, e.g. CCD cameras, reduces the complexity of the experimental setup and allows to record time series as opposed to film-based holographic PIV. Digital holography is able to return time series, however the particle image density, hence vector yield, is relatively low as discussed in the previous chapter. The strength of the holographic PIV technique lies in the measurement of small volumes of the order of 1 cm^3 .

3.2

Principles of Tomographic-PIV

The working principle of Tomographic-PIV is schematically represented in figure 3.1. Tracer particles immersed in the flow are illuminated by a pulsed light source within a three-dimensional region of space. The scattered light pattern is recorded simultaneously from several viewing directions using CCD cameras at two subsequent times t and $t+\Delta t$. Similar to stereo-PIV, adapters are used to fulfill the Scheimpflug condition between the image plane, lens plane and the mid-object-plane. Moreover the particles within the entire volume need to be imaged in focus, which is obtained by setting a proper $f_{\#}$ (Eq. 2.4). After the

recording step the 3D particle distribution (the object) is reconstructed as a 3D light intensity distribution from its projections on the CCD arrays. The reconstruction is an inverse problem and its solution is not straightforward since it is in general underdetermined: a single set of projections can result from many different 3D objects. Determining the most likely 3D distribution is the topic of tomography (Herman and Lent 1976, Herman 1980, Timmerman 1997), which will be addressed in the following section. The particle displacement (hence velocity) within a chosen interrogation volume is then obtained by the 3D cross-correlation of the reconstructed particle distribution at the two exposures. The cross-correlation algorithm is based on the cross correlation analysis with the iterative multigrid window (volume) deformation technique (*WIDIM*, Scarano and Riethmuller, 2000) extended to three dimensions.

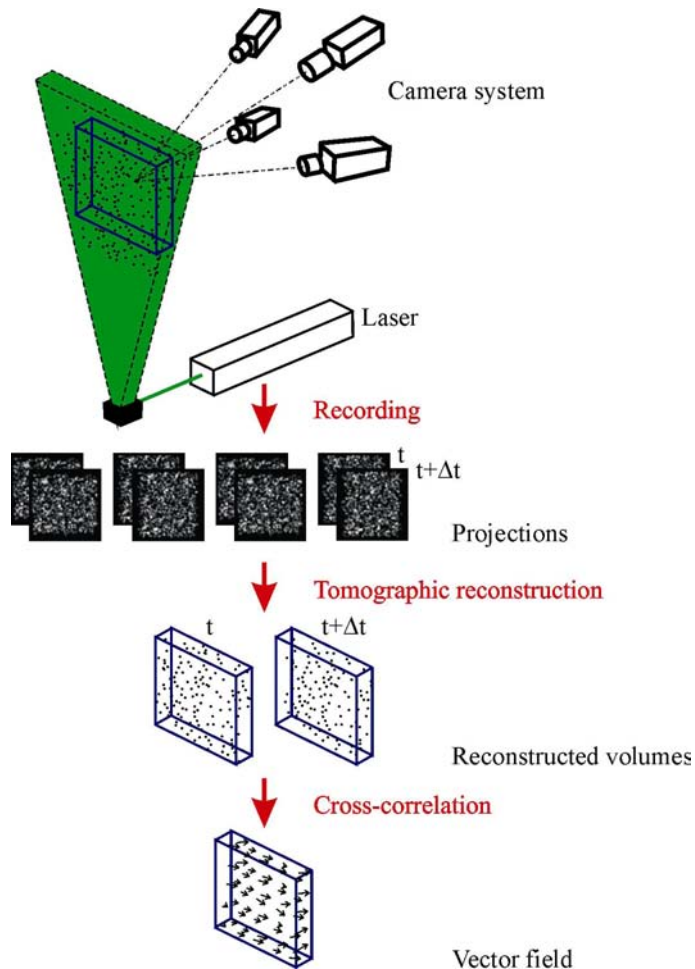


Figure 3.1: Principle of Tomographic-PIV

The relation between image (projection) coordinates and the physical space (the reconstruction volume) is established by a calibration procedure common to stereo PIV, which will be discussed briefly here and in more detail in section 3.4. The procedure starts by each camera recording images of a calibration target at several positions in depth throughout the volume. From these images the calibration procedure returns a mapping function, the viewing directions and the field of view. The mapping from physical space to the image coordinate system can be performed by means of either camera pinhole model (Tsai 1986) or by a third-order polynomial in x and y (Soloff et al 1997). As will be shown in the next chapter the correct tomographic reconstruction of a particle from its images relies on an accurate triangulation of the views from the different cameras, which translates into a required calibration accuracy of a fraction of the particle image size. Therefore a technique for the a-posteriori correction for minor calibration errors and system misalignment can significantly improve the accuracy of reconstruction (see section 3.4 and Wieneke 2007).

3.3 Tomographic reconstruction techniques

The novel aspect introduced with Tomographic-PIV is the reconstruction of the 3D particle distribution by tomography. Therefore a separate section is devoted to the tomographic reconstruction problem and algorithms for solving it.

By considering the properties of the measurement system, it is possible to select a-priori the reconstruction method expected to perform adequately for the given problem. First the particle distribution is discretely sampled on pixels from a small number of viewing directions (typically 3 to 6 CCD cameras) and secondly it involves high spatial frequencies. In these conditions algebraic reconstruction methods are more appropriate with respect to analytical reconstruction methods, such as Fourier and back-projection methods (Verhoeven 1993). For this reason, only the former class of methods is considered for further evaluation.

Algebraic methods (Herman and Lent 1976) iteratively solve a set of linear equations modeling the imaging system, or in general measurement system. In the present approach the measurement volume containing the particle distribution (the object) is discretized as a 3D array of cubic voxel elements in (X,Y,Z) (in tomography referred to as the basis functions) with intensity $E(X,Y,Z)$. A cubic voxel element has a uniform non-zero value inside and zero outside and its size is chosen comparable to that of a pixel, because particle images need to be properly discretized in the object as it is done in the images. Moreover the interrogation by cross-correlation can be easily extended from a pixel to a voxel based object. Then the projection of the light intensity distribution $E(X,Y,Z)$ onto an image pixel (x_i, y_i) returns the pixel intensity $I(x_i, y_i)$ known from the recorded images, which is written as a linear equation:

$$\sum_{j \in N_i} w_{i,j} E(X_j, Y_j, Z_j) = I(x_i, y_i) \quad (3.1)$$

where N_i indicates the voxels intercepted or in the neighborhood of the line of sight corresponding to the i^{th} pixel (x_i, y_i) (shaded voxels in figure 3.2). The weighting coefficient $w_{i,j}$ describes the contribution of the j^{th} voxel with intensity $E(X_j, Y_j, Z_j)$ to the pixel intensity $I(x_i, y_i)$ and is calculated as the intersecting volume between the voxel and the line of sight (having the cross sectional area of the pixel) normalized with the voxel volume. The coefficients depend on the relative size of a voxel to a pixel and the distance between the voxel center and the line of sight (distance d in figure 3.2). Note that $0 \leq w_{i,j} \leq 1$ for all

entries $w_{i,j}$ in the two-dimensional array W and that W is very sparse, since a line of sight intersects with only a small part of the total volume. In principle the weighting coefficients can also be used to account for different camera sensitivities, forward or backward scatter differences or other optical dissimilarities between the cameras. Alternatively the recorded images can be pre-process in an appropriate way to compensate for these effects.

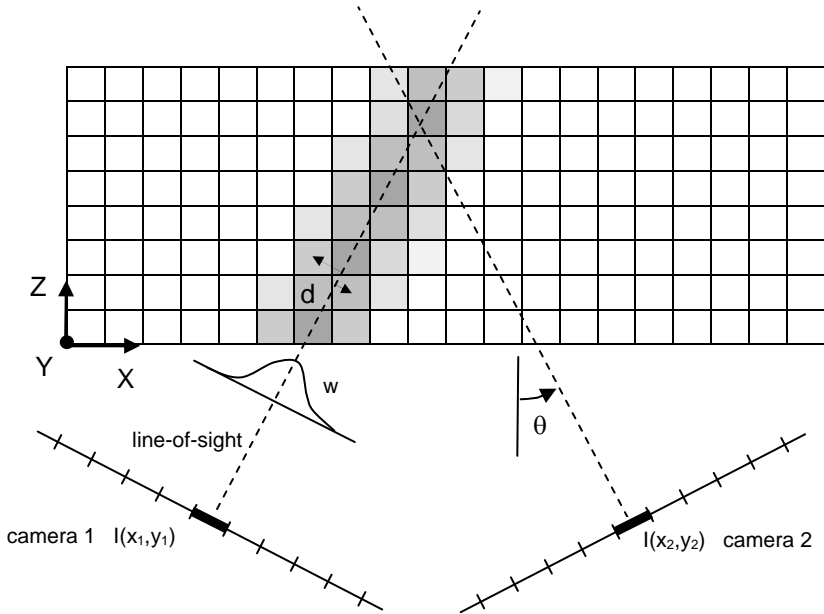


Figure 3.2: Representation of the imaging model used for tomographic reconstruction. In this *top-view* the image plane is shown as a line of pixel elements and the measurement volume is a 2D array of voxels. The gray level indicates the value of the weighting coefficient ($w_{i,j}$) in each of the voxels with respect to the pixel $I(x_1, y_1)$.

In the above model, applying geometrical optics, the recorded pixel intensity is the object intensity $E(X, Y, Z)$ integrated along the corresponding line of sight. In that case the reconstructed particle is represented by a 3D Gaussian-type blob, which projection in all directions is the diffraction spot. These reconstructed particle blobs are suitable for analysis with existing PIV cross-correlation algorithms providing sub-pixel accuracy.

A range of algebraic tomographic reconstruction algorithms is available to solve these equations (Eq. 3.1). However due to the nature of the system, the problem is underdetermined and the calculation may converge to different solutions, which implies that these algorithms solve the set of equations of Eq. 3.1 under different optimization criteria. A detailed discussion and analysis of these optimization criteria is beyond the scope of the present study and can be found in Herman and Lent (1976). Instead the performance of two different tomographic algorithms is evaluated in chapter 4 by numerical simulations of a Tomographic-PIV experiment focusing the evaluation upon the reconstruction accuracy and

convergence properties. The comparison is performed between the additive and multiplicative techniques referred to as ART (algebraic reconstruction technique) and MART (multiplicative algebraic reconstruction technique) respectively (Herman and Lent 1976). Starting from a suitable initial guess ($E(X,Y,Z)^0$ is uniform) the object $E(X,Y,Z)$ is updated in each full iteration as:

- 1) for each pixel in each camera i :
- 2) for each voxel j :

$$\text{ART: } E(X_j, Y_j, Z_j)^{k+1} = E(X_j, Y_j, Z_j)^k + \mu \frac{I(x_i, y_i) - \sum_{j \in N_i} w_{i,j} E(X_j, Y_j, Z_j)^k}{\sum_{j \in N_i} w_{i,j}^2} w_{i,j} \quad (3.2)$$

$$\text{MART: } E(X_j, Y_j, Z_j)^{k+1} = E(X_j, Y_j, Z_j)^k \left(\frac{I(x_i, y_i)}{\sum_{j \in N_i} w_{i,j} E(X_j, Y_j, Z_j)^k} \right)^{\mu w_{i,j}} \quad (3.3)$$

end loop 2
end loop 1

where μ is a scalar relaxation parameter, which for ART is between 0 and 2 and for MART must be ≤ 1 . In ART the magnitude of the correction depends on the residual $I(x_i, y_i) - \sum_{j \in N_i} w_{i,j} E(X_j, Y_j, Z_j)$ multiplied by a scaling factor and the weighting coefficient, so that only the elements in $E(X,Y,Z)$ affecting the i^{th} pixel are updated. Alternatively in MART the magnitude of the update is determined by the ratio of the measured pixel intensity I with the projection of the current object $\sum_{j \in N_i} w_{i,j} E(X_j, Y_j, Z_j)$. The exponent again ensures that only the elements in $E(X,Y,Z)$ affecting the i^{th} pixel are updated. Furthermore the multiplicative MART scheme requires that E and I are positive definite.

Besides the sequential update algorithms of Eqs. 3.2 and 3.3 schemes exist that update the reconstructed object simultaneously at every pixel using all equations in a single step. Examples of such simultaneous schemes are the conjugate gradient method (additive scheme) and several implementations of a simultaneous MART algorithm (Mishra et al 1999). Those methods return results similar to the sequential schemes and are potentially computationally more efficient. However the full investigation of those methods goes beyond the scope of the present study, but may be the subject of further investigations.

To illustrate some aspects of the tomographic reconstruction consider the basic 2 camera imaging system of figure 3.3. The X,Z slice of a volume contains a single particle, which is represented by a Gaussian intensity distribution referred to as the exact distribution $E_0(X,Z)$. The 2 camera image intensities I corresponding to this object are given by a summation of the intensity distribution $E_0(X,Z)$ in X -direction (camera 1) and in Z -direction (camera 2), which is written as:

$$\overline{\overline{W E_0}} = \overline{I} \quad (3.4)$$

following the notation of Eq. 3.1. The two-dimensional array W containing the weighting coefficients is shown in figure 3.4. As mentioned above W is sparse and for the present system it contains 200 non-zero elements out of a total of 2000 elements.

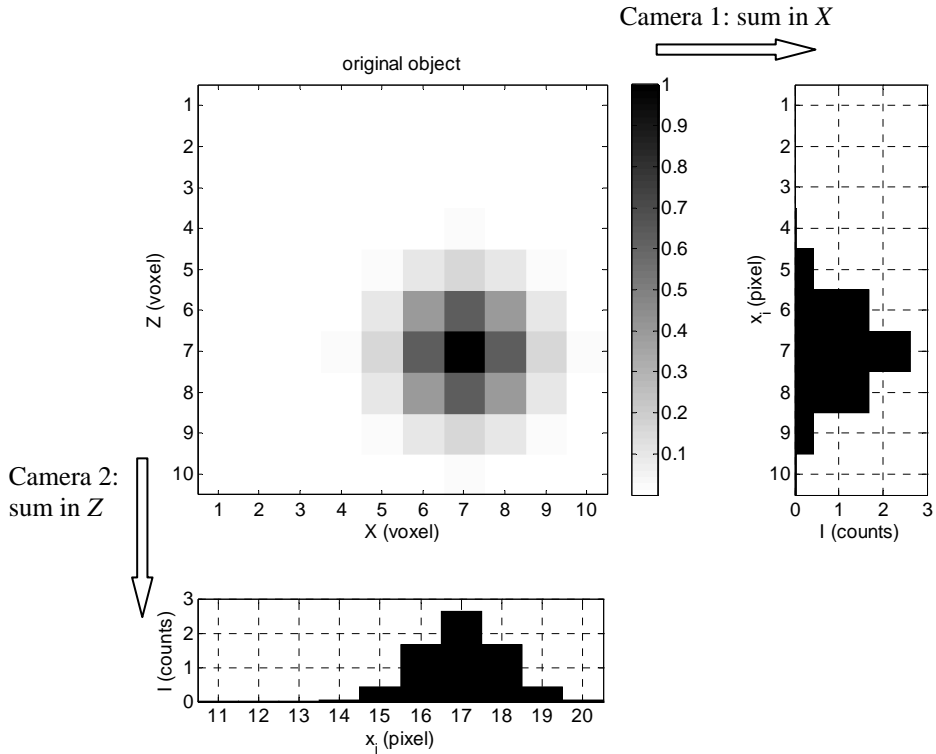


Figure 3.3: A single particle in a X,Z slice of a volume imaged by 2 cameras.

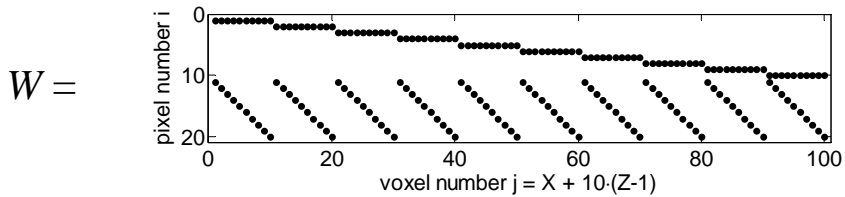


Figure 3.4: Non-zero weighting coefficients (dots). Rows 1 to 10 correspond to camera 1 (summation in X -direction in fig. 3.3) and rows 11 to 20 correspond to camera 2 (summation in Z -direction).

Of course in real experiments only the image intensities I and weighting coefficients W will be known, so the aim is to reconstruct the intensity distribution $E(X,Z)$ using:

$$\overline{\overline{W E}} = \overline{I} \quad (3.5)$$

From linear algebra it is known that the general solution to this problem is given by:

$$\overline{E} = \overline{E_0} + a_1 \overline{N_1} + a_2 \overline{N_2} + a_3 \overline{N_3} + \dots \quad (3.6)$$

where a_i are scalar variables and the arrays N_i are solutions of the set of homogeneous equations:

$$\overline{\overline{W N_i}} = 0 \quad (3.7)$$

The set of solutions to Eq. 3.7 is called the null space of W , which for the present system consists of 81 independent arrays N_i . The general solution (Eq. 3.6) contains as many degrees of freedom through the variables a_i . This clearly shows that the reconstruction problem is not trivial and that many solutions exist due the fact that the problem is underdetermined. An example of a solution alternative to the exact distribution $E_0(X,Z)$ is presented in figure 3.5. It has been obtained by combining the exact distribution $E_0(X,Z)$ with the homogeneous solution shown in figure 3.5-right.

Next the reconstruction problem of Eq. 3.5 is solved using tomography to compare with $E_0(X,Z)$. Here only the MART algorithm will be considered leaving the comparison of ART and MART for later discussion in section 4.2. Starting from a uniform intensity distribution (initial guess $E^0 = 1$), the intensity distributions at different stages of the reconstruction process are presented in figure 3.6. After 1/2 iteration (update using only the first half of all the pixels, which correspond to camera 1) the intensity distribution from the image of camera 1 is back-projected into the volume. Then completing the first iteration by using the information contained in the second image (camera 2) returns a distinct particle. At this point the reconstruction resembles a multiplication of the back-projected images from both cameras, which in a way ensures smoothness of reconstructed particle similar to particle image and explains why the solution does not converge to the irregular alternative solution of figure 3.5. The end result after 5 iterations shows a nearly perfect agreement with the exact distribution $E_0(X,Z)$ (figure 3.3). Although the present reconstructions after 1 and 5 iterations are nearly identical, it must be stressed that this is not generally the case. When the volume contains more particles, an improvement of the reconstruction with addition iterations can be noticed, as will be shown in the following chapter.

The above result demonstrates that a single particle can be reconstructed accurately by the MART algorithm. However adding a particle to the present exact intensity distribution $E_0(X,Z)$ and two corresponding camera images results in the tomographic reconstruction returning four distinct particles of equal intensity (see section 4.1), which indicates a significant contribution from the homogeneous solutions. Again this proves that the tomographic reconstruction is not straightforward. When the number of particles, the number of cameras and the size of the measurement volume are increased further, the reconstruction process becomes very complex and the result cannot be easily predicted. Therefore extensive numerical simulations need to be carried out to assess the performance

of the reconstruction algorithm for a range of different experimental configurations as to establish for which conditions the method can be applied successfully (chapter 4). Furthermore it is desirable to have a procedure to evaluate the reconstruction accuracy in case of an actual experiment where the exact intensity distribution is not known. Such a procedure will be discussed in chapter 5.

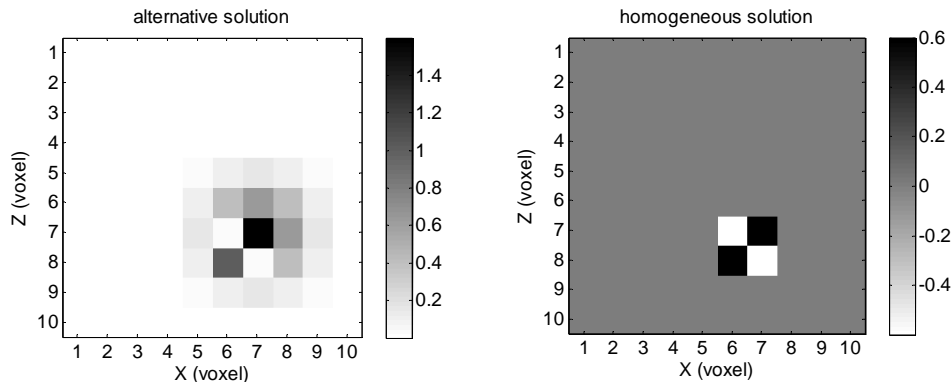


Figure 3.5: An alternative solution (left) obtained by combining the exact distribution $E_0(X,Z)$ with a homogeneous solution (right).

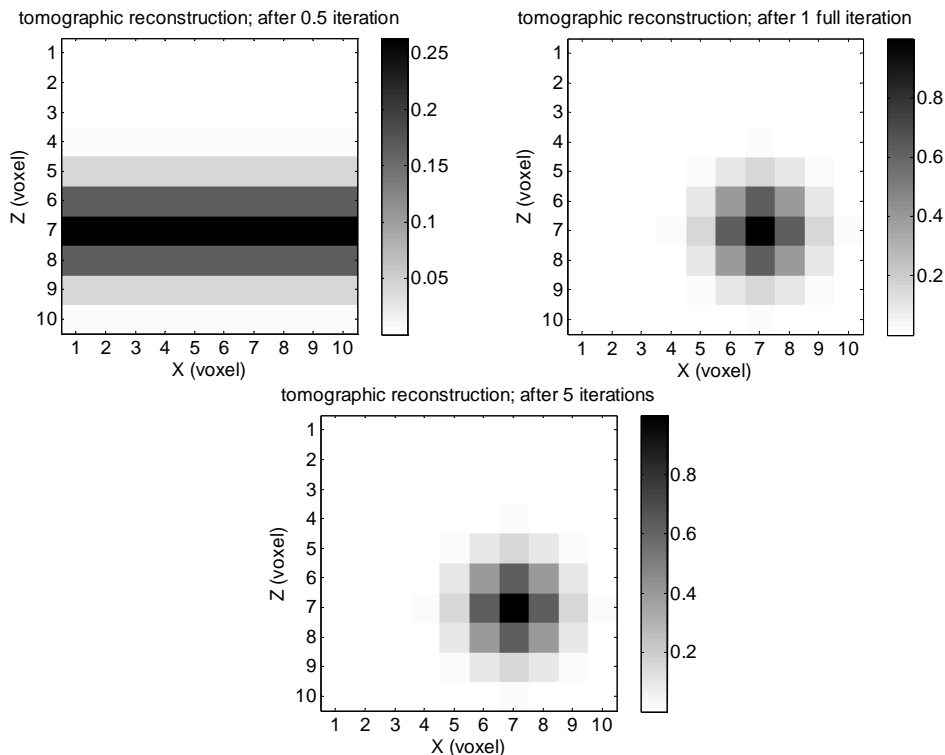


Figure 3.6: Tomographic reconstruction from the 2 camera images of figure 3.3. Top-left: reconstruction using only camera 1. Top-right: reconstruction after 1 full iteration using both cameras. Bottom: result after 5 iterations.

3.4

3D calibration and calibration correction

The relation between the physical coordinate system (X,Y,Z) and the image coordinates (x,y) needed to compute the weighting coefficients is established by a volume calibration, which for the present experiments is performed in the commercial software package Davis (LaVision 2006). The first step in the calibration procedure is to record an image of a calibration target with each camera. The calibration target contains a number of marks (either dots or crosses, figure 3.7) with known X,Y coordinates in a plane of constant Z . The position of these marks in each camera image is determined by cross-correlation with a template of the mark. Then a third-order polynomial in X and Y (Soloff et al 1997) is fit to the physical and image coordinates of all marks to obtain the mapping function, which is written as:

$$\begin{aligned} x &= a_0 + a_1X + a_2X^2 + a_3X^3 + a_4Y + a_5Y^2 + a_6Y^3 + a_7XY + a_8X^2Y + a_9XY^2 \\ y &= b_0 + b_1X + b_2X^2 + b_3X^3 + b_4Y + b_5Y^2 + b_6Y^3 + b_7XY + b_8X^2Y + b_9XY^2 \end{aligned} \quad (3.8)$$

where the calibration coefficients a_i and b_i depend on the depth position Z . By repeating this procedure at several (typically 3) positions in depth throughout the volume, mapping functions are returned at each discrete Z position. To obtain the X,Y position of a line of sight, i.e. constant image coordinates (x,y) , at intermediate Z positions linear interpolation or extrapolation is used. Thereby it is assumed that light propagates along straight lines in the medium (air or water), which is physically correct for incompressible flows.

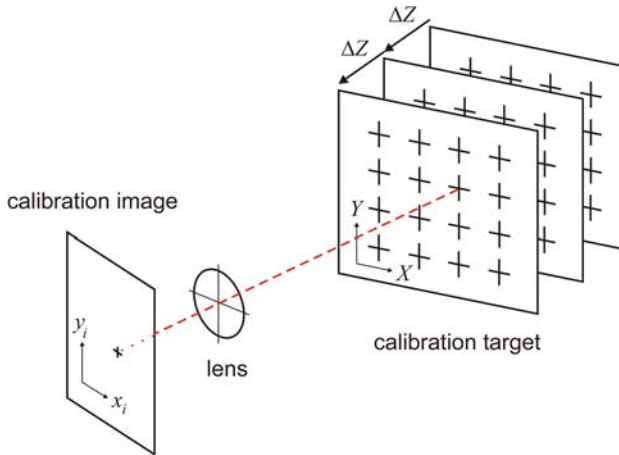


Figure 3.7: Calibration image recording.

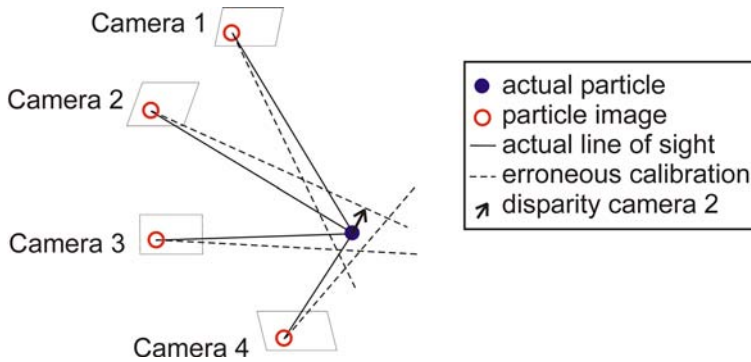


Figure 3.8: Residual triangulation disparity due to calibration errors. Lenses are omitted for simplicity.

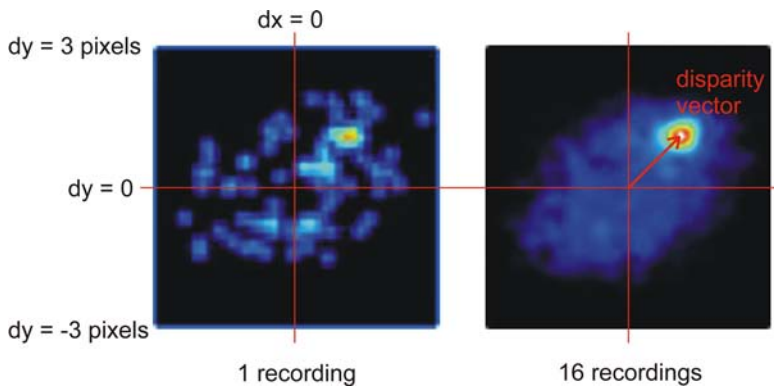


Figure 3.9: Disparity map for a single sub-volume (left) and the same map averaged over 16 recordings (right). (modified from Wieneke 2007)

As will be demonstrated in the following chapter, the tomographic reconstruction is sensitive to calibration errors, which may result from inaccuracies in the detection of the markers in the calibration images or inaccurate calibration plates. The effect of these errors can be seen from figure 3.8 as a disparity between the actual line of sight (solid lines) and the corresponding calibration mapping (dashed lines). Consequently the latter no longer intersect at the correct position in the measurement volume, hence particles cannot be triangulated perfectly.

In order to reduce these remaining errors in the mapping function, Wieneke (2007) has proposed a volume self-calibration procedure based on the recorded particle images. In the first step the 1000 to 5000 brightest particles in the recording from each camera are detected and triangulated in the measurement volume within a specified uncertainty. This part is identical to 3D particle tracking (Maas et al. 1993) and uses the original calibration. The actual particle position is then estimated within the triangulation region by a best fit. In the second step, the complete measurement volume is divided into sub-volumes (typically $5 \times 5 \times 5$). Using the original calibration, each estimated particle position is back-projected onto the camera recordings, which compared to the detected position in the recordings

returns a disparity error for each particle. Binning the disparity error, smoothing the contribution of each particle and summing over all particles in the sub-volume returns a disparity map (figure 3.9-left), which, after averaging over several recordings, shows a distinct peak (figure 3.9-right) corresponding to the final disparity vector for that sub-volume. In the last step a 3D disparity vector field is constructed from the contributions of the sub-volumes, which is used to update the calibration mapping function.

The self-calibration procedure has been shown to correct calibration errors up to a maximum of 7 pixels and reduce them to below 0.1 to 0.2 pixels (Wieneke 2007). Moreover this procedure allows quantifying the calibration accuracy in experiments.

Chapter 4

Theoretical and numerical assessment

As previously discussed the tomographic reconstruction is not trivial and may return incorrect 3D particle distributions in some cases. Therefore the present chapter aims to quantify the reconstruction accuracy using a theoretical and numerical approach. First an analytical expression is derived for the expected number of false particles in a reconstructed volume (i.e. ghosts) as to identify the most relevant experimental parameters. Then the results from a computer simulated Tomographic-PIV experiment show the accuracy of the reconstruction technique as functions of these experimental parameters. Also the performance of the two algebraic tomographic algorithms ART and MART is compared based on a numerical simulation. Finally a full scale simulation will demonstrate the capability and potential of the Tomographic-PIV method in terms of vector yield and velocity accuracy.

4.1

Estimate for the number of ghost particles

The most important source of reconstruction error in photogrammetric 3D-PIV techniques is the formation of false or ghost particles, which is illustrated in figure 4.1 for a 2-camera system. In this example the measurement volume contains two particles, which are seen by camera 1 along the lines-of-sight LOS_1 and LOS_2 and by camera 2 along the lines LOS_3 and LOS_4 . In the reconstruction process these recorded particle images and corresponding LOS 1 to 4 are used to determine the particle distribution in the measurement volume. Particles are formed where the lines-of-sight corresponding to a particle image in each camera intersect. For the present case these lines triangulate in four points resulting in three possible solutions for the particle reconstruction (figure 4.2). It can be shown in a simulation similar to what has been presented in section 3.3 that the present tomographic reconstruction algorithm converges to the 4-particle solution shown in figure 4.2-C, where the particles have equal intensity. Two of the reconstructed particles correspond to actual tracer particle and two are ghost particles or noise peaks in the reconstruction (figure 4.1). As shown below and stated by Maas et al. (1993) the number of ghost particles is determined mainly by three experimental parameters: the number of cameras, the tracer particle density and the light sheet or volume thickness.

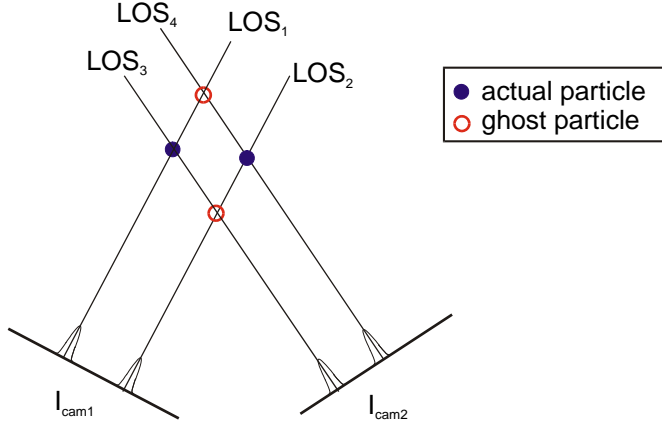


Figure 4.1: Formation of ghost particles in a 2 camera setup.

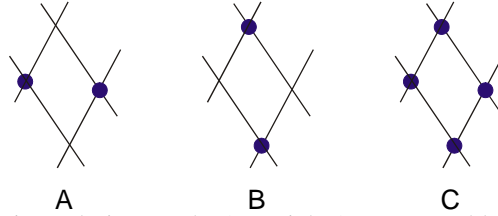


Figure 4.2: Reconstruction solutions to the 2-particle-2camera problem of figure 4.1.

In the general case of an N -camera system, a particle (either ghost or actual particle) is reconstructed in a point in a three-dimensional volume, when each of the N lines-of-sight going through that point corresponds to a particle image in the respective N recordings. Assuming ghost particle formation is a random process, the probability that a given point in the volume corresponds to a particle image in each recordings is $(ppp \cdot A_p)^N$, where ppp (particles per pixel) is the particle density in the recordings and A_p is the effective particle image area in pixel units, which is not necessarily equal to the area of the airy disk (Eq. 2.2). Then the total number of ghost particles N_g in the measurement volume is given by:

$$N_g = (ppp \cdot A_p)^N \cdot l_x \cdot l_y \cdot l_z \quad (4.1)$$

where $l_x \cdot l_y \cdot l_z$ are the dimensions of the reconstruction volume in x , y and z direction in voxel units (width, height and thickness). The number of actual tracer particles in the volume N_p is estimated by:

$$N_p = ppp \cdot l_x \cdot l_y \quad (4.2)$$

which is the total number of particles in the recordings. It is assumed that the pixels and voxels have equal dimensions and that the entire volume can be imaged onto $l_x \cdot l_y$ pixels.

Furthermore the thickness l_z of the volume usually is much smaller than its height and width. Then the signal-to-noise ratio in the tomographic reconstruction is defined as the ratio of actual tracer particle over ghost particles N_p/N_g :

$$\frac{N_p}{N_g} = \frac{1}{ppp^{N-1} \cdot A_p^N \cdot l_z} \quad (4.3)$$

From this equation it is seen that the signal-to-noise ratio in the reconstruction strongly depends on the particle image density expressed in ppp . With decreasing ppp the chance of random intersections of lines-of-sight corresponding to particle images rapidly decreases, hence the number of ghost particles drops. Note that because $ppp < 1$, the reconstruction signal-to-noise ratio increases with increasing number of cameras N . The ratio N_p/N_g furthermore depends on the depth of the reconstruction volume, which is proportional to the interception length of the line-of-sight with the volume. Finally the effective particle image area A_p is usually a constant in a given experimental setup, which depends mainly on the optical settings (i.e. $f_{\#}$).

4.2 Parametric study

The above assessment provides a first rough estimate of the reconstruction accuracy ignoring for instance the interactive updates. Therefore performance of the tomographic reconstruction is further evaluated based on numerical simulations, in which the order of the problem is reduced from a 3D volume with 2D images to a 2D slice with 1D images. This simplifies the computation and the interpretation of the results without losing generality on the results. In fact the 2D volume can be seen as a single slice selected from a 3D volume and similarly the 1D image as a single row of pixels taken from a 2D image.

Tracer particles are distributed in a 50×10 mm² slice, which is imaged along a line of 1000 pixels from different viewing directions θ (figure 3.2) by cameras placed at infinity, such that magnification and viewing direction are constant over the field of view and the magnification is identical for all views and close to 1. Furthermore the entire volume is assumed to be within the focal depth. Given the optical arrangement the particle location in the images is calculated and the application of diffraction (particle diameter is 3 pixels, which is justified by the large $f_{\#}$ required) results in the synthetic recordings. The particle image intensity is assumed uniform. The 2D particle field is reconstructed from these recordings at 1000×200 voxel resolution using the tomographic algorithms described in the previous chapter. Unless stated otherwise the following (baseline) experimental parameters are assumed: 3 cameras at $\theta = \{-20, 0, 20\}$ degrees, 50 particles (0.05 particles per pixel), 5 reconstruction iterations and no calibration errors or image noise.

First the reconstructions returned by the ART and MART algorithm (Eq. 3.2 and 3.3) are compared. For the ART reconstruction the relaxation parameter is set at 0.2 and the initial condition is a uniform zero intensity distribution, while for MART relaxation and initial condition are both 1. The resulting reconstructed particle fields after 20 iterations are shown in figure 4.3. The maximum intensity is 75 counts and values below 3 counts are blanked for readability. The ART algorithm leaves traces of the particles along the lines of sight, while the MART reconstruction shows more distinct particles. The additive ART scheme works similar to an OR-operator: in order to have a non-zero intensity in the object it is sufficient to have a particle at the corresponding location in one of the PIV recordings. It can be

compared with adding back-projections from the individual images, which gives a non-zero intensity when a particle is found in either the first *or* any other image or in all images. Still the intensity is highest at the actual particle locations. The multiplicative MART scheme behaves as AND-operator: similar to multiplying back-projections from the individual images leaving non-zero intensity only at locations where a particle appears in all recordings. The suitability of MART to reconstruct objects with sharp gradients or spikes has been confirmed by Verhoeven (1993). In conclusion, the artifacts in the ART reconstruction are undesirable, especially considering that the signal has to be cross-correlated for interrogation to provide the desired velocity (displacement) information. The result from the MART algorithm, therefore, better suits Tomographic-PIV. Moreover figure 4.4 shows that the individual particles reconstructed with MART are reconstructed at the correct position with an intensity distribution slightly elongated in depth ($dz \sim 1.5 dx$ for the present case). Therefore only the MART algorithm will be considered from here on.

The remainder of this section discusses the effect of the experimental and algorithm parameters on the MART reconstruction based on numerical simulations. Besides the number of cameras, the particle image density and measurement volume thickness, which have been identified in section 4.1 (Eq. 4.3) as critical to the reconstruction accuracy, also the number of iterations in the reconstruction, reconstruction resolution, camera viewing directions, calibration accuracy and image noise are considered.

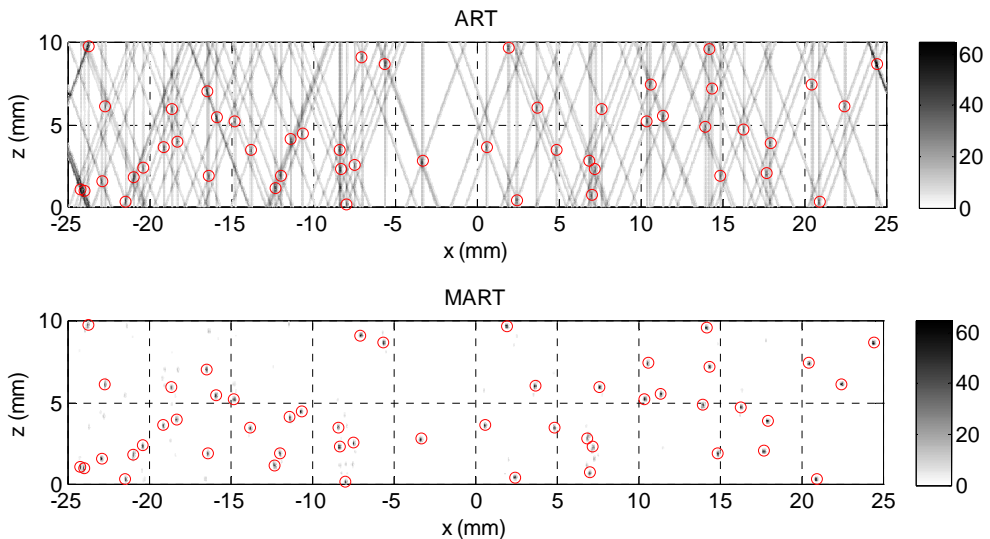


Figure 4.3: Particle field reconstructed using ART (top) and the same field reconstructed using MART (bottom). The actual particle positions are indicated by circles. The gray level represents the intensity level.

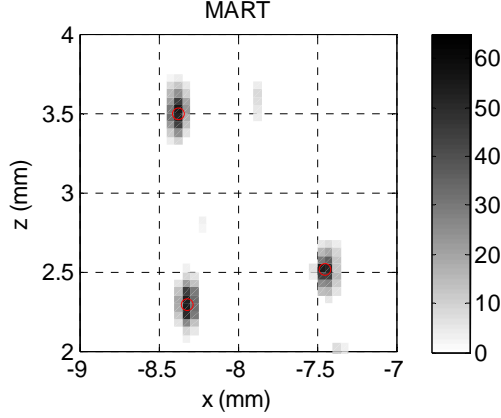


Figure 4.4: Detail of the MART reconstruction (figure 4.3) showing individual particles.

To quantify the accuracy of the reconstruction process, the reconstructed object $E_1(X,Z)$ is compared with the exact distribution of light intensity $E_0(X,Z)$ where the particles are represented by a Gaussian intensity distribution of 3 voxel diameter. The reconstruction quality Q is defined as the normalized correlation coefficient of the exact and reconstructed intensity distribution, according to:

$$Q = \frac{\sum_{X,Z} E_1(X,Z) \cdot E_0(X,Z)}{\sqrt{\sum_{X,Z} E_1^2(X,Z) \cdot \sum_{X,Z} E_0^2(X,Z)}} \quad (4.4)$$

A direct estimate of the correlation coefficient to be expected in the cross-correlation analysis of the reconstructed objects is therefore given by Q^2 in the assumption of perfect cross-correlation of the corresponding Gaussian particle fields and uncorrelated reconstruction noise.

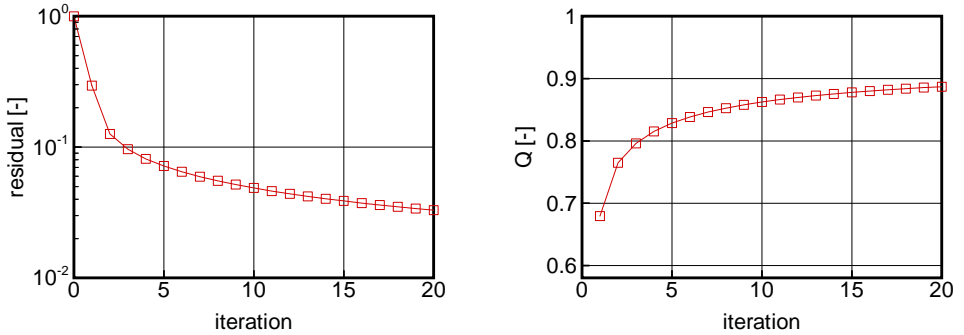


Figure 4.5: Convergence of the normalized residual (left) and the reconstruction quality (right).

First the convergence of the residual and the reconstruction is considered. The residual of the target equation Eq. 3.1 (figure 4.5-left) decreases monotonically in the tomographic iterative process. Although this behavior does not guarantee that the reconstructed object converges to the exact solution (Watt and Conery 1993), for the present reconstruction algorithm and noise free recordings, the solution converges correctly as evident from figure 4.5-right. A small tendency to divergence after 4 to 5 iterations was observed only for a noise level in the recordings in excess of 50% with respect to the particle peak intensity. Such divergence can be countered by applying a smaller relaxation ($\mu = 0.2$) as suggested by Mishra et al (1999), although that requires more iterations to reach a similar reconstruction quality Q . In the present parametric study and in the experiments presented later the reconstruction process is stopped after 5 iterations since both the residual and reconstruction quality Q do not change significantly performing further iterations. Moreover any divergence phenomenon is avoided. Furthermore the experimental results show that with additional iterations the returned vector field changes only within the noise level.

Figure 4.6 shows the dependence of the reconstruction quality Q on the different experimental parameters. The diagrams show clear trends, which provide the experimentalist with a first indication of the optimum experimental arrangement and the limitations of the system. A correlation coefficient of 75% with respect to the exact spatial distribution ($Q = 0.75$ corresponding to an expected cross-correlation coefficient of $Q^2 = 0.56$) is used as a cut-off value, above which the reconstruction should be considered sufficiently accurate.

The effect of the number of cameras (figure 4.6-A) is clear: adding camera gives additional information on the object, which increases reconstruction accuracy. A 2-camera system ($\theta = -20^\circ$ and 20°) is largely insufficient, whereas Q rapidly increases going to 3 and 4 cameras ($\theta = -20^\circ, 0^\circ, 20^\circ$ and 40°) and approaches unity with 5 cameras ($\theta = -40^\circ, -20^\circ, 0^\circ, 20^\circ$ and 40°).

The viewing angles are changed maintaining the symmetric camera arrangement. The angle indicated in figure 4.6-B is the angle between the outer cameras and the z -axis. The graph shows an optimum near 30° . For smaller angles the depth resolution decreases resulting in elongation of the reconstructed-particle in depth. For larger angles the length of the line-of-sight in the volume increases, which increases the probability of false particle triangulations hence increases of the number of ghost particles (section 4.1). The configurations returning an optimum have a viewing angle in the range of 15 to 45 degrees.

An increased particle density produces a larger percentage of ghost particles consequently decreasing the reconstruction quality. On the other hand, the larger number of particles allows a higher spatial sampling rate of the flow, returning a potentially higher spatial resolution. Therefore a high particle density is desirable. Based on the simulation results (figure 4.6-C) the maximum imaged particle density yielding an acceptable reconstruction quality is 0.075 and 0.15 particles per pixel for the 3 and 4 camera system respectively. In a 3D system this would approximately translate to 0.025 and 0.05 particles per pixel assuming each particle image spans three pixel lines. Moreover, figure 4.6-C shows that additional cameras (in the configuration mentioned above) allow a higher seeding density for a given reconstruction quality.

The effect of volume thickness l_z is shown in figure 4.6-D, where the thickness is normalized with the volume width l_x (constant at 1000 voxels). As expected from Eq. 4.3 the number of ghost particles increases with the volume thickness resulting in a decreasing

reconstruction quality Q . For the present system accurate reconstructions are obtained for volume thicknesses up to half the volume width. However in real experiments the depth of focus is expected to limit the achievable volume thickness.

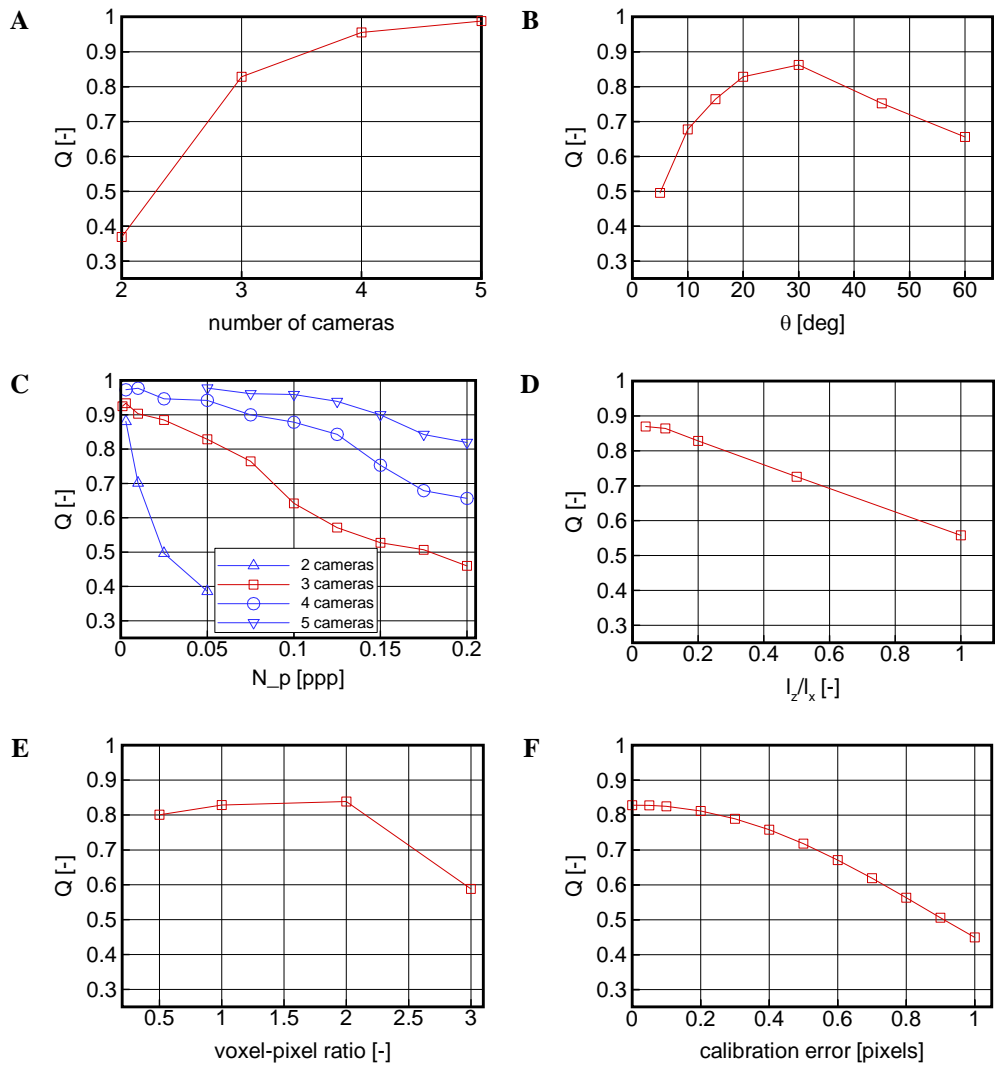


Figure 4.6: Reconstruction quality Q as a function of number of cameras (A), viewing direction (B), particle density (C), volume depth (D), voxel size relative to pixel size (E) and calibration accuracy (F).

The reconstruction resolution in voxels/mm is varied while maintaining constant imaging resolution in pixels/mm and volume size ($50 \times 10 \text{ mm}^2$). Then the voxel to pixel ratio is defined as the physical size of a voxel relative to the physical size of a pixel in the plane

of focus. From the results in figure 4.6-E it is seen that the reconstruction quality Q is insensitive to the voxel to pixel ratio over a wide range from 0.5 to 2. Therefore reconstructing the volume at low resolution using only a small number of voxels seems attractive, because it reduces the computational load in the reconstruction. However at low resolution the reconstructed particles span fewer voxel elements, which increases the risk of peak locking in the cross-correlation analysis introducing a bias error in the measured velocity (Raffel et al. 1998). The natural choice for the voxel to pixel ratio is one, because particles need to be properly discretized in the volume as it is done in the images. It is therefore suggested to reconstruct at a resolution equal to or slightly lower than the imaging resolution (voxel to pixel ratio < 1.3), so that the reconstructed particle diameter is 2 to 3 voxels.

In actual experiments calibration errors may occur, which result in a dislocation of the lines of sight in the reconstruction. As shown by Watt and Conery (1993) this reduces the accuracy of the reconstruction. To quantify the error and to find the necessary calibration accuracy, a calibration error is introduced after recording the images by displacing the center-camera towards the right and the right-camera to the left by an equal amount (being the calibration error). Lines of sight from the different cameras that originally intersected now form a triangle in the reconstruction volume. As seen from figure 4.6-F a calibration error of 0.4 pixel is the maximum acceptable for an accurate reconstruction. Stereo PIV calibration methods meeting this requirement have been developed for planar Stereo-PIV (Scarano et al 2005 and Wieneke 2005), which can reduce calibration errors to less than 0.1 pixel.

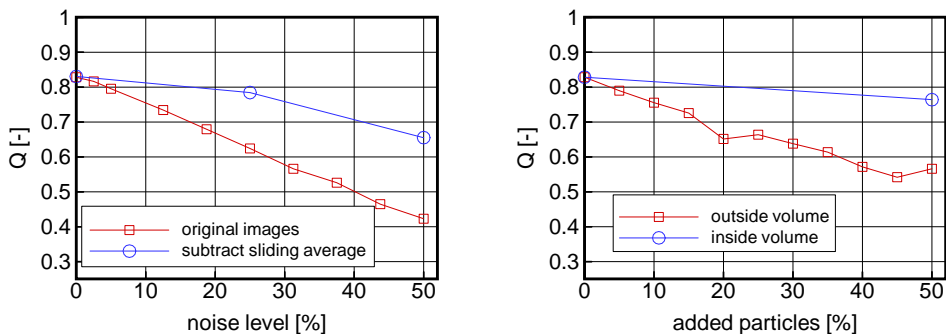


Figure 4.7: Effect on the reconstruction of white image noise (left) and unmatched particles (right).

Finally two types of image noise are considered: random noise added to the recordings and background particles, which are located outside the reconstruction volume. Figure 4.7-left shows the effect of random noise fluctuations, which range is expressed as a percentage of the particle peak intensity. The image noise deteriorates the reconstructed particle shape and increases the number of ghost particles, as noise is mistaken for particles. As a result the reconstruction quality Q strongly deteriorates with increasing random image noise. However image pre-processing can be applied to reduce the number of ghost particles. Subtracting a sliding average from the recording using a window of 61 pixels significantly improves the reconstruction results (figure 4.7-left). Random image noise up to 25% of the particle peak

intensity has only a small effect after pre-processing. For higher noise level (50%) the change of the particle image shape is important and cannot be recovered by the pre-processing. The effect of added background particles (located outside the volume) is compared with the same amount of particles added inside the volume in figure 4.7-right. This situation occurs when the reconstructed domain does not include all the illuminated particles either because the laser light sheet has a Gaussian profile or because of stray-light and uncontrolled reflections illuminating particles outside of the measurement volume. The particle located outside the volume have a stronger effect compared to the ones inside, therefore the reconstruction should include the entire illuminated volume to yield the best results.

4.3 Three-dimensional simulation

The numerical assessment of Tomographic-PIV in a 3D configuration is performed by simulation of the particle motion field around a ring vortex. The vortex core is located in the center plane $z = 0$ mm and forms a circle of 10 mm diameter. The analytical expression of the displacement field (in voxel units) d is given by:

$$d = \begin{Bmatrix} u \\ v \\ w \end{Bmatrix} = \frac{8R}{l} e^{-\left(\frac{R}{l}\right)} \quad (4.5)$$

where R is the distance to the vortex axis center ring and $l = 2$ mm is a length scale that defines the core radius of the vortex. The maximum displacement is 2.9 voxels. Inside the $35 \times 35 \times 7$ mm³ measurement volume 24,500 particles are distributed, which are imaged by four cameras placed at infinity. Each camera has a 30° viewing angle (to the left, to the right, upward and downward) and records the images onto 700x700 pixels. Consequently the particle image density is 0.050 particles per pixel. Furthermore the magnification is 1 and the particle image diameter is 3 pixels.

The measurement volume is reconstructed at 700x700x140 voxel resolution performing 10 iterations and $\mu = 1$. The returned reconstruction quality Q is 0.75. The reconstruction accuracy can be further assessed by counting the number of intensity peaks or particles. Each reconstructed object contains 24,400 actual particles (peaks within 1.5 voxel radius in the correct position) and 91,600 ghost particles considering only peaks values above 10 in arbitrary units. Even though the number of ghost particles exceeds significantly the number of actual tracer particles, their peak intensity I_p is lower as shown by the probability density function of peak intensity (figure 4.8). The expected peak intensity for an actual particle is 70 against 23 for a ghost. Therefore the contribution of the ghost particles to the cross-correlation map, hence velocity measurement, is limited.

The estimated reconstruction signal to noise ratio based on Eq. 4.3 is 2.4% corresponding to 42 ghosts per particle (using 0.05 ppp, $A_p = 3^2\pi/4 = 7$ pixels and $l_z = 140$ voxels), which clearly is an overestimate of the actual numbers. The estimate can be improved by considering only reconstructed particles at or above a chosen peak intensity, 70 counts say, which is the expected value of the actual particles and approximately 50% of the maximum particle peak intensity. Such a threshold is motivated by the fact that particles with a higher intensity I_p yield a larger contribution (order I_p^2) to the cross-correlation peak

hence can be considered more important. When only the particles with a peak intensity of 70 counts are considered the number of ghosts per particle reduces to 0.38, which would correspond to $A_p = 2.2$, 0.05 ppp and $l_z = 140$ voxels in Eq. 4.3. So it seems A_p is best chosen as the area representing the particle image peak. Furthermore the returned value for A_p agrees well with the experimental results presented in section 5.3.

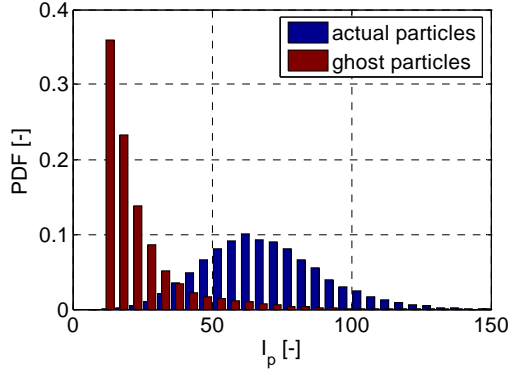


Figure 4.8: PDF of particle peak intensity for actual and ghost particles in the reconstructed objects.

The displacement field is obtained from the reconstructed object using a 3D extension of the WIDIM algorithm (Scarano and Riethmuler 2000) with 41^3 voxels interrogation volumes at 75% overlap. Therefore each interrogation volume contains on average 25 particle tracers. The measured vector field contains $66 \times 66 \times 10$ vectors shown in figure 4.9-left where the overall motion pattern is well captured. The surface corresponding to a vorticity magnitude of 0.13 voxels/voxel returns the expected torus. Figure 4.9-right presents the vectors in the cross section at $x = 0.25$ mm with the corresponding vorticity in x -direction (contours), where the flow symmetry and the two vortex sections are clearly visible. The normalized cross-correlation peak value is 0.56 and the mean signal-to-noise ratio exceeds 5 indicating a high confidence level for the measurement in such configuration.

The measurement accuracy is presented in the form of 2D scatter plots of the displacement error (figure 4.10), where 90% of the vectors have an absolute error smaller than 0.10 voxels in u and v and less than 0.16 voxels in w (the slightly larger uncertainty in depth direction is due to the 30 degrees viewing direction). The asymmetric scatter plot of the error on the w component (figure 4.10-right) appearing as a bias error results from the limited spatial resolution (modulation error) in combination with the asymmetric w distribution in the flow field. Such bias also appears when cross-correlating the exact distribution of light intensity $E_o(X,Y,Z)$ and is therefore not associated to the reconstruction process.

From the synthetic 3D experiment it can be concluded that Tomographic-PIV is capable of the instantaneous measurement of flow structures at a good resolution and accuracy.

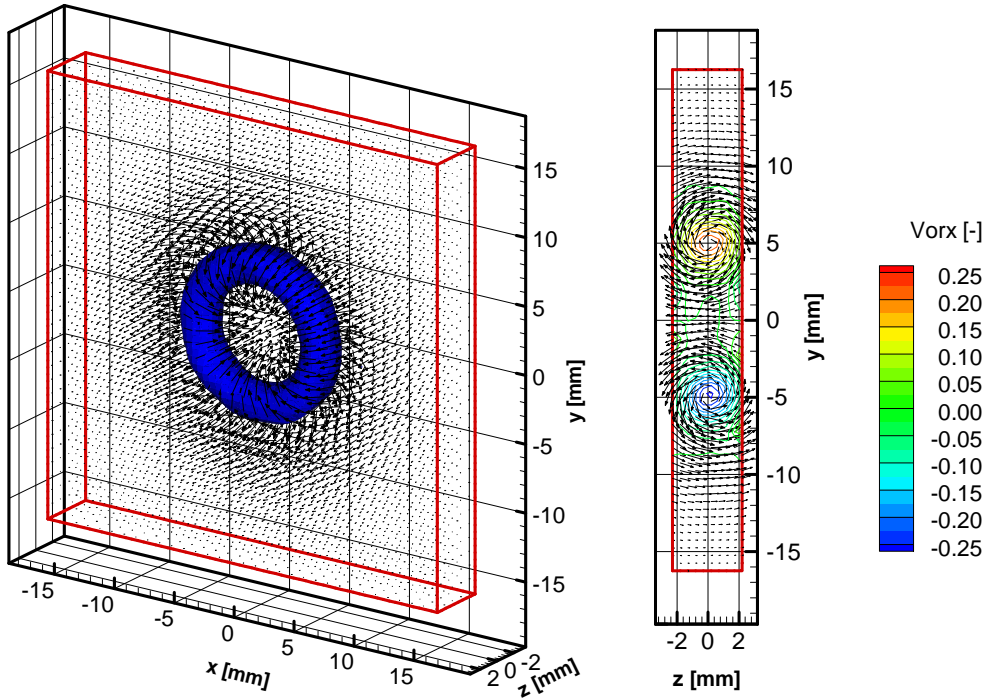


Figure 4.9: Velocity field and iso-vorticity surface (0.13 voxels/voxel) from a simulation of a vortex ring (left) and velocity vectors in the cross section at $X = 0.25$ mm (right) the contours show the vorticity in x -direction (in voxels/voxel).

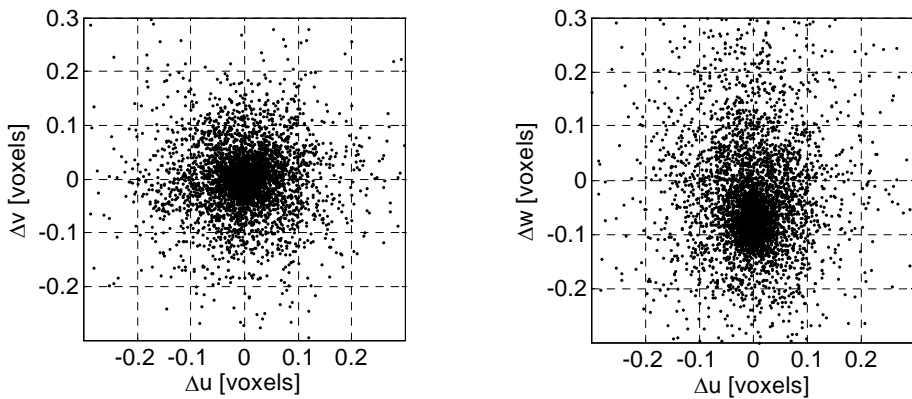


Figure 4.10: Scatter plots of the particle displacement error. Left: x and y displacement. Right: x and z displacement.

4.4

Conclusions

The numerical simulations presented in this chapter have shown that the MART algorithm is well suited for particle reconstruction returning distinct particles with limited artifacts. Furthermore, it has been shown that the reconstruction converges to the desired solution for noise free particle image recordings.

Based on a theoretical and numerical study the number of cameras, particle image density, volume depth, calibration errors and image noise are identified as critical to the reconstruction accuracy. The effects of these parameters are quantified in a parametric study, which results are presented in figures 4.6 and 4.7. The graphs provide clear trends that can be used by the experimentalist as a first indication of the optimum experimental arrangement and the limitations of the system. It is concluded that the calibration must be accurate within 0.4 pixel. Furthermore image-preprocessing (e.g. removing the background intensity) reduces the effect of random noise. And finally adding a camera to the system provides extra information, which can be used to increase the measurement resolution (increasing particle density) or accuracy.

A 3D simulation of a vortex ring flow has shown that the 3D measurement configuration with four cameras can yield $66 \times 66 \times 10$ vectors in a $35 \times 35 \times 7 \text{ mm}^3$ volume with a typical measurement error of 0.1 pixel particle displacement.

Chapter 5

Experimental assessment

The experimental validation and assessment of the Tomographic-PIV technique in this chapter is based on the measurement of a circular cylinder wake flow, which is an attractive test case, because the flow is clearly 3D at high enough Reynolds number and contains well defined large vortical structures. In the assessment both the accuracy of the tomographic reconstruction and the measured velocity will be considered for varying light sheet thicknesses and particle densities. First the reconstruction accuracy is quantified by determining the number of ghost particles, which will be compared with the theoretical estimates from the previous chapter. Then the velocity accuracy is determined from an assessment of the cross-correlation maps and a direct comparison of the velocity statistics with results obtained by stereo-PIV. Finally the instantaneous velocity and vorticity fields will be compared with data from literature.

5.1

Circular cylinder wake flow

To aid interpretation of the results presented later in this chapter, a brief introduction to the basic properties of the cylinder wake flow are given here, which is largely based on the review article by Williamson (1996). In cylinder flow, transition to turbulence starts in the wake and then progressively moves upstream to the shear and boundary layer (figure 5.1) as the Reynolds number based on the cylinder diameter Re_D is increased. The present measurements are performed in the flow regime where transition occurs in the shear layers, which ranges from approximately $Re_D = 1,000$ to $200,000$. At this stage, the wake is unsteady and characterized by the shedding of alternate vortices, which are called primary or Kármán vortices, and by a secondary instability mode (referred to as *Mode B* instability). The instability comprises counter-rotating streamwise vortex pairs or secondary vortices (figure 5.2), which are characterised by a spanwise wavelength $\lambda_z/D = 1$ (Brede et al. 1996). These streamwise vortex structures of *Mode B* behave laminar at $Re_D < 1,000$, but become less ordered at the onset of shear layer transition. In particular, the three dimensional wake structures are of the scale of the Kármán vortices as well as the shear layer vortices.

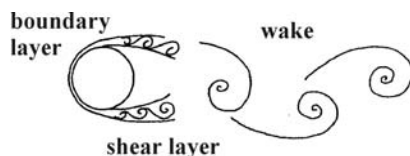


Figure 5.1: Flow regions in the unsteady cylinder wake [from Williamson 1996]

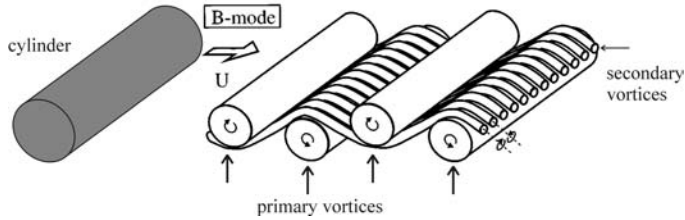


Figure 5.2: Conceptual sketch of the 3D vortical structures in the cylinder wake for mode B [adapted from Brede et al. 1996].

5.2

Experimental setup

The experimental validation of the technique is performed in a low-speed open-jet wind tunnel with a $0.40 \times 0.40 \text{ m}^2$ square cross section. The wake behind a circular cylinder is measured at $Re_D = 2700$ where the diameter D is 8 mm and the free stream velocity is 5 m/s. The cylinder axis is oriented horizontally, normal to the light sheet (figure 5.3-left).

Measurements are performed for varying light sheet thickness (2, 4, 8 and 12 mm) and seeding density level (ranging from 0.01 to 0.1 ppp) to determine the effect of each experimental parameter on the accuracy of Tomographic-PIV. The width and height of the measurement volume is kept constant at 36.5 and 35.8 mm respectively (667×654 voxels). The particle image density in the recordings is evaluated by counting intensity peaks above a threshold (9 counts, after background subtraction).

Two cameras from the four-camera imaging system are used to return Stereo-PIV results for the 2 mm light sheet. Self-calibration on the particle images (Wieneke 2005) is applied to improve the Stereo-PIV results. Because the mean flow repeats itself along the cylinder axis, a single plane is sufficient to measure the mean flow properties (average and RMS velocities) thus a scanning light sheet system is not necessary. The mean flow thus obtained will be compared with Tomographic-PIV in section 5.6, for which the measured velocity is expected to be uniform in z (the direction of the cylinder axis).

Additionally, measurements have been performed with the cylinder axis oriented vertically, parallel to the laser propagation direction in order to match the largest dimensions of the 8 mm thick measurement volume with the streamwise and spanwise coordinates (figure 5.3-right). This choice still allows to measure the Kármán vortices along the wake thickness since the measurement volume is one diameter deep.

The flow is seeded with $1 \mu\text{m}$ droplets to the required particle image density. The illumination source is a Quanta Ray double cavity Nd:YAG laser from Spectra-Physics with a pulse energy of 400 mJ. A slit is added in the path of the laser light sheet to cut the low intensity side lobes from the light profile and create a sharply defined illuminated volume thickness. The time separation between light pulses is $35 \mu\text{s}$ yielding a free stream particle displacement of 0.18 mm corresponding to 3.2 voxels.

A 4-camera system (figure 5.3) is used to record 12-bit images of the tracer particles at 1280×1024 pixels resolution from different directions. The image resolution is approximately 18.3 pixels/mm. The cameras are equipped with Nikon objectives set at $f/8$. Scheimpflug adapters are used to align the mid-plane of the illuminated area with the focal

plane. The effective field of view common to all cameras is $50 \times 50 \text{ mm}^2$. Table 5.1 lists the properties specific to each camera, such as the magnification M , the focal length f and the viewing angles θ_x and θ_y in horizontal and vertical direction respectively.

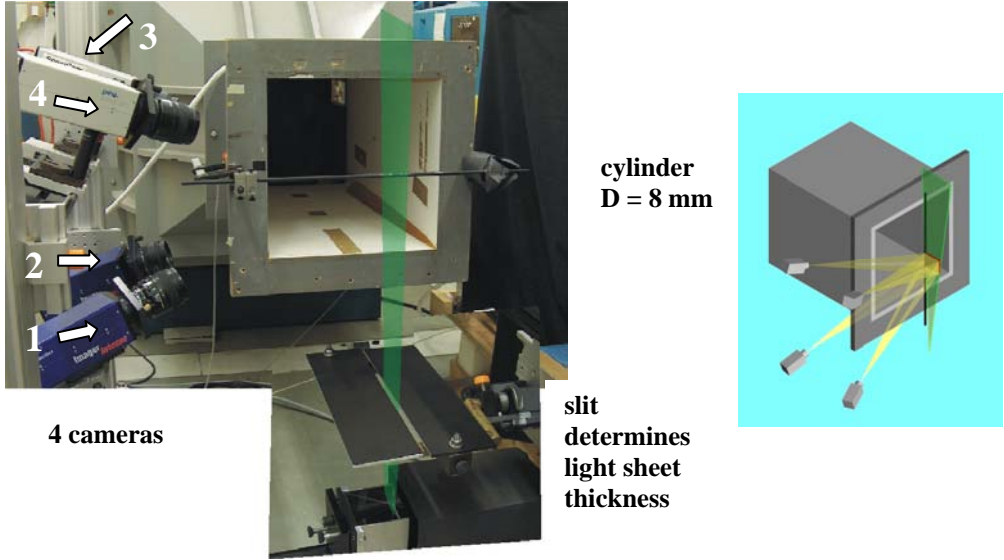


Figure 5.3: The optical arrangement for the Tomographic-PIV experiments in the low speed wind tunnel. Left: horizontal cylinder. Right: vertical cylinder.

Table 5.1: Imaging system parameters

camera #	camera type	pixel pitch (μm)	M (-)	f (mm)	θ_y (deg)	θ_x (deg)
1	Imager Intense	6.45	0.13	60	+20	+22
2	Imager Intense	6.45	0.12	50	-10	+22
3	SensiCam	6.7	0.12	50	-10	-22
4	SensiCam QE	6.45	0.14	60	+20	-22

The imaging system is calibrated by scanning a plate with 15×12 marks (crosses) through the volume in depth direction in steps of 4 mm over a total range of 8 mm. In each of the three calibration planes the relation between the physical coordinates (X, Y, Z) and image coordinates is described by a 3rd order polynomial fit. Linear interpolation is used to find the corresponding image coordinates at intermediate z -locations. The calibration accuracy is approximately 0.2 pixels based on an a-posteriori evaluation using the volume self-calibration procedure described in section 3.4. Note that the volumes have been reconstructed using the original and not the corrected calibration.

The reconstruction process is improved by means of image pre-processing with background intensity removal, particle intensity equalization and a Gaussian smooth (3×3 kernel size), as described in the previous chapter (section 4.2).

The intensity distribution in the measurement volume is reconstructed at 18.2 voxels/mm resolution using the MART algorithm with 5 iterations and with the relaxation parameter $\mu=1$. For the 8 mm thick light sheet the dimensions of the reconstructed volume are 36.5(Length) \times 35.8(Height) \times 11(Depth) mm corresponding to 667 \times 654 \times 203 voxels. For the other cases the reconstruction volume thickness is scaled according to the light sheet thickness. Note that the reconstructed volume depth is slightly larger than the light sheet thickness (approximately 150 voxels) to ensure that the complete 8 mm light sheet is contained, which is important for accurate reconstruction. Figure 5.4 shows an example of a reconstructed volume. The light sheet position can be clearly identified within the reconstructed volume due to the application of a slit in the light path.

The particle displacement is obtained using a 3D FFT-based cross-correlation algorithm with iterative multigrid and window deformation (Scarano and Riethmuller 2000). The analysis returned 77 \times 79 \times 15 velocity vectors using an interrogation volume size of 31³ voxels with 75% overlap. Data validation based on a signal-to-noise ratio threshold of 1.2 and on the normalized median test with a maximum threshold of 2 (Westerweel and Scarano 2005) returns 5% spurious vectors. The average signal-to-noise ratio and normalized correlation coefficient are 3.3 and 0.6 respectively for a particle image density of 0.05 ppp.

5.3 Accuracy of the tomographic reconstruction

In real experimental conditions an assessment of the reconstruction quality is not straightforward, since the actual particle distribution is unknown. It is possible, however, to estimate the number and intensity distribution of the ghost particles by comparing the light intensity reconstructed outside and inside the illuminated region (representing reconstruction noise and signal plus noise respectively). Note that the light sheet position can be clearly identified within the reconstructed volume (figure 5.4) due to the application of a slit in the light path.

Because ghost particles are formed when the particle images from all recordings triangulate in points where there is physically no particle, they can occur anywhere in the reconstructed volume with a constant probability, also outside the light sheet. Consequently the reconstructed intensity distribution outside and inside the light sheet represents the reconstruction noise (ghosts) and actual particles plus noise respectively. The ghost particle density can therefore be determined by counting the intensity peaks outside the light sheet. The corresponding intensity values return the probability density function (PDF) of the ghost particle peak intensity. The same procedure is followed inside the light sheet returning the particle density and peak intensity of the actual and ghost particles combined. Finally the difference (inside the light sheet minus outside) provides the values for the actual particles in the reconstruction. In the particle detection the volume is cropped to 560 \times 550 voxels in *X* and *Y* direction to remove border effects (figure 5.4) and only intensity peaks above a threshold (5 counts) are counted.

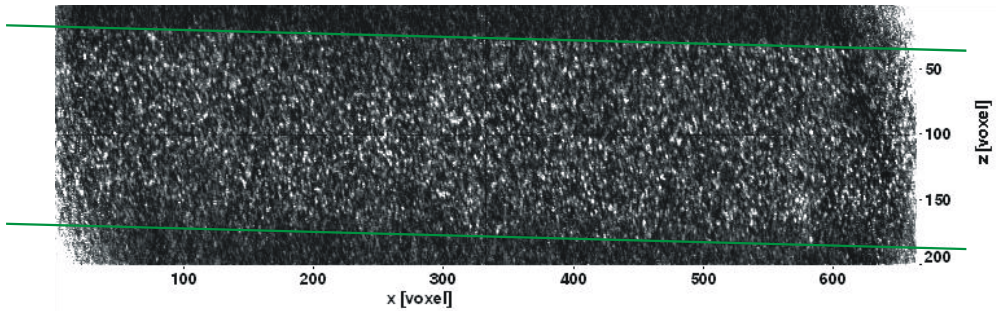


Figure 5.4: Top view of the reconstructed volume showing the light intensity integrated in y -direction. The green lines indicate the position of the 8 mm thick light sheet (0.03 ppp).

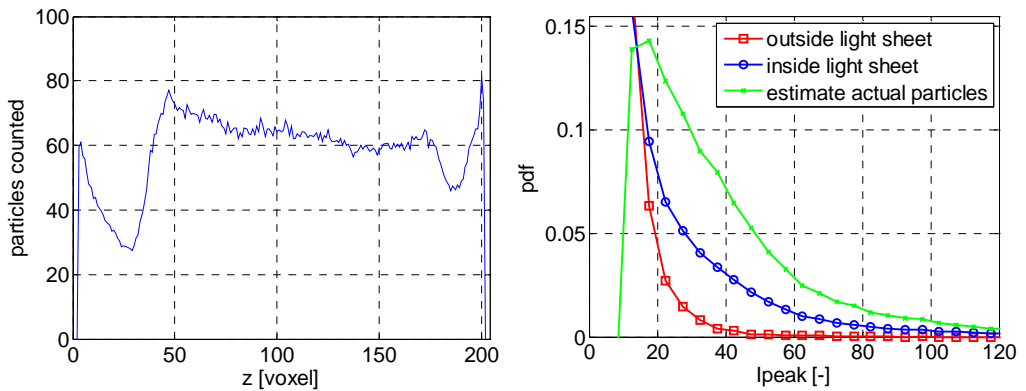


Figure 5.5: Distribution of intensity peaks in depth (left) and PDF of the peak intensity inside, outside the light sheet and actual particles (right) for an 8 mm thick light sheet and a seeding density of 0.019 ppp . The plots present results averaged over 40 reconstructed objects.

The distribution of the intensity peaks in the reconstructed volumes plotted against the depth-coordinate (figure 5.5-left) shows that well inside the light sheet ($z = [35, 185]$ voxels) there are on the average 65 peaks or particles in each z -layer of the reconstructed volume, while outside ($z = [20, 30]$ voxels) approximately 30 peaks are returned. Assuming the latter value is the ghost particle density, it is concluded that inside the light sheet there are 35 actual particles per unit depth, which means 54% of the intensity peaks correspond to actual tracer particles. Furthermore border effects are observed, which increase the number intensity peaks towards the edges of the volume. Note that such an effect is not observed in figure 5.4 (intensity integrated in y -direction), because the additional particles have a relatively low intensity. For $z > 185$ voxels the number of particles does not return to 30 per slice, because the light sheet is misaligned with the coordinate system so that part of the z -slice is still in the light sheet (figure 5.4).

To check consistency between the number of particles in the recordings and in the reconstruction, the total number of particles in the considered volume is computed. Based on

the recordings the total number of particles is $ppp \cdot l_x \cdot l_y = 0.019 \cdot 560 \cdot 550 = 5852$. In the reconstructed volume 5285 actual particles are counted between $z = 35$ and 185 voxels, which is in good agreement with the recorded number of particles in the images. It is therefore concluded that the properties of the actual particles in the reconstructed volume can be inferred from a comparison of particles inside and outside the laser sheet.

The PDF of the particle peaks intensity (figure 5.5-right) reveals that inside the light sheet the expected peak intensity is higher than outside, which means the real particles have a higher peak intensity compared to the ghost particles and reconstruction noise. This finding is in agreement with results of synthetic Tomographic-PIV experiments (figure 4.8). It is seen from figure 5.5-right that the actual particles have an average peak intensity of approximately 50 counts. Moreover figure 5.6 presents the effect of particle image density in ppp on the ghost and actual particle intensity. It is found that the average peak intensity of the ghost particle increases with ppp , while the average intensity of the actual particles decreases slightly: intensity is transferred from the actual particles to the ghosts.

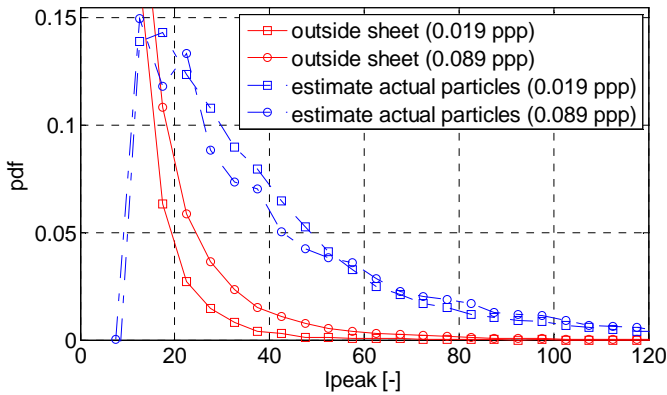


Figure 5.6: Comparison of the PDF of the peak intensity outside the light sheet and actual particles for an 8 mm thick light sheet and a seeding density of 0.019 and 0.089 ppp.

The ratio of actual tracer particles N_p and ghost particles N_g is determined at the average peak intensity of the actual particles ($I_{peak} = 50$). Figure 5.7 presents N_p/N_g versus the particle image density in the recorded particle images ppp for the light sheet thicknesses 4, 8 and 12 mm. The number of actual particles per ghost particle decreases with ppp and light sheet thickness as expected. The number of ghosts equals the number of actual particles at $ppp = 0.15$, 0.062 and 0.044 for light sheet thickness 4, 8 and 12 mm respectively. Furthermore, the ratio N_p/N_g is proportional to ppp^{-3} , as predicted for a 4-camera system (Eq. 4.3), is observed for $1 < N_p/N_g < 10$. In this range Eq. 4.3 is fit to the curves to obtain the effective particle image area A_p (l_z , N and ppp are known), which is found to increase with the light sheet thickness (table 5.2). It is believed that this is due to the reduced signal-to-noise ratio in the recordings, which is not taken into account. The particle image intensity in the recordings reduces (figure 5.8) due to the expansion of the light sheet with consequent drop in light intensity. Consequently image noise, hence reconstruction noise, increases relative to the actual particle intensity, which shows as an increase of A_p in the above fits. Furthermore the depth of focus is approximately 12 mm, which means the geometric particle

image diameter equals the diffraction spot for particles near the edges of the 12 mm laser sheet. Hence the total particle images diameter increases and the peak intensity decreases for these particles, which also results in a decrease of the signal-to-noise ratio in the recordings.

In conclusion: the results show that the maximum ppp still returning accurate reconstructions can be predicted a-priori using Eq. 4.3 with a reasonable estimate of the effective particle image area A_p . Alternatively figure 5.7 can be used directly for experimental configurations similar to the present one. Note that the present curve may depend on calibration accuracy and signal-to-noise ratio in the recorded images.

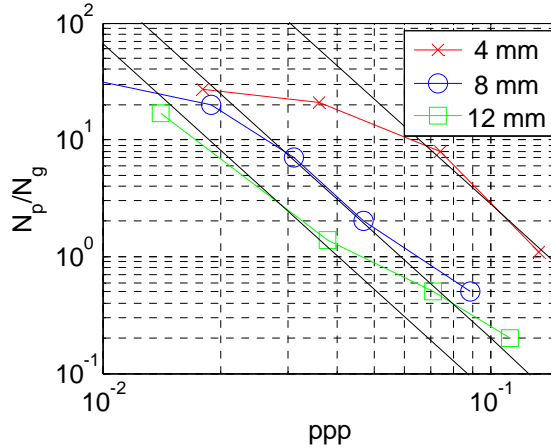


Figure 5.7: Ratio of actual tracer particle versus ghost particles for varying particle image density and light sheet thickness. Black lines indicate fits of the theoretical relation of Eq. 4.3.

Table 5.2: Parameters in fit Eq. 4.3 to curves in figure 5.7

Light sheet thickness [mm]	l_z [voxels]	A_p [pixels]
4	78	1.5
8	150	2.4
12	210	2.9

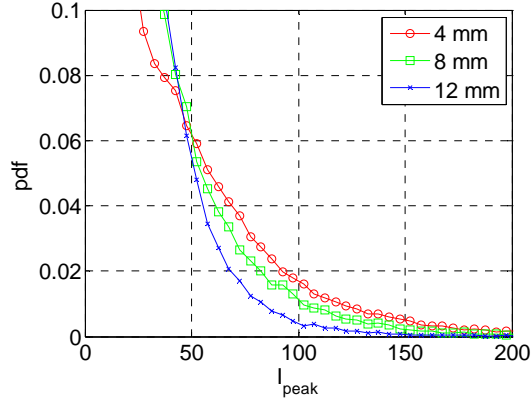


Figure 5.8: PDF of the peak intensity in the recordings for different light sheet thicknesses.

5.4

Assessment of the velocity measurement

The velocity accuracy will be assessed based on the results for the 8 mm thick light sheet and considering three values for the recorded particle image density: 0.02, 0.05 and 0.08 *ppp*. These three seeding densities cover the full range from a very good to a very noisy tomographic reconstruction of the particles, as shown above.

However, before presenting the final velocity vector fields, the cross-correlation maps are discussed, which provide the link between the reconstructed particle volumes and the measured velocity vector. In the cross-correlation analysis, 5 iterations with window deformation are used with spline volume intensity interpolation and 31^3 voxels interrogation volumes returning cross-correlation maps of identical size. Two typical examples are presented in figure 5.9 showing a correlation map in the last iteration for 0.02 (left) and 0.08 *ppp* (right). In the last iteration the update of the particle displacement is expected to be small, therefore the highest, primary correlation peak will be close to the origin (zero displacement) as is the case in figure 5.9. Moreover, these correlation maps have been obtained outside the wake in a region of relatively uniform flow conditions (labeled *B* in figure 5.10), so that correlation peak spreading related to velocity gradients is negligible. As expected, the number of peaks (shown by the blue iso-surfaces) increases with the number of particles in the correlation volume. However, the cross-correlation signal-to-noise ratio (defined as the ratio of the highest and the second highest correlation peak) is similar at 3.8 and 3.7 for 0.02 and 0.08 *ppp* respectively. Furthermore, it is seen that the primary peak near the origin is elongated in depth (*z*-direction). Based on the 0.1 correlation coefficient iso-surface (blue) the primary peak width in depth is estimated at 7.5 (0.02 *ppp*) and 11 voxels (0.08 *ppp*), while in the other directions the width is approximately 4 voxels. The increase in size of the correlation peak can be regarded as a sign of reduced reconstruction accuracy.

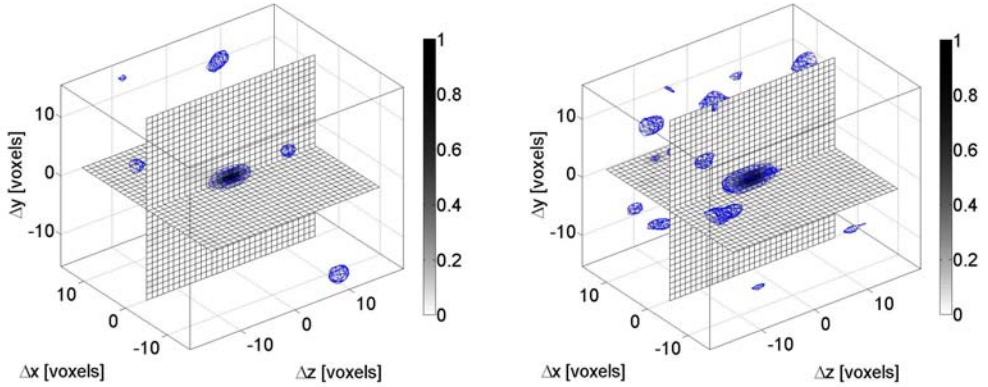


Figure 5.9: Correlation maps for the 8 mm light sheet with seeding densities 0.02 (left) and 0.08 (right) showing planar cuts (mesh) with cross-correlation coefficient in gray and iso-surfaces of constant correlation coefficient (value 0.1, blue).

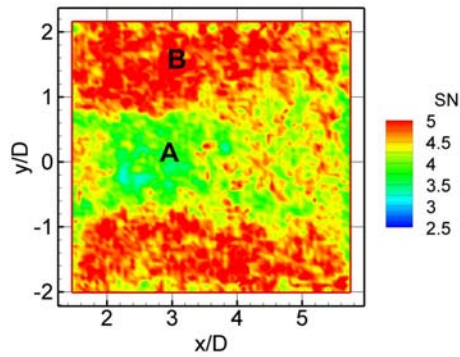


Figure 5.10: Average cross-correlation signal-to-noise ratio in the mid-plane in the 8 mm light sheet for 0.02 *ppp*.

Table 5.3: Cross-correlation signal-to-noise ratio at two different locations in the volume

ppp	estimated average number of actual particles per correlation volume	estimated average number of ghost particles per correlation volume	SN in wake region (A)	SN in outer flow (B)
0.02	4.7	0.25	3.9	5.0
0.05	12	6.3	3.3	4.2
0.08	19	23	3.8	4.8

Figure 5.10 presents the average cross-correlation signal-to-noise ratio in the measurement volume mid-plane for a seeding density of 0.02 *ppp*. A single plane in this case is sufficient, because the variations over the volume depth are insignificant. The figure

shows a relatively high signal-to-noise ratio ranging from 4 in the wake region (labeled *A*) to 5 in the outer flow (labeled *B*). The observed variation can be directly related to the velocity gradient levels, which are relatively high in the wake causing correlation peak broadening and are small in the outer flow. It is well known from planar PIV that peak broadening reduces the primary peak height hence the signal-to-noise ratio.

The cross-correlation signal-to-noise ratio is expected to increase linearly with the number of tracer particles per interrogation volume (or seeding density) at first approximation. However, the reconstruction noise (i.e. the number of ghost particles) also increases strongly with the number of actual particles, as demonstrated in the previous section, which has the effect of reducing the signal-to-noise ratio. To see the relative importance of these opposite effects, table 5.3 gives the estimated number of actual tracer particles and ghost particles with the returned cross-correlation signal-to-noise ratios in the wake and outer flow. When the results for the lowest and highest seeding density are compared, a relatively small (0.2) drop in the signal-to-noise ratio is seen suggesting that both effects largely cancel each other. For the intermediate seeding density (0.05 *ppp*) the overall signal-to-noise ratio is lower, however the returned values may still be considered relatively high for PIV measurements. The observed decrease at 0.05 *ppp* is unexpected since the number of actual tracer particles is larger than the number of ghosts, whereas for 0.08 *ppp* with a higher signal-to-noise ratio, the ghosts outnumber the actual particles. A possible explanation of this out-of-trend behavior may be given by the lower dynamic range (8-bit) at which the volumes are stored for the 0.05 *ppp* case compared to the 16-bit range used for the other cases (0.02 and 0.08 *ppp*). Given the high signal-to-noise ratio for all three seeding densities with only a small difference between the results for the lowest and highest seeding density, it is concluded that the cross-correlation signal-to-noise ratio is insensitive to the seeding density, hence tomographic reconstruction accuracy, over the range considered. These results again illustrate the robustness of the correlation approach in PIV.

5.5

Quantitative comparison with Stereoscopic PIV

The accuracy of the Tomographic-PIV technique is investigated by comparing the flow statistics with measurements made with Stereoscopic-PIV. The ensemble for both techniques consists of 100 snapshots obtained in the horizontal cylinder configuration (figure 5.3-left), from which the velocity statistics are obtained at confidence levels exceeding 90%. The limited ensemble size is due to the fact that tomographic reconstruction and interrogation operations are time consuming. Stereo-PIV results are obtained using two cameras from the above imaging system and a 2 mm thick light sheet. In the cross-correlation analysis 32×32 pixel interrogation windows are used at 75% overlap yielding a spatial resolution comparable to Tomographic-PIV. Furthermore, self-calibration on the particle images (Wieneke 2005) is applied to eliminate light-sheet misalignment errors in Stereo-PIV.

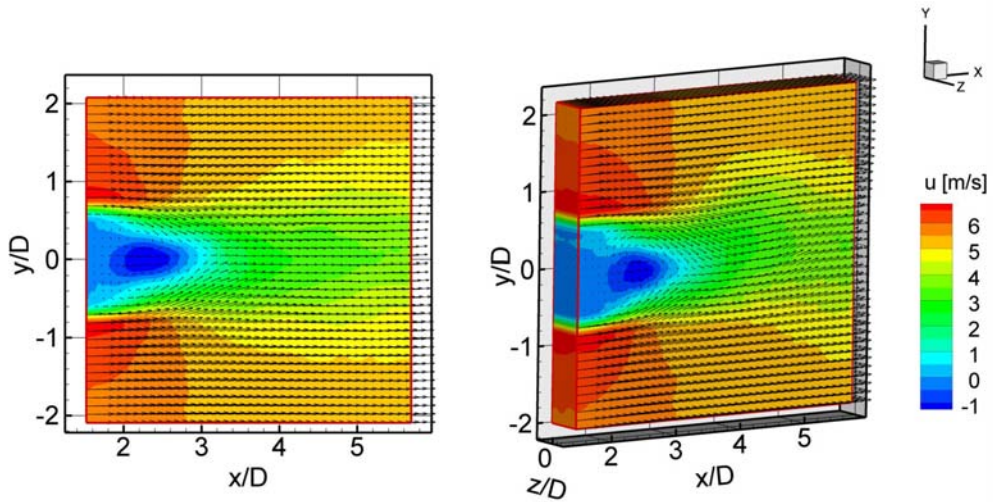


Figure 5.11: Mean velocity distribution obtained by Stereo (left) and Tomographic-PIV (8 mm light sheet and 0.05 *ppp*, right).

The average velocity distribution returned by Tomographic-PIV (figure 5.11-right) is uniform along the cylinder axis, as expected, and shows a good qualitative agreement with stereo-PIV data (figure 5.11-left). Both velocity fields clearly show the two shear layers emanating from the upper and lower part of the cylinder ($y/D = \pm 0.5$). The shear layer reattach at $x/D = 2.8$, $y/D = 0$ enclosing the circulation region with reversed flow. After the point of reattachment the width of the wake increases and the velocity deficit decreases. It is observed that the wake is not symmetrical as expected, which is most likely due to an insufficient number of samples. Finally the maximum value for the u -component of velocity in the present part of the wake is 6.6 m/s, which is found in the outer flow region ($x/D = 1.8$, $y/D = \pm 0.8$).

To compare the results quantitatively, vertical profiles (at $x/D = 3.0$) of the mean and RMS fluctuations of the streamwise velocity component are extracted from the data (figure 5.12). The overall agreement between Stereo and Tomographic-PIV is good with the largest difference in the mean u of 0.50 m/s, corresponding to 0.30 voxel particle displacement. The RMS profiles for the u -component agree within 0.30 m/s. Wieneke and Taylor (2006) have confirmed this level of agreement based on measurements of a vortex ring. It is interesting to observe that the present tomographic results show very little variation with respect to the particle image density in the range of 0.02 to 0.08 *ppp*. Even when the number of ghost particles in the volume is larger than the number of actual tracer particles as is the case for 0.08 *ppp*.

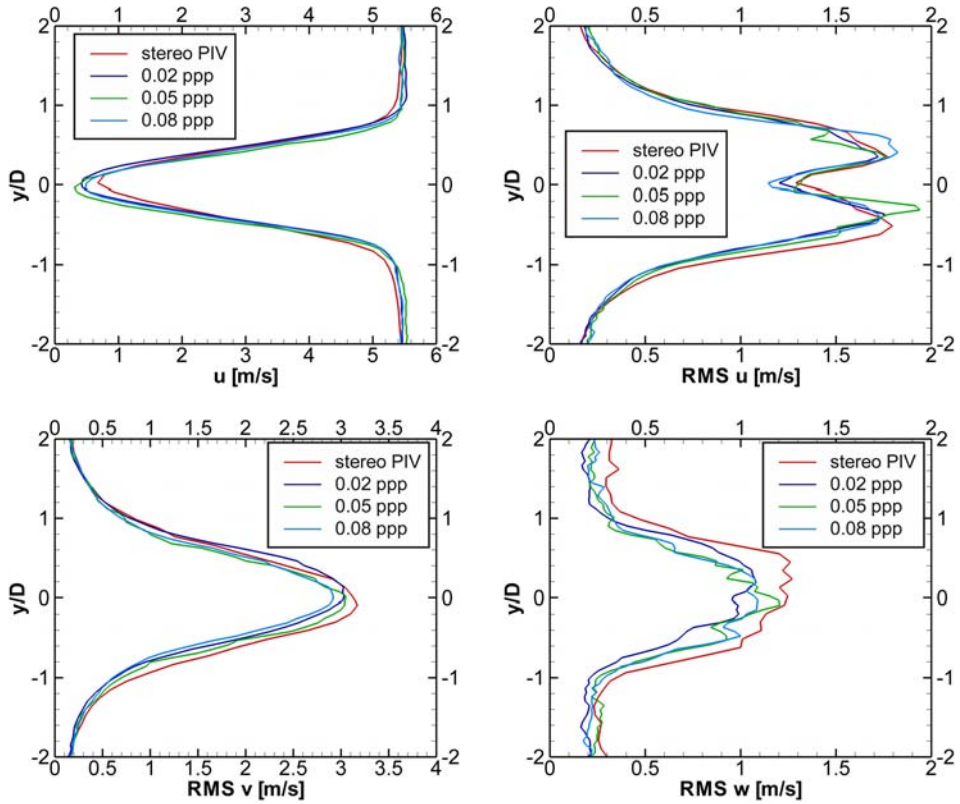


Figure 5.12: Profiles of the u -component of velocity, mean (top-left) and RMS (top-right), and RMS velocities of the v - (bottom-left) and w -components (bottom-right) at $x/D = 3.0$. Comparing Tomographic-PIV at different seeding densities with Stereo-PIV.

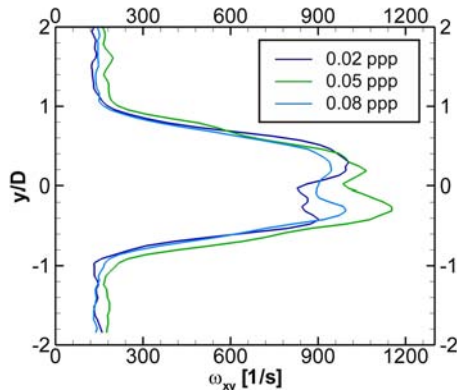


Figure 5.13: Profiles of the mean in-plane-component of vorticity $\omega_{xy} = \sqrt{\omega_x^2 + \omega_y^2}$ at $x/D = 3.0$. Comparing Tomographic-PIV at different seeding densities.

In many 3D flow investigations, including the present study, the instantaneous flow organization is visualized using derived quantities such as vorticity. To investigate the dependence of the returned vorticity levels on the particle image density, vertical profiles (at $x/D = 3.0$) of the mean in-plane vorticity magnitude $\omega_{xy} = \sqrt{\omega_x^2 + \omega_y^2}$ are plotted (figure 5.13).

The in-plane component of vorticity results from velocity variations over the volume depth, i.e. secondary vortices (figure 5.2), and therefore is a relevant measure for Tomographic-PIV's capability to yield truly three-dimensional velocity data. The velocity gradients needed to compute the vorticity vector have been obtained from the measured velocity distribution by a second order regression over a $5 \times 5 \times 5$ kernel (see section 7.3.1 for details). Figure 5.13 shows similar vorticity levels for the three seeding densities especially considering the limited statistics, i.e. number of snapshots. The profiles are found to agree within 300 s^{-1} corresponding to a 0.011 voxels/voxel particle displacement gradient. In the outer flow region the profiles display a plateau, where the vorticity levels off to a value of approximately 150 s^{-1} corresponding to a 0.005 voxels/voxel particle displacement gradient. This value can be regarded as a measure for the accuracy of the vorticity vectors, since the in-plane vorticity is expected to go to zero in that part of the flow. Furthermore, it is observed that the vorticity for the intermediate seeding density (0.05 ppp) is overall higher, which may be related to the lower cross-correlation signal-to-noise ratio for that case. Based on the vorticity profiles, it can be concluded that the 3D velocimetry capability seems to depend little on the seeding density over the range considered. This conclusion is supported by the instantaneous flow volumes, similar to those presented in the following section for 0.05 ppp , all showing comparable levels of vorticity.

5.6

Instantaneous velocity results

The Tomographic-PIV measurements are validated further by inspection of the instantaneous flow fields for a seeding density of 0.05 ppp and a comparison of the results with the flow organization reported in literature. An instantaneous velocity and vorticity field is shown in figure 5.14-left. The separated shear layer is visible in form of a vorticity sheet emanating from the upper and lower side of the cylinder. On the bottom side of the wake a counter clockwise roller is being formed as also indicated by the swirling pattern of the instantaneous velocity vectors. The previously shed primary roller can be identified with the roll-up of the vorticity sheet on the upper side just downstream of the first primary vortex. Finally a third Kármán vortex with the same rotation sign as the first one is visible downstream at the bottom of the measurement volume. Even in this relatively thin view of the cylinder wake a significant three-dimensional behavior can be observed with a secondary roller interconnecting the second and the third vortex oriented approximately at 45 degrees and exhibiting a vorticity level comparable with the primary rollers. At the present Reynolds number the shear layers separating from the cylinder are transitional and three-dimensionality on the scale of the Kármán vortices is expected (Williamson 1996).

The iso-surfaces of vorticity stretching vector magnitude ($|\overline{\omega \cdot \nabla V}|$, figure 5.14-right) show that the stretching activity is concentrated in the core of the secondary roller and indicates that these structures are responsible for the increase and re-orientation of the vorticity between the main rollers.

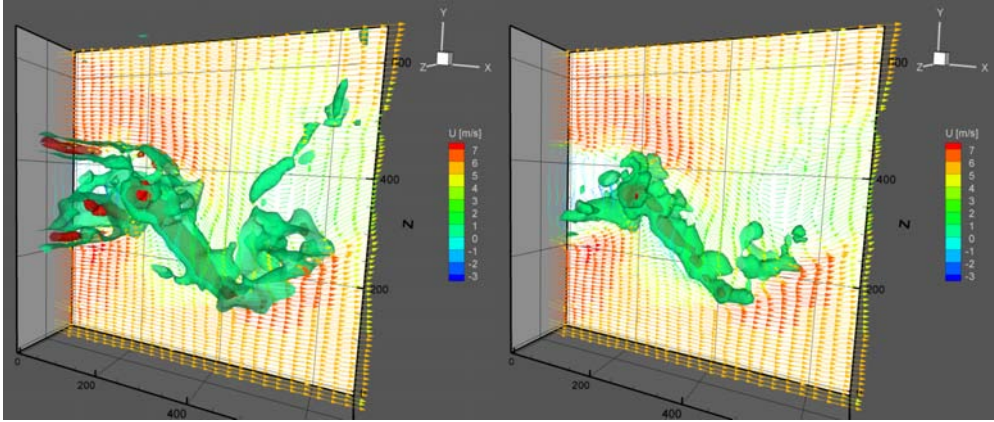


Figure 5.14: Instantaneous flow field snapshot. Left: vorticity vector magnitude iso-surfaces ($|\omega| = 2 \times 10^3 \text{ s}^{-1}$, green; $|\omega| = 4 \times 10^3 \text{ s}^{-1}$, red) and velocity vectors in the mid section of the measurement volume. Vectors color-code the streamwise velocity component. Right: vorticity stretching vector magnitude iso-surfaces ($|\vec{\omega} \cdot \nabla \vec{V}| = 5 \times 10^6 \text{ s}^{-2}$, green; $|\vec{\omega} \cdot \nabla \vec{V}| = 15 \times 10^6 \text{ s}^{-2}$, red).

To improve the visualization of the structural organization of the flow the spanwise and the combination of streamwise and y component of vorticity are color-coded as shown in figure 5.15. The four uncorrelated snapshots show consecutive phases of the vortex shedding cycle. The transition from snapshot (a) to (b) marks the separation of a Kármán vortex from the upper shear layer with stretching of the secondary vortex between this Kármán vortex and the new vortex forming from the lower shear layer. This observation is consistent with the large value for the vorticity stretching magnitude at this location in figure 5.14-right, which is computed from snapshot (a). The snapshots (c) and (d) show further stretching and curling of the secondary vortices around the Kármán vortex as it is convected to $x/D = 4.2$ and 4.4 respectively. Moreover the normalized vorticity level in the Kármán vortices $\omega_z D / u_\infty = 2.2$ agrees closely with planar PIV measurements in Reynolds number range 2,000 to 10,000 from Huang et al (2006), who report an average normalized peak vorticity of 2.1 at $x/D = 3$.

The spanwise organization of the flow structure becomes more visible from the vertical cylinder experiments (figure 5.16). The secondary vortex structures (blue and red depending on the orientation of vorticity in stream wise direction) appear to be organized in counter rotating pairs yielding a quasi periodic behavior. From a visual inspection of 100 snapshots the normalized spatial wave length λ_z / D is estimated at 1.2 (Scarano et al 2006), which is in good agreement with Huang et al (2006) and slightly in excess with the reported values at lower Reynolds number (Williamson 1996). The effect of the secondary structures is to first distort the primary Kármán vortices, as clearly seen in figure 5.16-bottom at $x/D = 4.5$, and finally cause breakup of the primary vortices.

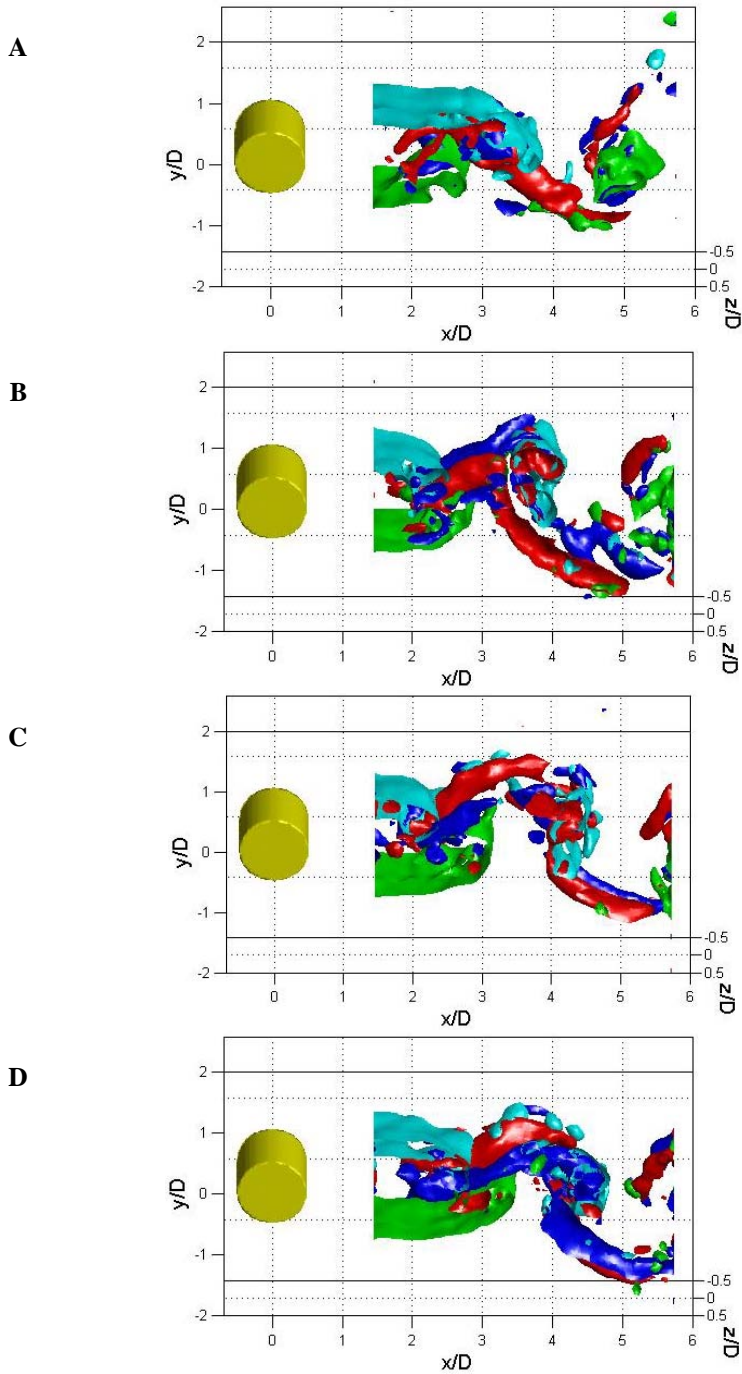


Figure 5.15: Instantaneous vorticity iso-surfaces showing four consecutive phases of the vortex shedding cycle ($\omega = 1.4 \cdot 10^3 \text{ s}^{-1}$). Color coding: cyan $\omega_z < 0$; green $\omega_z > 0$; blue $\sqrt{\omega_x^2 + \omega_y^2} \cdot \text{sign}(\omega_x) < 0$; red $\sqrt{\omega_x^2 + \omega_y^2} \cdot \text{sign}(\omega_x) > 0$.

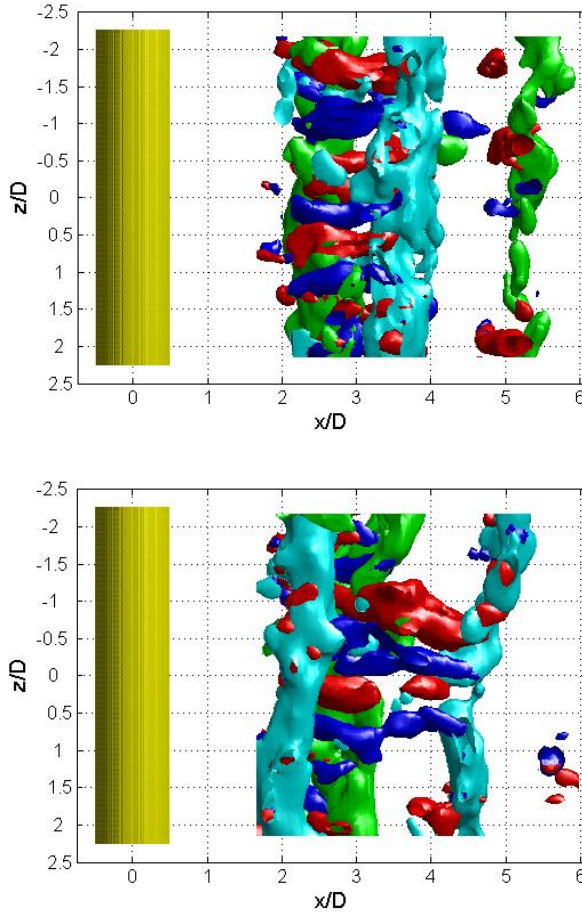


Figure 5.16: Instantaneous vorticity iso-surfaces from vertical cylinder experiments. Color coding as in figure 5.15.

The returned spatial organization of the flow and vorticity level compare well with what is reported in literature, as shown above, so that the current results demonstrate that the instantaneous structures in the flow can be captured in a 3D volume with Tomographic-PIV. Moreover the returned flow velocity exhibits a large variation along the viewing directions of the cameras, which allows concluding that independent velocity information is measured along the z -coordinate corresponding with the volume depth. Possible noise or reconstruction artifacts, when present, are in fact expected to propagate particle (displacement) information along viewing lines ultimately resulting in a quasi uniform particle displacement along that line. Clearly such effects do not play a dominant role in the current experiment.

5.7

Conclusions

The accuracy of Tomographic-PIV was assessed experimentally based on measurements of a circular cylinder wake flow at $Re_D = 2700$, which were carried out for a light sheet thickness of 2, 4, 8 and 12 mm and seeding density ranging from 0.01 to 0.1 *ppp*. Both the accuracy of the 3D particle reconstruction and velocity measurement were considered. The experimental setup consisted of a four camera imaging system with a maximum angle between viewing directions of 45 degrees and a slit to set the light sheet thickness and to sharply define its position in depth.

A procedure was described to quantify reconstruction noise (in the form of ghost particles) in Tomographic-PIV experiments, which applied to the present measurements returned the reconstruction signal-to-noise ratio as a function of light sheet thickness and seeding density (figure 5.7). The results confirmed the trends predicted by the model for ghost particle formation presented in section 4.1, so that in future experiments the reconstruction accuracy can be estimated a priori.

The accuracy of the measured velocity is assessed by a comparison of the velocity statistics within the 8 mm thick volume with planar Stereoscopic-PIV. It was shown that the mean and RMS velocity agree within 0.5 and 0.3 m/s respectively (corresponding to 0.30 and 0.18 voxel particle displacement). Moreover, for the range of particle image seeding densities considered (0.02 to 0.08 *ppp*) no significant difference in the returned velocity and vorticity statistics was observed, even though the number of ghost particles exceeded the number of actual particle for 0.08 *ppp*. Furthermore it was found that reconstruction noise or ghost particles have a limited effect on the cross-correlation resulting in a high and approximately constant signal-to-noise ratio.

The instantaneous velocity fields returned the Kármán street with counter-rotating vortices alternatively shed and cross-linked by secondary vortex structures aligned in the streamwise-binormal direction. Both the flow organization and the vorticity level were in good agreement with literature. The results give a further confirmation that the Tomographic-PIV technique is suited to the study of complex three-dimensional flows.

Chapter 6

Challenges in the application of PIV to supersonic flows

In chapter 10 of this thesis, the implementation of PIV into a supersonic wind tunnel environment will be treated. This environment poses a series of specific challenges, many of which are rather technical in nature such as: limited optical access for illumination and image recording, the required high seeding rates and the vibrations of the wind tunnel and consequently measurement setup. Careful design of the experimental apparatus can solve or alleviate these aspects. However, there are also intrinsic limitations associated to PIV in supersonic flows, most notably particle lag and image distortion due to the refractive index field, which will be briefly discussed below. As will be shown, both these effects may introduce bias errors in the measured velocity distribution, which can result in misinterpretation of the flow field if not properly understood.

6.1

Particle lag

The density of the tracer particles used for PIV in air is usually much larger than the gas density. Therefore, inertial forces acting on the particle cause a lag of the particle motion with respect to the flow, also known as particle slip. This lag is especially important in high speed flows, because of the large flow acceleration or short time scales that are likely to occur under these conditions. One can think of shock waves in the extreme case.

Particle lag can be evaluated by considering the equation for particle motion, which for tracer particles in air can be simplified to (Melling 1997):

$$\frac{\partial \mathbf{V}_p}{\partial t} = \frac{\mathbf{V} - \mathbf{V}_p}{\tau_p} \quad (6.1)$$

where \mathbf{V}_p and \mathbf{V} are the particle and local flow velocity respectively, and τ_p is a characteristic time scale referred to as the particle relaxation time. For spherical particles τ_p can be estimated assuming low particle slip velocities and using a modified Stokes drag (Melling 1997), which yields:

$$\tau_p = \frac{\rho_p d_p^2}{18\mu} (1 + 2.7Kn_p) \quad (6.2)$$

where ρ_p is the particle density, d_p is the particle diameter, μ is the fluid dynamic viscosity and Kn_p is the Knudsen number based on the particle diameter. For the $d_p = 1 \mu\text{m}$ water droplets used in the low speed PIV experiments in the present thesis ($Kn_p = 0$, chapters

5 and 8), it can be verified that τ_p is approximately $4 \mu\text{s}$, which is small compared to the relevant time scale in the flow and the light pulse separation applied in these experiments (i.e. the measured particle displacement is their motion integrated over the pulse separation time, which is $35 \mu\text{s}$ and $100 \mu\text{s}$ in the experiments of chapter 5 and 8 respectively). Therefore, particle lag is relatively unimportant in these conditions. However, in high speed and supersonic flows, particle lag can become of the same order as the light pulse separation (e.g. $2 \mu\text{s}$ in chapter 10), and hence must be considered.

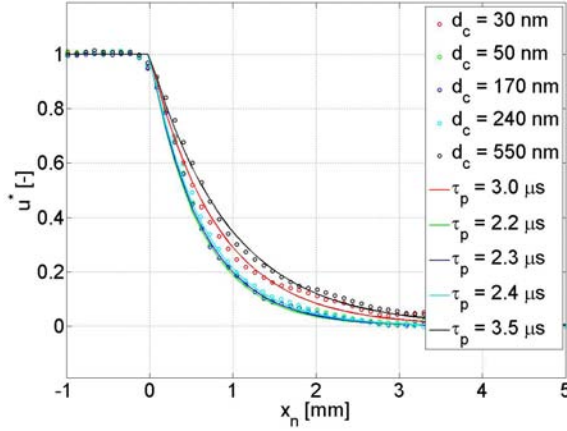


Figure 6.1: Measured velocity profiles (circles) with fits (solid lines) for different particle crystal sizes (Schrijer and Scarano 2007).

In the present (chapter 10) and many other supersonic PIV experiments at Delft University of Technology (e.g. Scarano and Van Oudheusden 2003, Schrijer et al. 2006, Humble et al. 2007), solid titanium dioxide (TiO_2) tracer particles are used. Schrijer and Scarano (2007) have evaluated the particle relaxation τ_p of the TiO_2 particles of various crystal sizes experimentally by measuring the particle response to a steady shock wave with planar PIV. The shock in this case can be viewed as a step input to the particle equation of motion (Eq. 6.1), which can then be solved analytically assuming τ_p constant yielding (Schrijer and Scarano 2007):

$$u^* = \frac{u_{np} - u_{n2}}{u_{n1} - u_{n2}} = \exp\left(\frac{-t}{\tau_p}\right) \approx \exp\left(\frac{-x_n}{\tau_p [u_{n1} - (u_{n2} - u_{n1}) \exp(-1)]}\right) \quad (6.3)$$

where u_n is the velocity component to the shock, the subscript p denotes the measured particle velocity and the subscripts 1 and 2 denote the fluid flow conditions before and after the shock respectively. Because PIV returns spatial information, the time response is rewritten to a spatial relaxation profile, where x_n is the distance normal to the shock. By fitting the analytical expression (Eq. 6.3) to the measured profiles, the particle relaxation time is obtained. The results for the different tested particle crystal sizes d_c are presented in figure 6.1. The fits return a nearly constant τ_p for the crystal sizes between 50 and 240 nm of

approximately $2.3 \mu\text{s}$ corresponding to a characteristic particle response frequency of 430 kHz. For the smallest (30 nm) and largest crystal sizes (550 nm) larger values for τ_p are found. These results clearly do not follow the predicted relation between particle size and τ_p (Eq. 6.2), which must be attributed to particle agglomeration. Moreover, the 240 nm particle seems to yield an optimum between small particle size for relatively low particle lag and large size to yield large particle image intensity.

6.2 Refractive index effects

The presence of variations in density, hence refractive index, in supersonic flow distorts the imaging process by deflecting light rays propagating through the flow. The principles of light ray deflection in a refractive index field are well understood and are in fact exploited in flow visualization techniques such as shadowgraphy, conventional schlieren and background oriented schlieren (BOS), see for example Settles (2001) and Elsinga et al. (2004). Although beneficial to the mentioned visualization techniques, in PIV these refractive index effects, also known as aero-optical distortion effects, introduce errors in the measured velocity as described by Elsinga et al. (2005).

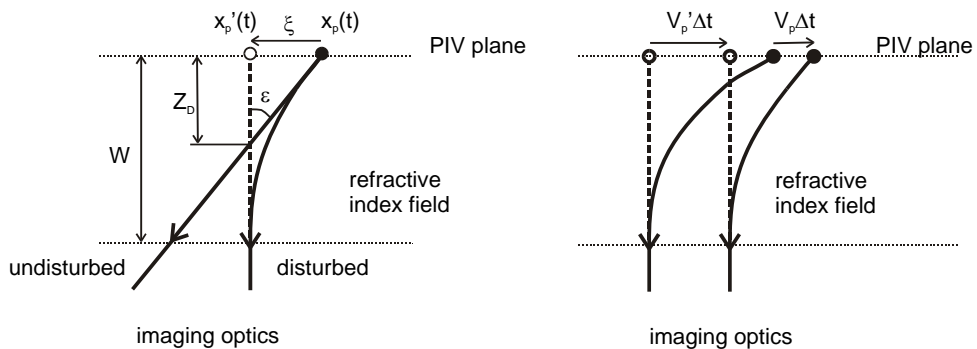


Figure 6.2: Optical distortion in PIV due to a refractive index field extending over a distance W from the measurement plane: position error (left) and direct velocity error (right). Solid lines represent light ray trajectories coming from the particle (solid circle). Dashed lines are the backward extension of those rays indicating the position where the particle is perceived in the PIV plane (open circles). (Elsinga et al. 2005)

The model for aero-optical distortion in planar PIV is based on geometrical optics and is shown in figure 6.2. For simplicity only a single light ray for each particle is considered, but this is not essential for the description of the optical errors. Figure 6.2-left shows an undisturbed light ray propagating through a homogeneous refractive index field and the disturbed one (through an inhomogeneous refractive index field) coming from a single particle and initially propagating in the same direction. A backward extension of the two light rays (dashed line) reveals that for the disturbed light ray, the position of the particle as perceived by the imaging optics (open circle) is different from the actual position of the particle in the PIV plane (solid circle). This spatial displacement is referred to as the position

error. Figure 6.2-right shows a single particle (moving to the right) at two subsequent exposures separated by a time interval Δt . The position error at the two spatial locations may differ returning different position errors for the two particle images. This results in an error in the perceived particle image particle displacement, hence measured particle velocity. This is referred to as the direct velocity error.

Mathematically the image distortion can be expressed in terms of an optical displacement vector $\xi(\mathbf{x})$, as:

$$\xi(\mathbf{x}_p(t)) = \mathbf{x}_p'(t) - \mathbf{x}_p(t) \quad (6.4)$$

where $\mathbf{x}_p(t)$ is the actual particle location (x,y) in the measurement plane and $\mathbf{x}_p'(t)$ is the location where that particle is perceived by the imaging system (figure 6.2-left). The optical displacement vector is directly equivalent to the position error of the measurement and is related to the gradient of the refractive index ∇n . BOS studies (Richard and Raffel 2001, Elsinga et al. 2004) propose the following expression for the optical displacement vector based on the theory of light propagation in a refractive index field (using $n \approx 1$):

$$\xi(\mathbf{x}) = -Z_D \boldsymbol{\varepsilon}(\mathbf{x}) = -Z_D \int_S \nabla n(\mathbf{x}, z) dz \quad (6.5)$$

where z is the coordinate direction normal to the PIV measurement plane, $\boldsymbol{\varepsilon}$ is the light beam deflection angle and Z_D is the distance parallel to the optical axis between the measurement plane and the intersection point of the disturbed ($\nabla n \neq 0$) and undisturbed ($\nabla n = 0$) light rays coming from the same particle (figure 6.2-left). The refractive index n depends on the density ρ according to the Gladstone-Dale relation, i.e. $n = 1 + K\rho$ ($K = 2.3 \cdot 10^{-4} \text{ m}^3/\text{kg}$ for air).

The velocity error of the measurement $\Delta \mathbf{V}_p$ is now defined as the difference between the measured velocity and the actual particle velocity \mathbf{V}_p at a given location \mathbf{x} in the image, which is given by (Elsinga et al. 2005):

$$\Delta \mathbf{V}_p(\mathbf{x}) = \frac{d\xi(\mathbf{x}(t))}{dt} - \frac{\partial \mathbf{V}_p}{\partial \mathbf{x}} \xi(\mathbf{x}) = (\nabla \xi) \mathbf{V}_p - (\nabla \mathbf{V}_p) \xi \quad (6.6)$$

The first term on the right hand side is the direct velocity error (figure 6.2-right) which is given by the product of the actual particle velocity and the gradient of the optical displacement vector. The latter represents a local change in optical magnification, which “stretches” the imaged object with respect to the physical dimension in the measurement plane. Note that only the derivative of the optical displacement vector taken in the direction of the velocity vector contributes to the error. The second term in Eq. 6.6 is the product of the optical displacement vector with the gradient of the actual particle velocity and represents the contribution of the position error (figure 6.2-left) to the velocity error. It was shown previously that the optical displacement vector is related to the gradient of refractive index (Eq. 6.5).

Elsinga et al. (2005) have shown by numerical simulations and experiment that the direct velocity error term (the first term on the right hand side in Eq. 6.6) dominates and can introduce significant errors most notably in expansions and compressions. Moreover, PIV measurements of the velocity distribution over shock waves (Elsinga et al. 2005b) have shown that particle image blur indicates the presence of a significant velocity error related to

aero-optical distortion. This can be understood from the mechanism of particle image blur (figure 6.3). The scattered light from a particle is captured by the imaging optics through a finite solid angle of semi-aperture θ . When changes in the amount of deflection occur within the mentioned angle (due to a local variation in the gradient of refractive index), the imaging system becomes astigmatic producing a blurred particle image, where the blur length ξ_{blur} is given by:

$$\xi_{blur} = \xi_1 - \xi_2 \sim (\nabla \xi) dx \quad (6.7)$$

The blur is anisotropic with the largest blurring directed along a principal axis of $\nabla \xi$. From Eq. 6.6 and 6.7 it is seen that both the direct velocity and particle image blur are related to the gradient of the optical displacement vector $\nabla \xi$, although there is no direct relation between the two optical distortion effects. Therefore, blur can indicate the presence of the direct velocity error, but cannot be used directly to correct for it.

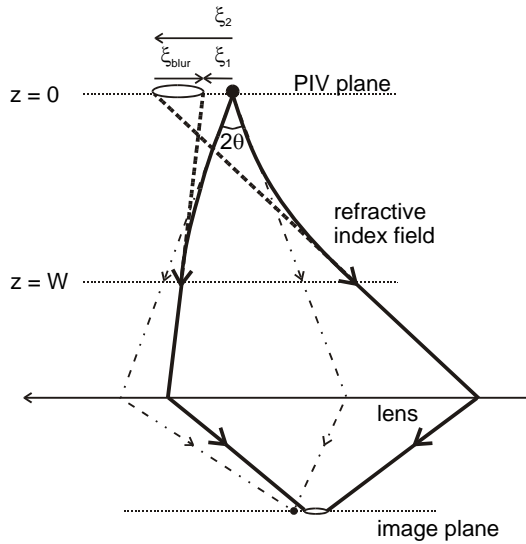


Figure 6.3: Principle of refractive particle image blur. Solid lines represent light ray trajectories coming from the particle (solid circle) edges in an inhomogeneous refractive index field. Dashed lines are the backward extension of those rays indicating the edges where the particle appears in the PIV recordings (open ellipse). (Elsinga et al. 2005)

As mentioned above aero-optical distortion effects are most profound in PIV measurements of (concentrated) expansions, compressions and, notably, shock waves. An example of the latter is presented in figures 6.4 and 6.5. The measured velocity distribution (figure 6.4) displays an unphysical acceleration of the flow in front of the shock due the refractive index variation over the shock, which increases the measured local flow velocity by approximately 4% inside the square labeled B, i.e. u increases locally from 16.3 pixels displacement in the uniform flow region in front of the shock to 17.0 pixels near the shock. In the uniform flow region (labeled A) the refractive index is also uniform, therefore the

light scattered by the tracer particles is transmitted without distortion. When comparing the recorded particle images in both regions (figure 6.5), it is seen in the uniform flow region (A) the particle images are circular without blur while at location (B), representing the shock wave, the particle image is blurred in the direction normal to the shock as expected due to the local variation of the refractive index. Moreover, the particle peak brightness has decreased as a result of blur.

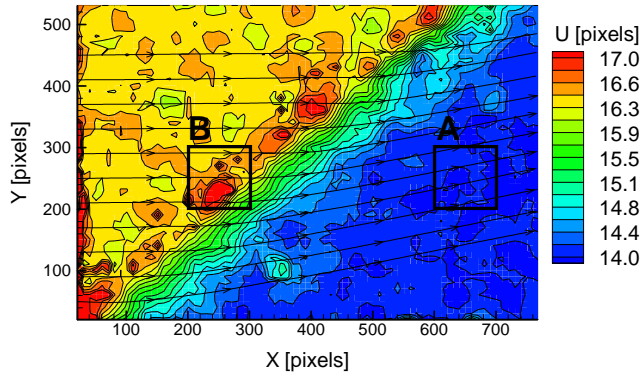


Figure 6.4: The u -component of velocity in pixel units with streamlines from an instantaneous PIV measurement of a 2D oblique shock wave at Mach 2. (Elsinga et al. 2005)

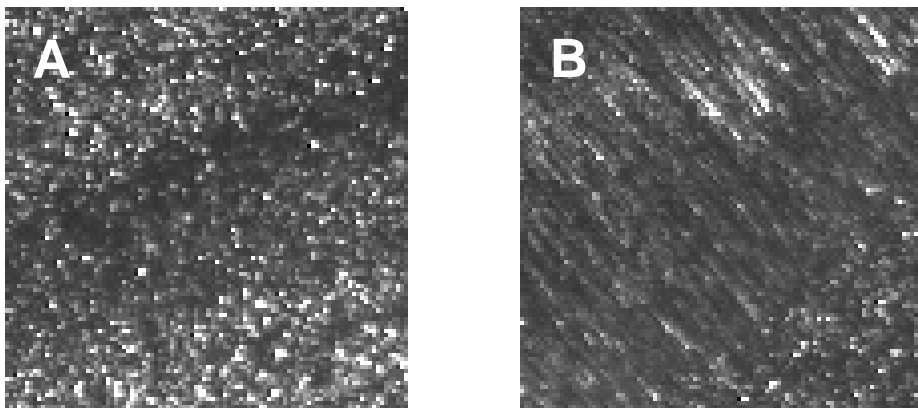


Figure 6.5: Detail (100x100 pixels) of the PIV recording corresponding to the velocity field of figure 6.4 at positions A (left) and B (right). (Elsinga et al. 2005)

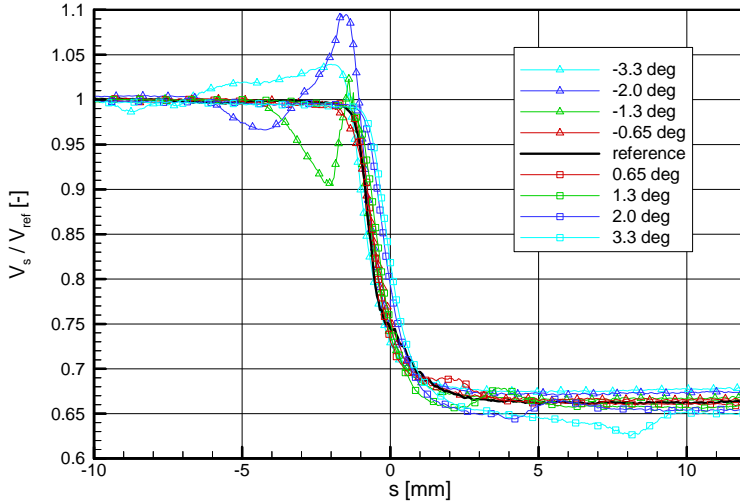


Figure 6.6: The effect of the viewing direction on the average normalized velocity profiles across a shock wave taken in the direction normal to the shock s . The angle between the shock plane and the camera viewing direction is given in the legend, where a positive angle is defined as viewing through the shock from the low density side. (Elsinga et al. 2005b)

Figure 6.6 presents measured velocity profiles across a shock for various measurement configurations, i.e. varying the viewing direction w.r.t. the shock plane. The black reference line shows the velocity profile without significant errors related to refractive index effects. The other profiles are affected by optical distortion and show the sensitivity of the velocity error on the measurement setup. Furthermore they indicate typical values for the magnitude of the error, which can be as large as 10% of the velocity in the direction normal to the shock. For further detail is referred to Elsinga et al. (2005b).

For Tomographic-PIV aero-optical distortion affects the 3D particle reconstruction in a similar manner as calibration errors in the sense that lines of sight are dislocated. Therefore, the numerical assessment of the tomographic reconstruction quality in the presence of calibration errors (figure 4.6-F) can be used to evaluate distortion effects substituting the calibration error by the aero-optical dislocation. Where the latter is calculated using the distortion theory outlined above.

Finally, solution strategies to the problem of aero-optical distortion effect include the reduction of the integration length through refractive index field by positioning the measurement location close to the tunnel window, thereby reducing the optical displacement vector $\xi(\mathbf{x})$ and its gradient. Furthermore, the viewing direction can be chosen such as to minimize the deflection angle, i.e. reduce the angle between the refractive index gradient and the viewing direction. Both approaches have been followed in the supersonic wind tunnel experiments to be presented in chapter 10. As a result no aero-optical distortion effects have been observed.

Part II

Experimental investigation of turbulent boundary layers

Chapter 7

Coherent structures in the turbulent boundary layer

This chapter provides a comprehensive framework for discussion of the Tomographic-PIV turbulent boundary layer measurement results to be presented in following chapters. The nomenclature and notations are introduced, followed by a short overview of the relevant coherent structures in literature considering both subsonic and supersonic turbulent boundary layers. Finally the coherent structures visualization methods applied in the present studies are presented together with a method for obtaining conditionally averaged structures.

7.1

Terminology

The results will be presented in a right-handed coordinate system, where the x, y and z -axis are chosen as the free-stream flow direction, wall-normal direction with $y = 0$ at the wall and the spanwise direction respectively (see also figure 7.2-right). The corresponding components of the velocity vector \mathbf{V} are u, v and w .

In the context of the turbulent boundary layer, the coordinates and velocity can be made dimensionless using either the so-called inner or outer scaling. The former is also referred to as wall or plus units and normalizes the spatial coordinate \mathbf{x} and velocity \mathbf{V} with viscous length and velocity scales to give:

$$\mathbf{x}^+ = \frac{\mathbf{x}u_\tau}{\nu} \quad ; \quad \mathbf{V}^+ = \frac{\mathbf{V}}{u_\tau} \quad (7.1)$$

where ν is the kinematic viscosity and u_τ is the skin friction velocity, which for incompressible flow is defined as:

$$u_\tau = \sqrt{\frac{\tau_w}{\rho}} \quad \text{with} \quad \tau_w = \mu \left(\frac{\partial u}{\partial y} \right)_w \quad (7.2)$$

In eq. 7.2 μ is the dynamic viscosity, ρ is the density and the subscript w denotes the conditions at the wall ($y = 0$). Alternatively outer scaling uses the boundary layer thickness δ and the free stream velocity U_e to normalize \mathbf{x} and \mathbf{V} . In this thesis the boundary layer thickness is defined as the distance from the wall where the average velocity attains 99% of the free stream value δ_{99} .

Following the Reynolds decomposition, the instantaneous velocity in a turbulent flow is expressed as the sum of a mean $\bar{\mathbf{V}}$ and a fluctuating component \mathbf{V}' , which is written as:

$$\mathbf{V}(\mathbf{x}) = \bar{\mathbf{V}}(\mathbf{x}) + \mathbf{V}'(\mathbf{x}) \quad (7.3)$$

where in the present study the mean is the average of the ensemble of N (PIV) instantaneous velocity snapshots \mathbf{V}_i , which is written as:

$$\bar{\mathbf{V}}(\mathbf{x}) = \frac{1}{N} \sum_{i=1}^N \mathbf{V}_i(\mathbf{x}) \quad (7.4)$$

The local flow can be further characterized by considering the fluctuating velocity in the u', v' plane, which is known as quadrant decomposition (Willmarth and Lu 1972), see figure 7.1. More specifically, ejection and sweep motions are defined as fluctuations in the second (Q2) and fourth quadrant (Q4) of this plane respectively. Ejections can be interpreted as the transport of low speed fluid ($u' < 0$) away from the wall ($v' > 0$), whereas sweeps are transport of high speed fluid ($u' > 0$) towards the wall ($v' < 0$). In this thesis low and high speed are to be understood as relative to the local average velocity. As will be shown in chapter 8, the velocity fluctuations in a turbulent boundary layer are biased towards Q2 and Q4 resulting in a non-zero (negative) Reynolds shear stress $\overline{u'v'}$, which is defined as:

$$\overline{u'v'}(\mathbf{x}) = \frac{1}{N} \sum_{i=1}^N u'_i(\mathbf{x})v'_i(\mathbf{x}) \quad (7.5)$$

The Reynolds shear stress is a measure for turbulent diffusion in the boundary layer and is an important term in the turbulent boundary layer equation for incompressible zero-pressure gradient flow (White 1991).

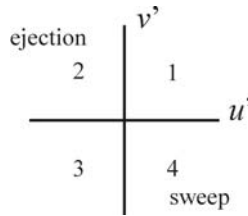


Figure 7.1. Quadrants of the instantaneous u', v' plane.

As the spatial flow variation in the wall-normal direction is concerned, the turbulent boundary layer can be divided into an inner region ($y^+ \leq 100$) containing the viscous sub-layer, the buffer layer and part of the logarithmic layer, and an outer region ($y^+ > 100$) containing the upper part of the log-layer and the wake region. The wake region starts where the average velocity profile departs the logarithmic, usually around $y/\delta = 0.1$. The division into inner and outer layer is motivated by the physical notion that near the wall (inner layer) viscous shear dominates over turbulent shear, whereas the opposite is the case in the outer layer. More elaborate discussions of these layers and mean velocity profiles can be found in White (1991) and George (2006). Concerning the instantaneous flow origination, it should be noted that different coherent structures have been observed within the inner and outer region (see also figure 7.2).

To be able to discuss coherent structures and identify them later on in the measured velocity fields by PIV, a definition is required. In this thesis the approach of Robinson

(1991) is followed, who states that *a coherent motion is a three-dimensional region of the flow over which at least one fundamental flow variable (velocity component, density, temperature, etc.) exhibits significant correlation with itself or with another variable over a range of space and/or time that is significantly larger than the smallest local scales of the flow.* Others have used more restrictive definitions, such as Hussain (1986) who defines them in terms of phase-correlated vorticity and vortices. Even though vortices constitute a very important class of coherent structures, as seen in the following section, the more general definition is preferred here, because it also allows the observed large zones of uniform low and high momentum flow to be considered a coherent motion. Furthermore, the term coherent structure will be used interchangeably with coherent motion and eddy structure.

A universally accepted definition of a vortex does not exist, but a useful working definition is that *a vortex exists when instantaneous streamlines mapped onto a plane normal to the vortex core exhibit a roughly circular or spiral pattern, when viewed from a reference frame moving with the center of the vortex core* (Robinson 1991). Like other definitions, this statement contains a notion of fluid locally rotating around a common center. A translation of this definition into a practical detection method (i.e. mathematical quantity that can be used for data visualization) will be discussed in section 7.4. Finally, the terms steamwise, wall-normal and spanwise in conjunction with vortices refer to the principal orientation of the axis of rotation, which is normal to the plane of rotation.

7.2

Structural elements in the outer layer

The concept of coherent structures seeks to describe the turbulent flow in terms of elementary flow structures. It aims at reducing the complexities of turbulence in order to improve the understanding of the kinematics and dynamics of turbulence. Those concepts can be further used to construct representative flow models, as will be shown later. Moreover understanding the structure and dynamics of the flow may guide future attempts to flow control and drag reduction in case of turbulent boundary layers. Reviews of the coherent structures observed in turbulent boundary layers have been provided by Cantwell (1981), Robinson (1991) and Adrian (2007), which will not be repeated here. Rather a short summary of the structures that occur in the outer layer is given to aid the discussion of the experimental results in subsequent chapters. As the coherent structures in turbulent channel flow and boundary layer flow are believed to be very similar, examples from both cases will be used to support the discussion.

7.2.1

Overview

Perhaps the simplest coherent structures are based on the local fluctuating velocity vector. They include the sweep and ejection events introduced in the previous section (figure 7.1), which have a special significance to the Reynolds shear stress. Other velocity based structures are the low and high speed zones (relative to the average velocity) in the outer layer, which should not be confused with the well-known near-wall streaks with a mean spanwise spacing of 100 viscous wall units ν/u_τ . The low speed zones have been reported to extend over large distances in streamwise direction, as will be shown later. Furthermore the zones of low and high speed are often separated in space by thin regions of high fluctuating vorticity that may be considered as shear layers.

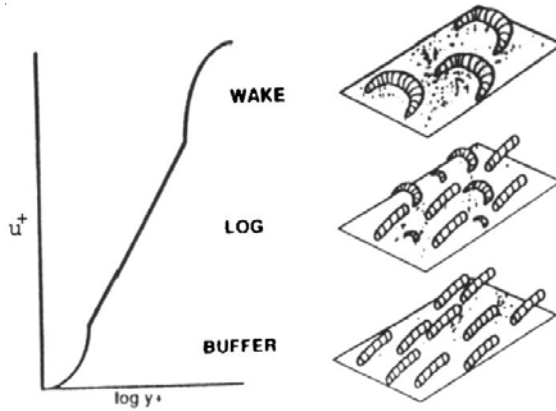


Figure 7.2. Schematic of the vortex structures in the different regions of the turbulent boundary layer. (Robinson 1991)

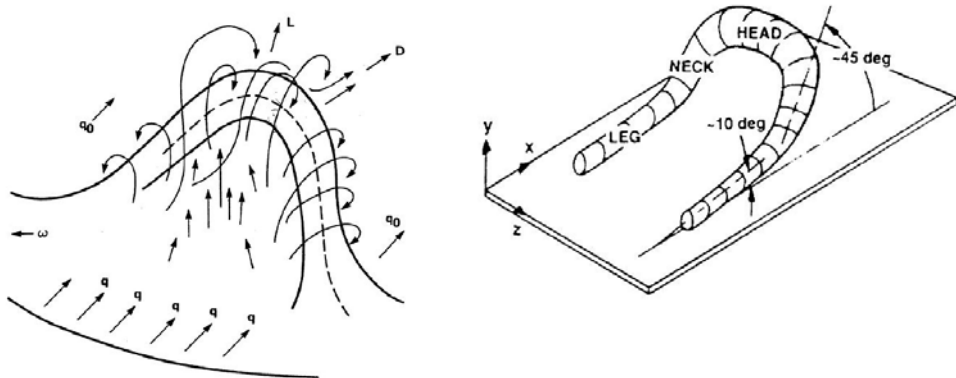


Figure 7.3. Horseshoe vortex model (left, Theodorsen 1952) and nomenclature (right, Robinson 1991b).

The second, more complex class of coherent structure is the vortex of various forms. Quasi-streamwise vortices have been observed mostly in the near wall region, while the wake region is mostly populated by hairpin or arch vortices (figure 7.2, Robinson 1991 and references therein). It should be noted that in this thesis the term hairpin will be used to denote arch, horseshoe, hairpin and cane vortices following Adrian et al. (2000), because they are believed to be variations of the same basic structure. The hairpin vortex structure was introduced by Theodorsen (1952) as a horseshoe shaped structure around which the local fluctuating flow exhibits a swirling motion (figure 7.3). The different parts of this structure have been named legs, necks and head (figure 7.3-right), where the first refers to the quasi-streamwise vortices near the wall and the latter is the part furthest from the wall having the principal swirling component in the negative spanwise (z -) direction. The head is connected on both sides to the legs through the necks, which typically are inclined at 45 degrees with the wall. Associated to the hairpin structure are the ejection event upstream, underneath the head in between legs, the low speed flow underneath the head and the sweep

events outboard of the hairpin necks. Furthermore hairpins have often been observed to be asymmetric, or one legged (cane type), in DNS data of a turbulent boundary layer (Robinson 1991) and LES data of a turbulent channel flow (Moin and Kim 1985).

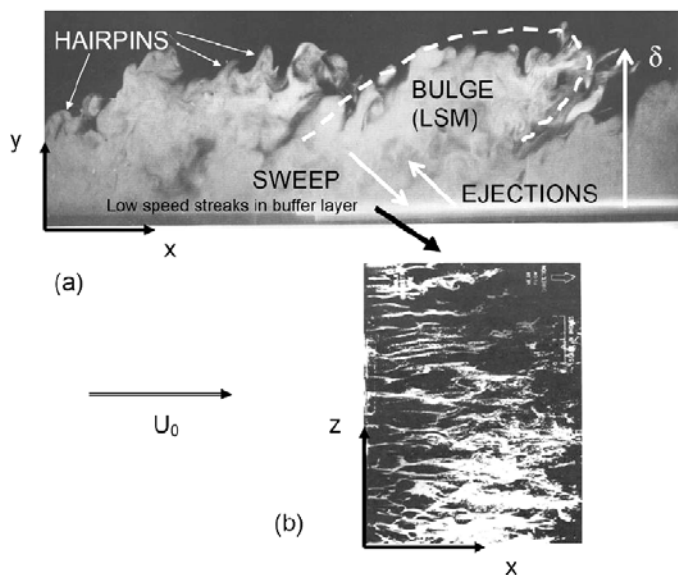


Figure 7.4. Smoke visualization of the streamwise wall-normal plane in a turbulent boundary layer showing signatures of hairpin vortices in a turbulent bulge (top, Adrian 2007 from Falco 1977, $Re_\theta = 4000$) and H_2 bubble visualization of the near wall low speed streaks in a plane parallel to the wall (bottom, from Kline et al. 1967).

Experimental evidence for the existence of hairpin vortices exists mainly from planar (smoke) visualizations (figure 7.4) and PIV (figure 7.5) and to a lesser extent from conditionally averaged flow fields obtained by hot-wire anemometry. The smoke visualization of Falco (1977) (figure 7.4-top) shows the signature of hairpin heads indicated by the arrows, which he refers to as typical eddies. Moreover, the hairpins appear to be grouped in what is called a bulge or large-scale-motion (LSM). The spatial extent of LSM's is of the order of the boundary layer thickness. Head and Bandyopadhyay (1981), based on flow visualizations of turbulent boundary layers at Reynolds numbers based on momentum thickness Re_θ up to 17,500, conclude that hairpins within these bulges travel at approximately the same velocity. They also found that the heads of the hairpins within a bulge form an interface typical having an inclination of 20 degrees with the wall.

An example of the instantaneous velocity distribution in the streamwise wall-normal plane as returned by PIV is presented in figure 7.5 (taken from Adrian et al. 2000). In the velocity field zones of relatively uniform velocity, denoted I, II and III, are observed with high shear at the interfaces indicated by the solid lines (Meinhart and Adrian 1995). Along the interface separating zone I and II several hairpin signatures are observed, which heads are indicated by circles. In this plane, the hairpin signature is composed of a swirling motion

around the head relative to a convective velocity and an ejection event underneath and upstream of the head.

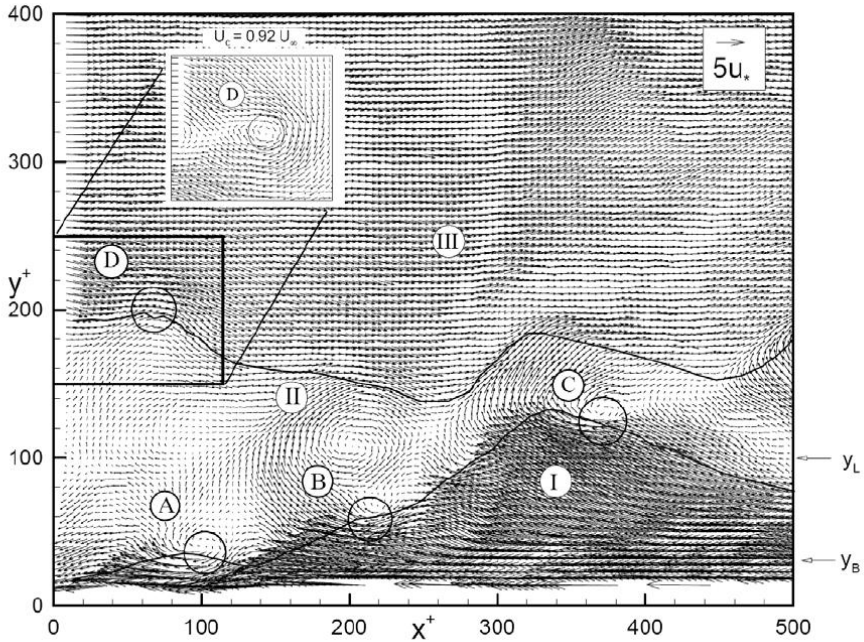


Figure 7.5. Instantaneous velocity distribution returned by PIV in the streamwise wall-normal plane showing hairpin head signatures (circles) separating zones of relatively uniform momentum (zones I, II and III indicated by the solid lines). A convective velocity of 80% of the freestream velocity is subtracted. $\delta^+ = 355$ and $Re_\theta = 930$ (Adrian et al. 2000)

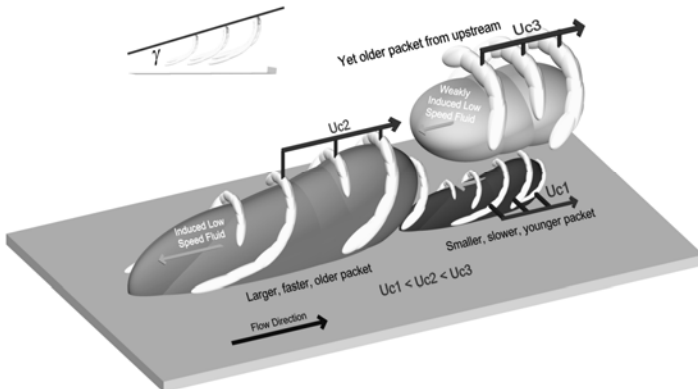


Figure 7.6. Conceptual sketch of the hairpin packets with older packets overlying newer packets. (Adrian et al. 2000)

Based on their PIV results Adrian et al. (2000) propose the organization of hairpins into packets, which are marked by a streamwise alignment of hairpin vortices convecting at the same velocity and inducing a single zone of uniform (low speed) flow between their legs. Therefore packets may be regarded as a coherent structure itself. A conceptual sketch of the hairpin packet model is presented in figure 7.6, where several packets are shown with a smaller and younger packet near the wall convecting at a relatively low velocity and older, faster convecting packets away from the wall. The wall-normal arrangement of packets moving over each other accounts for the stacked uniform momentum zones as observed in PIV results like figure 7.5. As a possible mechanism for packet formation, Zhou et al. (1999) suggest that new hairpins are generated upstream of a hairpin exceeding a threshold strength. This is known as the auto-generation mechanism and has been demonstrated by numerical simulations using a single hairpin as initial condition.

Power spectra obtained by hot-wire anemometry have indicated the presence of scales larger than the packets below $y/\delta = 0.2$ (order 10δ in streamwise direction), which are known as very-large-scale motions (Kim and Adrian 1999, Balakumar and Adrian 2007) or superstructures (Hutchins and Marusic 2007). In these measurements Taylor’s hypothesis of frozen turbulence is applied to convert the time signal from the hot-wire into length scales assuming the convection rate dominates over the rate of change associated to turbulent processes, which is written as:

$$\Delta x = \bar{u} \Delta t \tag{7.6}$$

Using a hot-wire rake Hutchins and Marusic (2007) have, furthermore, shown that the low speed zones meander and can be much longer (over 20δ , figure 7.7) in streamwise direction compared to what has been derived from single hot-wire measurements. Their width is approximately 0.4δ independent of Reynolds number. Moreover, they found that the very-large-scale structures leave an imprint on the flow in the near wall inner region. Toh and Itano (2005) describe the effect of the outer structure on the near wall streaks in their DNS channel flow data as the spanwise movement of the near-wall streaks towards the (very-) large-scale low speed zones under the influence of the large-scale spanwise flow. The spanwise movement is followed by merger and eruption of the near wall streaks underneath the low speed zones and generation of new near-wall structures underneath the high speed zones.

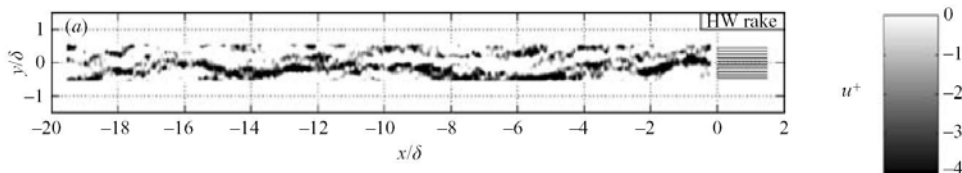


Figure 7.7. Hot-wire rake signal showing very-large-scale meandering low momentum zones (gray) in a $Re_\tau = 14,380$ turbulent boundary layer at 0.15δ distance from the wall. The x -axis is reconstructed using Taylor’s hypothesis. The y -axis corresponds to the spanwise direction in this figure. (Hutchins and Marusic 2007)

Kim and Adrian (1999) proposed a model for the very-large-scale motions based on observations of hairpin and packet signatures in hot-wire signals. In this model, shown in

figure 7.8, the very long low speed zones are created from multiple packets aligned in streamwise direction. The above models show a clear trend over the years towards larger scale structures and organization of the turbulent boundary layer flow. The hairpin still is a very relevant structural element but mainly as part of the much larger structures. This applies especially to the lower part of the boundary layer $y/\delta < 0.5$. It is interesting to note at this point, that the experimental results to be presented in chapter 10 seem to indicate that a very-large-scale flow organization may also exist not just in streamwise direction (i.e. the low speed zones) but also in spanwise direction, thus continuing the trend.

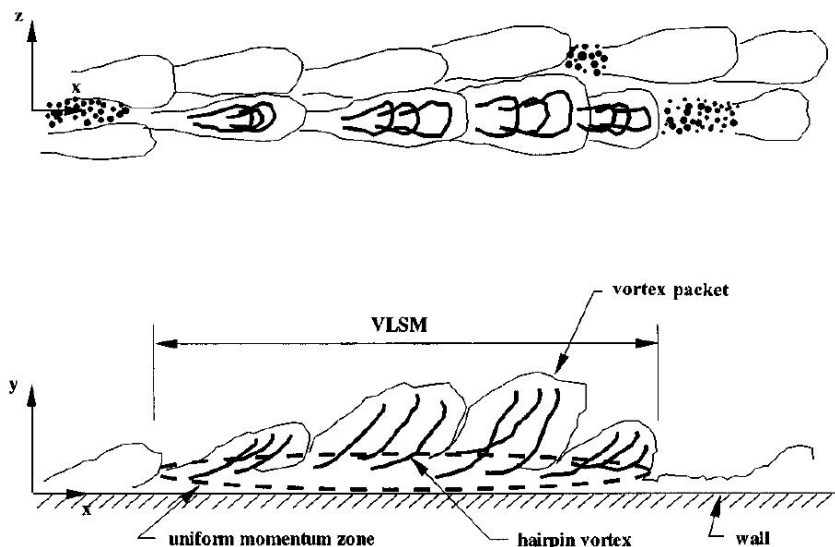


Figure 7.8. Model for very-large-scale motion (VLSM) where hairpins group in packets and packets align in streamwise direction to the very long zones of uniform low momentum (Kim and Adrian 1999).

7.2.2

Supersonic boundary layers

Concerning the physics of supersonic turbulent boundary layers and the coherent structure therein much less is known, as concluded by Spina et al. (1994). It is generally accepted that compressibility effects remain small for free stream Mach numbers M_e below 4, because the local fluctuating Mach number is small (< 0.3) throughout the boundary layer. Consequently the flow structure is often assumed to be similar to the incompressible case at equivalent Reynolds number. Experimental evidence in support of this assumption is provided by qualitative flow visualizations such as figure 7.9, which contains bulges and hairpin signatures similar to figure 7.4 for the subsonic boundary layer. Furthermore, PIV results obtained in a plane parallel to the wall (Ganapathisubramani et al. 2006) revealed very long low speed zones similar to the incompressible case.

DNS of compressible turbulent boundary layers is beginning to become available (Martin 2007), but is limited to Reynolds numbers much lower than in supersonic

experiments. However, the packets observed in Mach 3 DNS data have similar properties (i.e dimensions and number of hairpins) to those in the low Reynolds number incompressible experiments (Ringuette et al. 2007), which again shows that compressibility does not significantly affect the structures. Quantitative visualization of the 3D vortical structures at high Reynolds number is lacking, which provides an opportunity for Tomographic-PIV to contribute to this field (chapter 10).

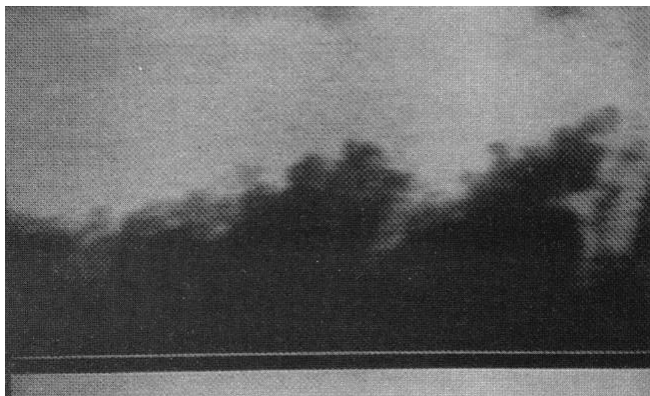


Figure 7.9. Visualization of the streamwise wall-normal plane in a supersonic turbulent boundary layer at $M_e = 2.5$ and $Re_\theta = 25,000$ obtained using Rayleigh scattering. The gray level is a measure for the local density. Compare with subsonic visualization of figure 7.4. (Smits 1991 after Smith 1989)

7.2.3

Turbulence modeling using coherent structures

To establish a link between the theory of coherent structures and the statistical approach to turbulence, Perry and Chong (1982) and Perry and Marusic (1995) have formulated a quantitative model of boundary layer turbulence based on Townsend's attached eddy hypothesis (Townsend 1976). They describe the kinematics of the turbulent boundary layer by an ensemble of eddies (hairpins), which are uncorrelated, randomly distributed in streamwise and spanwise direction and are attached to the wall in the sense that their size is proportional to the eddy's distance to the wall. However, the eddies do not necessarily extend all the way down to the wall, especially in the wake region. Furthermore, the population density of each hierarchy of hairpins scale and their vortex strength, are chosen such that the average velocity profile complies with the measured profile. This method has been successful in reproducing power spectra and Reynolds stresses showing that the (attached) hairpin models are feasible according to the turbulence statistics.

Later Marusic (2001) included hairpin packets in the quantitative model after experimental observations by Adrian et al. (2000), because single, statistically uncorrelated hairpins could not explain the long streamwise correlations observed in velocity measurements in the logarithmic layer, nor could long individual structures of different shapes. This study shows that packets are statistically relevant and also illustrates the interaction between experimental observations and quantitative modeling, and their complementary role.

7.3

Visualization of coherent structures

The flow structures of interest in this study are the low-speed zones (this terminology is used to distinguish from near-wall streaks) and the vortical structures, which often combine into hairpin packets. The former can be simply visualized in the velocity fields returned by Tomographic-PIV by iso-surfaces of the u -component of velocity selecting a level below the local average velocity. To detect and visualize vortical motion a number of criteria exist such as λ_2 (Jeong and Hussain 1995), λ_{ci} (Zhou et al. 1999), Δ (Chong et al. 1990) and Q (Hunt et al. 1988) all returning nearly equivalent visualizations (Chakraborty et al. 2005). Here the Q criterion is used, which will be presented next followed by a procedure to obtain averaged (vortex) structures.

7.3.1

Vortex detection

Vortical motion is visualized using the Q -criterion (Hunt et al. 1988), which is based on the analysis of the second invariant Q of the local velocity gradient tensor $\nabla\mathbf{V}$. For incompressible flow this criterion can be written as:

$$Q = \frac{1}{2} \left(|\boldsymbol{\Omega}|^2 - |\mathbf{S}|^2 \right) > 0 \quad (7.7)$$

where $\mathbf{S} = \frac{1}{2} \left(\nabla\mathbf{V} + (\nabla\mathbf{V})^T \right)$ is the rate-of-strain tensor and $\boldsymbol{\Omega} = \frac{1}{2} \left(\nabla\mathbf{V} - (\nabla\mathbf{V})^T \right)$ is the vorticity tensor. Hence Q is a measure of the excess rotation rate relative to strain rate and indicates a local swirling flow topology as shown by Chakraborty et al. (2005). This kinematic interpretation allows the incompressible formulation of Eq. 7.7 to be applied in case of compressible flow as well. Moreover, compressibility effects are expected not to be important for the present case anyway, as argued in section 7.2.2. A non-zero Q threshold is employed to separate the vortical structures from the measurement noise.

The velocity gradients in $\nabla\mathbf{V}$ are obtained from the measured velocity distribution by a second order polynomial regression. In this procedure the function:

$$f_{reg}(r_x, r_y, r_z) = a_0 + a_1 r_x + a_2 r_y + a_3 r_z + a_4 r_x r_y + a_5 r_x r_z + a_6 r_y r_z + a_7 r_x^2 + a_8 r_y^2 + a_9 r_z^2 \quad (7.8)$$

is fit in the least squares sense to each component of velocity in a $5 \times 5 \times 5$ neighborhood of a point x', y', z' . In Eq. 7.8 r_x, r_y, r_z are distances in x, y and z -direction w.r.t. x', y', z' and the coefficients a_i are fit variables with a_0 being the filtered velocity at x', y', z' and a_1, a_2, a_3 being the gradients in x, y and z respectively. Note that the $5 \times 5 \times 5$ kernel size is equal to the cross-correlation interrogation volume (when using 75% overlap), so that the spatial frequency response of cross-correlation and regression are similar. Consequently the regression reduces the measurement noise without significantly reducing the spatial resolution and velocity gradients.

Q is a scalar quantity and has no direction. Therefore occasionally a 2D swirling strength is used to discriminate between streamwise, spanwise and wall-normal vortices. The swirling strength criterion (Zhou et al. 1999) uses the imaginary part of the complex

conjugate eigenvalues λ_{ci} of $\nabla\mathbf{V}$, which is always positive (or zero when $\nabla\mathbf{V}$ has only real eigenvalues). Instead of the full velocity gradient tensor, the 2D swirling strength uses only the velocity components and gradients in a 2D plane. For instance the spanwise swirling strength $\lambda_{ci,z}$ considers only the velocity in the x,y plane and is defined as the imaginary part of the eigenvalues of J_{uv} given by:

$$J_{uv} = \begin{bmatrix} \frac{\partial u}{\partial x} & \frac{\partial u}{\partial y} \\ \frac{\partial v}{\partial x} & \frac{\partial v}{\partial y} \end{bmatrix} \quad (7.9)$$

Similarly the streamwise swirling strength $\lambda_{ci,x}$ and wall-normal swirling strength $\lambda_{ci,y}$ are the imaginary part of the eigenvalues of J_{vw} and J_{uw} respectively. Finally the 2D swirling strength can be given a sign using the corresponding component of vorticity (e.g. $\lambda_{ci,z} \cdot \text{sign}(\omega_z)$) to differentiate between clockwise and anti-clockwise planar swirling motion.

7.3.2

Conditional averaging by linear stochastic estimation

For the statistical evaluation of the flow structures linear stochastic estimation (Adrian 1996, Christensen and Adrian 2001) is used to approximate the average velocity field associated to a specified event E at location x',y',z' . In its simplest form E is a scalar quantity obtained or derived from the measured velocity distributions, for example u' , a single component of the vorticity vector or swirling strength. The conditional average $\langle \hat{\mathbf{V}}(x,y,z) | E(x',y',z') \rangle$ is then written as a linear function of the event E , where the coefficient is obtained by minimizing the mean-square error between the estimate and the conditional average. For the fluctuating components of velocity (u' , v' , w') this results in:

$$\begin{aligned} \langle \hat{u}'(x'+r_x, y, z'+r_z) | E(x', y', z') \rangle &\approx \frac{\langle u'(x'+r_x, y, z'+r_z) \cdot E(x', y', z') \rangle}{\langle E(x', y', z')^2 \rangle} E(x', y', z') \\ \langle \hat{v}'(x'+r_x, y, z'+r_z) | E(x', y', z') \rangle &\approx \frac{\langle v'(x'+r_x, y, z'+r_z) \cdot E(x', y', z') \rangle}{\langle E(x', y', z')^2 \rangle} E(x', y', z') \\ \langle \hat{w}'(x'+r_x, y, z'+r_z) | E(x', y', z') \rangle &\approx \frac{\langle w'(x'+r_x, y, z'+r_z) \cdot E(x', y', z') \rangle}{\langle E(x', y', z')^2 \rangle} E(x', y', z') \end{aligned} \quad (7.10)$$

As seen from the equation the conditional average is estimated by unconditional two-point correlations, which are much easier to compute than the conditional average itself. Furthermore it is important to note that the estimate uses the fluctuating velocity components u', v', w' relative to the local average and that the estimate is linear, so that the character of estimate does not change with the value of E . Finally if it is assumed that in a boundary layer the two-point correlations are independent of the x and z coordinate, then the conditional average is only a function of $r_{x,y}$ and r_z and $\langle \dots \rangle$ in Eq. 7.10 denotes averaging over all samples as well as spatial averaging in x and z .

Chapter 8

Low speed turbulent boundary layer ($Re_\theta = 1900$)

The instantaneous 3D velocity distribution in a turbulent boundary layer at $Re_\theta = 1900$ has been measured using tomographic-PIV. The 3D vortical structures are visualized in the measurement volumes covering the logarithmic layer and the wake region. In the logarithmic layer predominantly asymmetric hairpin vortices are observed, which size, inclination and spatial organization into hairpin packets will be discussed. Furthermore ejection and sweep events with a maximum contribution to the Reynolds shear stress are detected and presented in relation to the vortical structures. In the wake region large-scale arch and cane vortices are observed, which appear to be randomly distributed.

8.1

Introduction

The coherent motion in turbulent flow is commonly associated with vortical structures, as discussed in the previous chapter. Moreover vortices are the key elements in many fluid dynamic models for wall-bounded turbulence. Therefore extensive research has been carried out into their characteristic shape in a turbulent boundary layer often using qualitative flow visualization techniques, i.e. smoke and dye visualizations. The interpretation of these visualizations, however, has an important visual, hence subjective, component (Delo et al. 2004) and is further complicated by the fact that smoke diffuses much slower than vorticity so that it tends to maintain its pattern longer than the actual flow especially at low Reynolds numbers (Antonia et al. 1990). Despite these difficulties, hairpins could be shown to exist in the turbulent boundary layer. Moreover, smoke visualizations by Head and Bandyopadhyay (1981) showed that hairpin vortices travel in groups. And more recently Adrian et al. (2000) proposed the organization of hairpins in packets based on quantitative visualizations using planar PIV measurements. Hairpin packets are marked by a streamwise alignment of hairpin vortices convecting at the same velocity and inducing a common zone of uniform (low speed) flow between their legs. Therefore they may be regarded as a coherent structure in itself. The packet structures have been studied experimentally by their signatures in 1D and 2D measurements (Adrian et al. 2000, Ganapathisubramani et al. 2003 and Marusic 2001) and have been visualized in DNS data (Adrian and Liu 2002).

So far the 3D shape of the coherent structures could be studied only from DNS. The commonly observed vortices can be divided into streamwise and hairpin vortices, where the latter is used as a general term to denote horseshoe, arch, cane and hairpins. In the famous work by Robinson (1991) it is found that the buffer layer is dominated by quasi-streamwise vortices and that arches populate the wake region. The logarithmic layer contains of both arches and streamwise vortices. Experimental validation of these conclusions exists only in part through studies of the structure signatures and statistics in lower dimensional data. Furthermore the Reynolds number accessible by DNS is limited. Robinson for example based his conclusions on data computed by Spalart (1988) at $Re_\theta = 670$.

The present study proposes to use tomographic-PIV to measure the instantaneous three-dimensional velocity distribution in the logarithmic layer and wake of a $Re_\theta = 1900$ turbulent boundary layer, which allows to quantitatively visualize the 3D coherent structures. Hence the structures can be investigated experimentally without being affected by assumptions or prior knowledge usually needed to produce the signatures or by interpretation difficulties associated to qualitative dye visualizations. The aim it is to compare the findings with results from the large amount of related works in literature at similar Reynolds numbers. The results will also serve as a basis for discussion of coherent motion in the supersonic boundary layer, later on in chapter 10, for which considerable less information is available in literature. The focus will be on the vortical structures, hairpin packets with low speed regions, ejections and sweeps, which probably are the most reported structural elements (chapter 7). The experimental arrangement is presented in section 8.2 followed by the boundary layer statistical properties and the instantaneous results will be shown in section 8.3.

8.2 Experimental setup

The experiments are performed in the $40 \times 40 \text{ cm}^2$ cross-section wind tunnel at the Aerodynamics Laboratories of the Delft University of Technology. The test section is made out of Plexiglas for good optical access (figure 8.1). The turbulent boundary layer on the lower tunnel wall is investigated at a free-stream velocity U_e of 9.9 m/s and $Re_\theta = 1900$. The boundary layer thickness δ_{99} , displacement thickness δ^* and momentum thickness θ are 24 mm, 4.2 mm and 2.9 mm respectively. A tripping wire is placed 1.2 m upstream of the measurement location to fix transition.



Figure 8.1. Experimental arrangement. Left: low speed wind tunnel with Plexiglas test section (A). Right: camera setup for tomographic-PIV underneath the test section (used for configurations I and II).

Tomographic-PIV measurements are performed in the 3 configurations presented in Table 8.1. For the first two configurations the laser sheet is aligned parallel to the wall (x - z plane, where x is the free stream direction and z the spanwise direction) and is then expanded in wall normal direction y to 12 mm thickness. Configuration I covers the lower part of the boundary layer and configuration II the upper part. In configuration III the light sheet is aligned with the x - y plane and expanded in span yielding complementary

information on the flow structures over the complete boundary layer thickness, but with a reduced spanwise extent. In each configuration 250 instantaneous snapshots are obtained.

The flow is seeded with 1 μm droplets produced with a fog generator to a particle image density of approximately 0.05 particles per pixel. The illumination is provided by a Nd:YAG dual-head laser of 400 mJ pulse energy within 6 ns. The light sheet thickness is controlled by a slit placed after the laser sheet formation optics. The particle image recording is performed with four cameras organised within a solid angle of 40x30 degrees (figure 8.1). Scheimpflug adapters are installed between the sensor and the 50 or 60 mm focal length objectives. The lens $f_{\#}$ is set at 8.0. Four LaVision Imager Intense CCD cameras (1376x1040 pixels, 12 bits) are employed to record the light scattered by the particles. The average imaging magnification is $M = 0.18$ corresponding to a resolution of 27 pixels/mm. The time separation between subsequent exposures is set at 100 μs , yielding a particle displacement of 26 voxels in the free stream. Therefore the dynamic range of the present system is 260, given a cross-correlation accuracy of 0.1 voxel particle displacement.

Image pre-processing on the particle recordings (background removal, intensity normalization and Gaussian smooth on a 3x3 kernel) is applied to improve the volume reconstruction by the MART algorithm described in section 3.3. The reconstruction is stopped after five iterations returning the reconstructed volume, which is discretised at 27^3 voxels per mm^3 .

In the cross-correlation analysis of the 3D reconstructed objects the interrogation box size is progressively decreased to 50^3 voxels (configuration I) or 42^3 voxels (configuration II and III). A 75% overlap factor is applied between neighboring boxes returning an overall measurement grid consisting of typically 80x60x25 vectors with a vector spacing of 0.4 mm (Table 8.1) corresponding to 14 viscous length scales. Data validation based on the normalized median test (Westerweel and Scarano 2005) returns approximately 5% spurious vectors.

Table 8.1. Dimensions of the measurement configurations

Configuration	Δx (mm)	y range (mm)	Δz (mm)	size vector grid (x,y,z)	vector spacing (mm)
I	33	1 – 12	26	69 x 25 x 54	0.44
II	34	8 – 20	26	84 x 32 x 66	0.38
III	42	0 – 30	10	84 x 66 x 21	0.47

The mean velocity profile is plotted in inner variable scaling in figure 8.2-top, where

$$u^+ = \frac{u}{u_\tau} \quad \text{and} \quad y^+ = \frac{u_\tau}{\nu} y \quad \text{with} \quad u_\tau = \sqrt{\frac{\tau_w}{\rho}} = \sqrt{\nu \left(\frac{\partial u}{\partial y} \right)_w}$$

where the subscript w demotes conditions at the wall. The tomographic-PIV result from configuration III is compared with one-component hot wire anemometry and stereoscopic-PIV data. For the latter method two cameras from the tomographic-PIV optical arrangement are used in combination with a 1 mm thin light sheet. From the comparison it is concluded that the different methods show a good agreement. Moreover the data have been fitted to the log-law region of the Spalding (1961) composite formula for the wall to obtain the friction velocity $u_\tau = 0.45$ m/s (see Table 8.2 for a summary of the boundary layer properties). The log-layer is found to extend up to $y^+ = 200$, corresponding to $y = 6.9$ mm, where the experimental data start to depart from the theoretical profile.

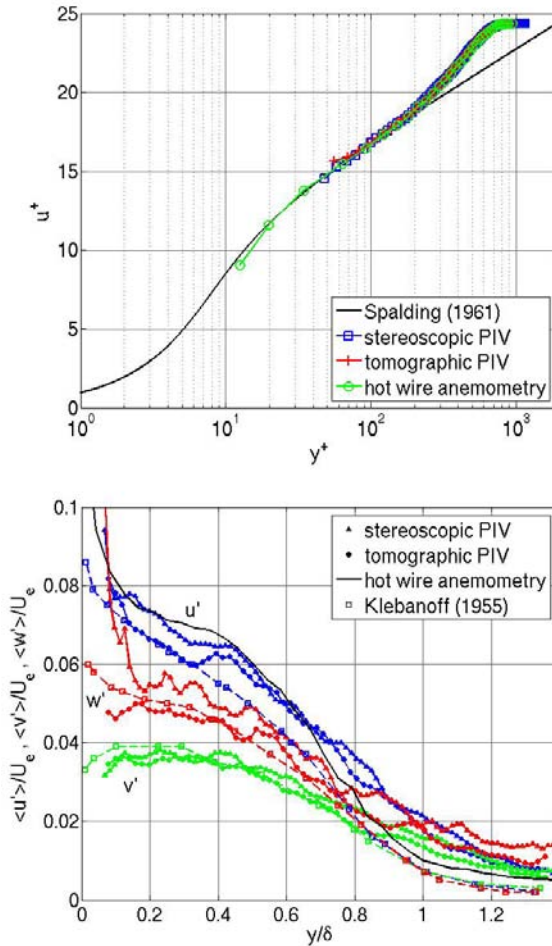


Figure 8.2. Mean velocity profile (top) and RMS profiles for the three components of velocity (bottom).

The turbulence intensities are presented in figure 8.2-bottom, where one-component hot-wire anemometry and stereoscopic-PIV results are again added to validate the tomographic-PIV measurements. Near the wall, $y/\delta < 0.5$, there is a clear difference between the three components of velocity with the smallest fluctuations in the v -component and the largest in the u -component, as expected. Further from the wall the profiles show decreasing velocity fluctuations with y reaching isotropic turbulence conditions approximately at the boundary layer edge $y/\delta = 1$. The tomographic-PIV fluctuating velocities agree within $0.005U_e$ with stereoscopic-PIV, which corresponds to approximately 0.1 pixel particle displacement. However, very close to the wall ($y/\delta < 0.15$) the w -fluctuations are overestimated by stereoscopic-PIV, which is probably related to erroneous reconstruction of the out-of-plane component in the presence of strong local velocity gradients over the laser sheet thickness (Wieneke and Taylor 2006). Furthermore a comparison with the Klebanoff (1955) hot wire

data reveals higher u -fluctuations in the present boundary layer and also a higher overall turbulence level in the free stream ($y/\delta > 0.8$). The differences are approximately $0.01U_e$ corresponding to approximately 0.2 voxel particle displacement in tomographic-PIV. Finally the single hot-wire is sensitive to both u and v -fluctuations, which makes the final result a non-linear combination of the two. However the hot wire seems to confirm the elevated u -fluctuations in the present boundary layer with respect to the Klebanoff data. Based on the above it may be concluded that the uncertainty in the PIV measurement is 0.1 to 0.2 voxel particle displacement.

Table 8.2. Boundary layer properties

U_e	9.9 m/s
δ_{99}	24 mm
δ^*	4.2 mm
θ	2.9 mm
$H = \delta^*/\theta$	1.4
u_τ	0.45 m/s
u_τ/ν	34 mm^{-1}
δ^*	710
c_f	$4.2 \cdot 10^{-3}$
Re_θ	1900

8.3

Instantaneous flow organization

The instantaneous results are presented in coordinates normalized with the boundary layer thickness δ . The time average velocity is subtracted in all vector plots to clearly show swirling motion and regions of low and high velocity. The emphasis will be on the results obtained in configuration I near the wall, as the flow displays a higher degree of organization at that location.

8.3.1

Vortical structures

An example of the returned vortex structures in a single snapshot of the lower part of the boundary layer (configuration I) is presented in figure 8.3. Individual ‘blobs’ are color coded for clarity (note that the Q -threshold is identical for all detected structures and

approximately equal to $2 \cdot 10^{-4} \left(\frac{\partial u}{\partial y} \right)_w^2$). Each blob, however, may still consist of a number of

vortices in close proximity, which is the general disadvantage of local vortex detection schemes such as the Q -criterion. Moreover blobs smaller than a single cross-correlation volume are removed, because they are considered incoherent in space.

In the lower part of the boundary layer mostly asymmetric hairpin, arch or cane vortices are observed. The results also contain more complicated structures (e.g. structure B and D in figure 8.3-top), which are considered to be combinations of these vortices. Individual streamwise vortices are found near sweeps having a length of approximately 0.2δ (see section 8.3.3). But more often they are part of hairpin or cane vortices (the legs), as has also

been observed by Robinson (1991) in DNS data at $Re_\theta = 670$. Figure 8.3-top also shows short vortices at the top of the volume (e.g. structures A, C, E and F), which are thought to be the legs of hairpin or cane vortices with the corresponding heads located higher up in the boundary layer.

A single cane vortex structure is isolated from the volume and presented in top and side view in figure 8.3-bottom. The height and width of this vortex are 0.4δ and 0.3δ respectively. The velocity vectors reveal a swirling motion around the neck (top) and head of the cane (bottom). As expected, the vortex induces low speed flow ($u' < 0$) between its legs with a Q2 event ($u' < 0, v' > 0$) below and just upstream of the vortex head.

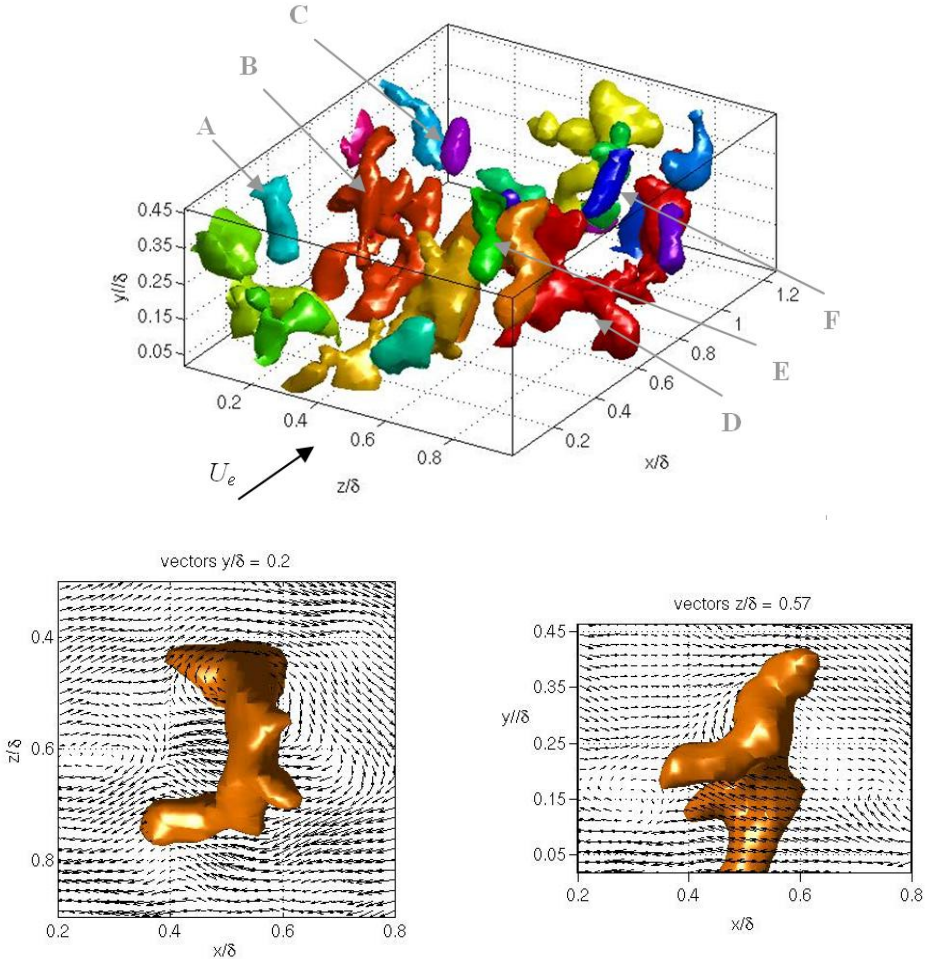


Figure 8.3. Vortex structures in the low part of the boundary layer (configuration I, top) and details of the velocity field near a single vortex structure (bottom).

In the upper part of the boundary layer (configuration II) a larger variety of vortex structures is observed, which cause the turbulence to become less organized and more isotropic towards the boundary layer edge as observed in the fluctuating velocity profiles

(figure 8.2-bottom). Figure 8.4 shows examples of the non-hairpin-like vortex structures returned in the upper part of the boundary layer. The coherent structures at this height include arch vortices deflected with respect to the spanwise direction (up to 40 degrees, figure 8.4-left) and the different smaller scale vortex structures found in the volume of figure 8.4-right together with some large scale canes. With increasing distance from the wall the structures also become larger, as expected. At $y/\delta = 0.6$ the width of the largest structures is approximately 0.5δ .

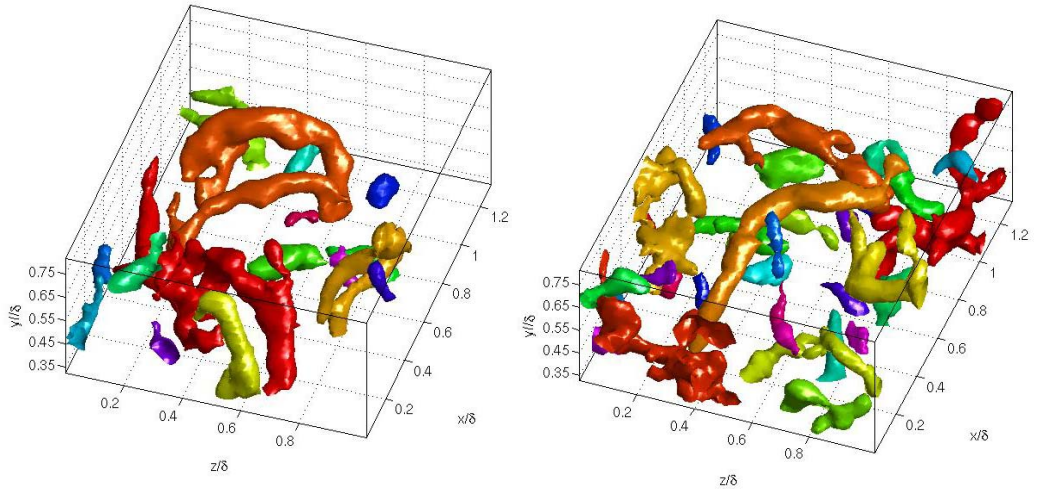


Figure 8.4. Vortex structures in the upper part of the boundary layer (configuration II).

A statistical description of the hairpin vortex structures is provided by the conditional average eddy obtained by linear stochastic estimation (section 7.3.2), where the specified event is the negative spanwise swirling strength $\lambda_{ci,z}\text{sign}(\omega_z)$ at height y/δ in the boundary layer. The result may be interpreted as the average flow field associated with this event, which corresponds to the hairpin vortex head as seen from the result for the spanwise swirl event at $y/\delta = 0.35$ (figure 8.5). The Q vortex detection criterion shows an arch or hairpin structure (green, figure 8.5-left) on top of a low speed zone (gray). Moreover the velocity vectors with respect to the average velocity in the wall normal plane $r_z/\delta = 0$ and in the plane parallel to the wall at $y/\delta = 0.20$ (figure 8.5- right) reveal the typical signature of a hairpin structure in these planes. The former plane shows again spanwise swirling motion at the specified location $y/\delta = 0.35$ ($r_x/\delta = 0$), as well as the characteristic ejection ($u' < 0, v' > 0$) below and just upstream of the hairpin head and shear layer separating the low-momentum and incoming high-momentum flow upstream of the vortex. The shear layer interface is inclined at approximately 20 degrees with the wall. The velocity vectors in the plane parallel to the wall (figure 8.5-bottom-right) shows swirling motion around both necks of the conditional eddy ($r_x/\delta = -0.1$) and flow stagnation, relative to the average velocity, upstream at approximately $r_x/\delta = -0.4$ and $r_z/\delta = 0$.

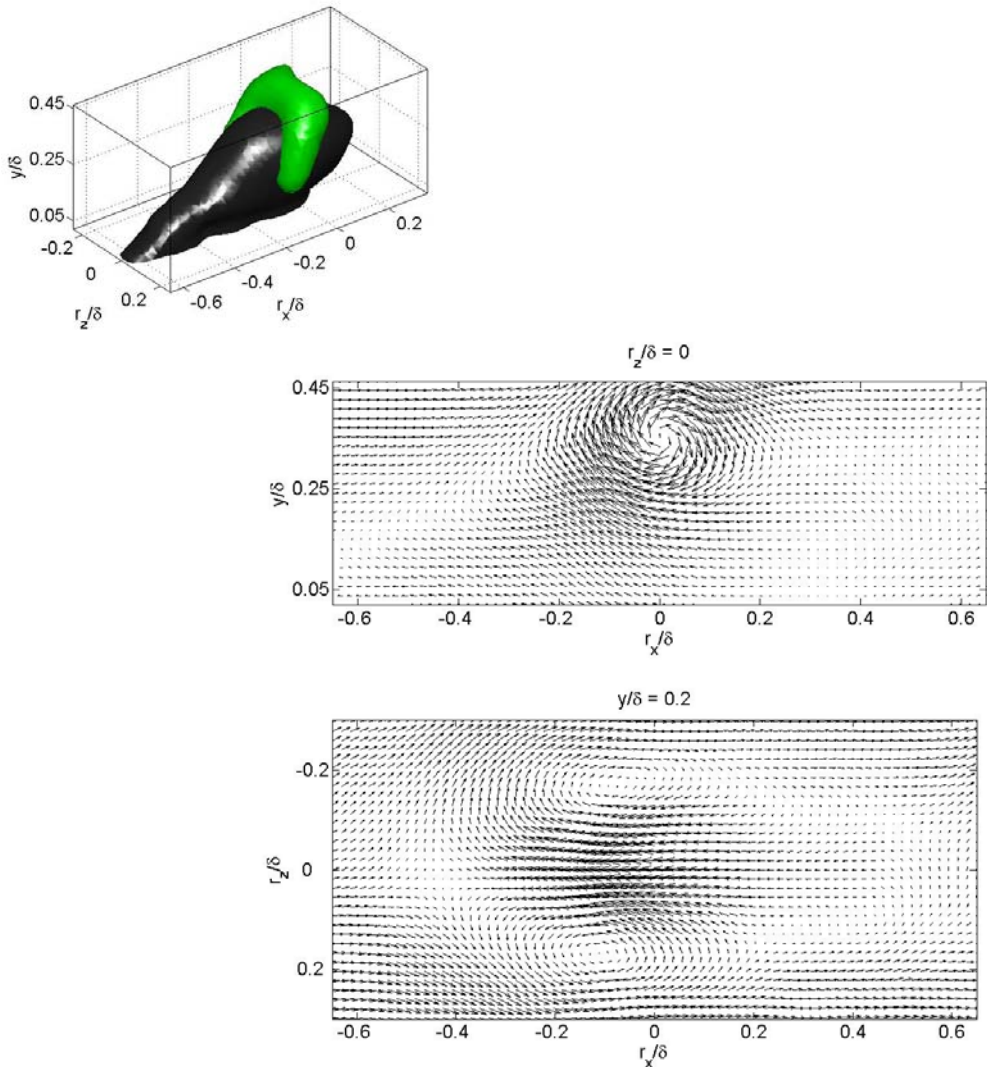


Figure 8.5: Conditional eddy (top-left) given a negative spanwise swirling event at $y/\delta = 0.35$ in the $Re_\theta = 1900$ turbulent boundary layer. Vortical motion is visualized using the Q vortex detection criterion (green) and low speed zones (gray, $u' < 0$) with corresponding velocity vector plot in the x,y and x,z cross-sections (right). The velocity vectors are relative to the local average velocity.

Figure 8.6 presents the conditional eddies for negative spanwise swirl at different heights in the boundary layer between $y/\delta = 0.1$ and 0.8 . The resulting vortices are placed along an artificial slope for illustration purposes. It should be stressed that this slope does not correspond to any physical growth rate of the structures in streamwise direction or time.

From the side-view (figure 8.6-top) it can be seen that the neck of all conditional eddies are inclined at approximately 45 degrees with the wall. The top-view (figure 8.6-bottom) reveals a linear spanwise growth of the conditional eddy with distance from the wall y/δ as indicated by the two red solid lines. Based on these line fits, the width of the conditional eddy Δz_{eddy} can be related to the corresponding height of the vortex head y_{head}/δ as:

$$\frac{\Delta z_{eddy}}{\delta} = 0.35 \frac{y_{head}}{\delta} + 0.12 \quad (8.1)$$

Interestingly the width does not go to zero at the wall, but remains positive and finite. Tomkins and Adrian (2003) in their analysis of the near wall low-speed streaks also observe this behavior.

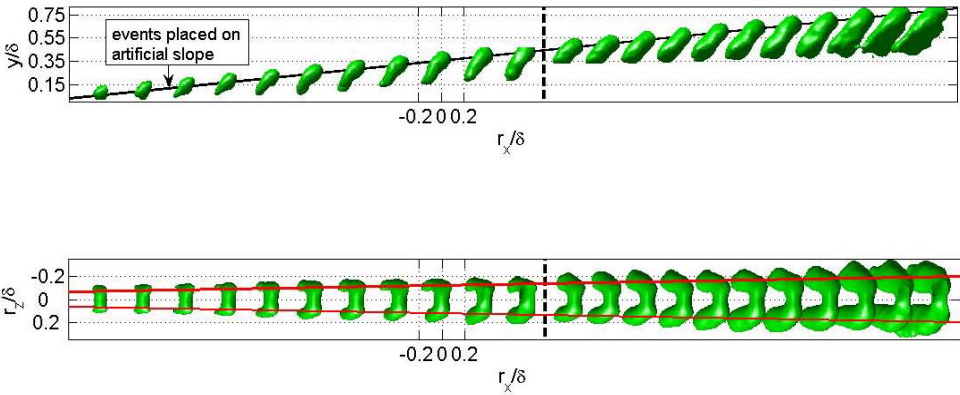


Figure 8.6. Side view (top) and top view (bottom) of the conditional eddies based on a negative spanwise swirl event at different height in the boundary layer visualized using the Q vortex detection criterion. Eddies to the left and right of the dashed line are obtained in measurement configuration I and II respectively. For illustration purposes the eddies are displaced in horizontal direction so that the events lie on the solid line (top figure) inclined at an arbitrary angle with the wall. The red solid lines in the bottom figure indicate the width of the eddies.

8.3.2

Low speed zones and hairpin packets

Figure 8.7 shows the instantaneous spatial organization of vortices into packets, which are formed by streamwise aligned hairpin vortices inducing a common low speed zones between their legs. The vortical structure are identified as before, whereas a low speed zone (gray) is defined as a region with $u < 90\%$ of the local mean velocity. Two hairpin packets can be seen close to the wall ($y/\delta < 0.2$, denoted A) and in the middle of the volume ($y/\delta < 0.35$, B) containing 2 and 3 hairpin vortices respectively. The relatively small number

of hairpin vortices per packet was expected based on previous observations with planar PIV at a similar Reynolds number (Adrian et al. 2000). A third low speed zone (C) is located at the top of the volume. However hairpin heads, if present, are outside the measurement domain, so it is not clear whether structure C is also a packet. Using the present visualization method, one or more packets can be observed in most of the snapshots ($>90\%$) near the wall (up to $y/\delta = 0.5$, configuration I). As shown above the vortical structures in the upper part of the boundary layer appear more random and do not reveal a clear streamwise alignment (figure 8.4, configuration II), which is consistent with earlier observations (Adrian et al. 2000, Ganapathisubramani et al. 2003, Marusic 2001).

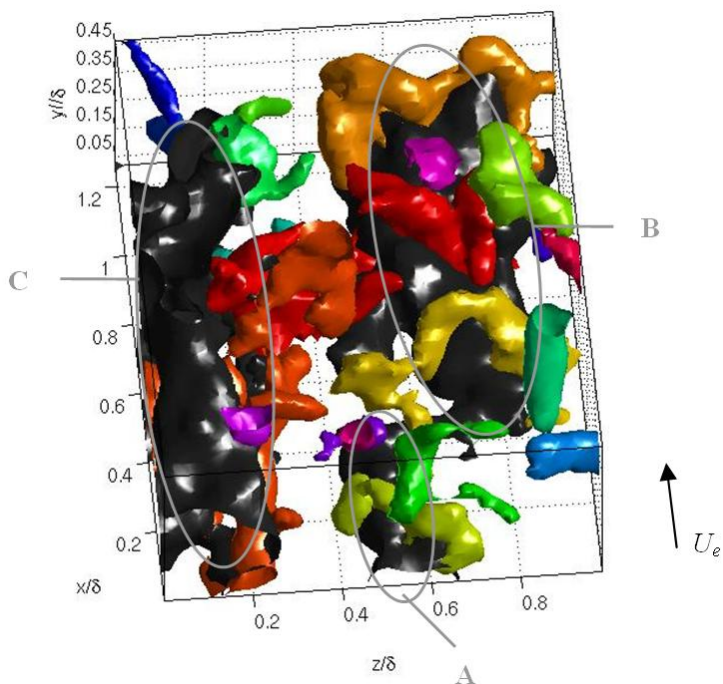


Figure 8.7. Vortex structures around regions of low speed ($u < 90\%$ of the mean velocity, gray) in the lower part of the boundary layer (configuration I).

Packet B in figure 8.7 will be discussed in more detail. The packet is 0.35δ wide, 0.35δ high, $>0.8\delta$ long and consist of an arch vortex followed by two m-shaped vortices downstream. This double arch may indicate that the vortex structures are in the process of merging or splitting. The streamwise spacing between the vortex heads is approximately 0.3δ . The top and side view of the packet (figure 8.8) show spanwise and upward growth in streamwise direction. The latter is estimated at 12 degrees, which is in good agreement with planar PIV data (Adrian et al. 2000 and Christensen and Adrian 2001) and smoke visualization studies (Head and Bandyopadhyay 1981). Furthermore the side view (figure 8.8-bottom) shows the inclination of the vortex necks (or legs), which is estimated at 45 degrees for the most upstream vortex and increases to 70 degrees for the most downstream vortex at larger distance from the wall. Note that the two downstream vortices do not extend

down to the wall and that also the thickness of the upstream vortex decreases close to the wall.

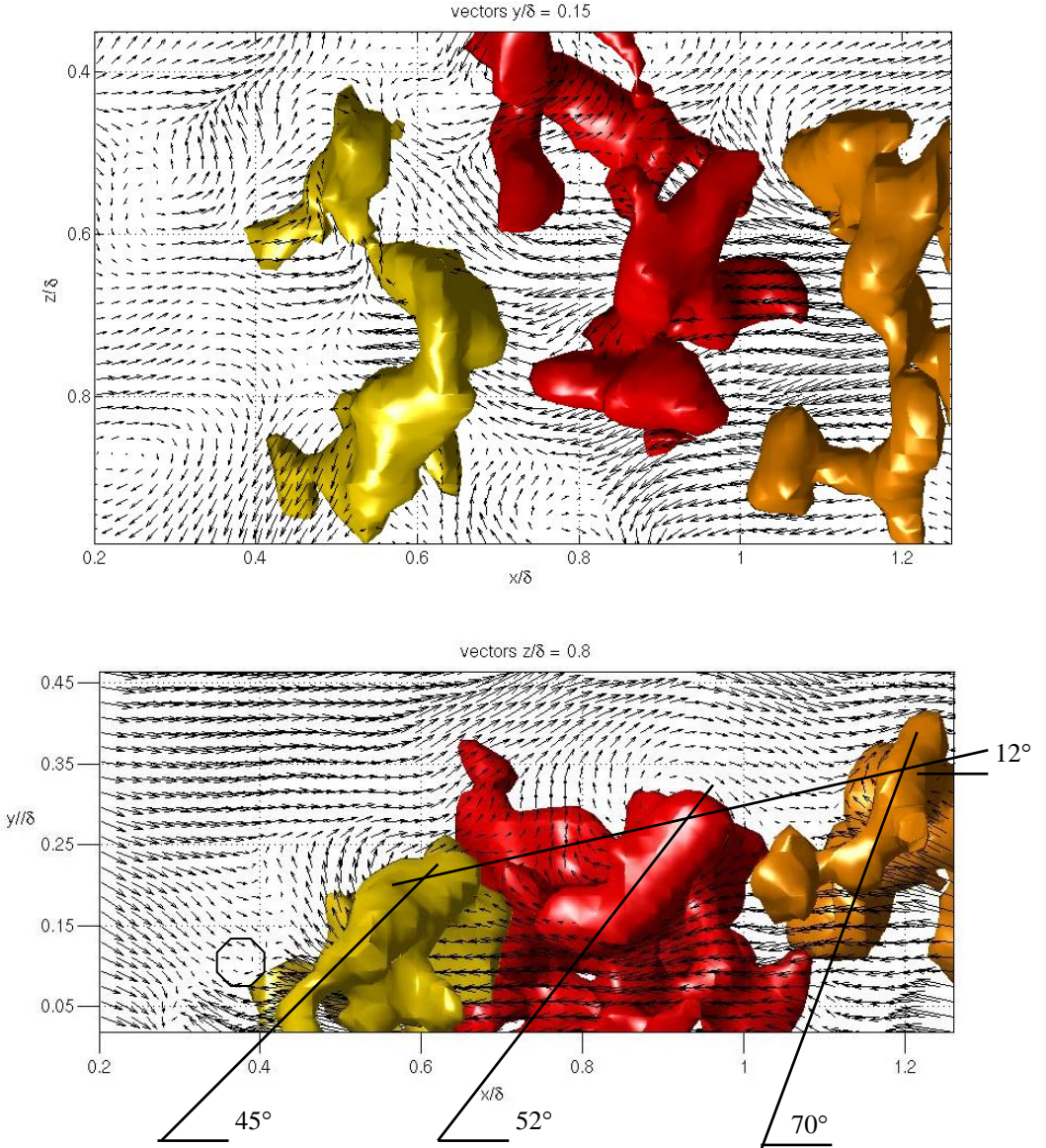


Figure 8.8. Top and side view of vortex packet B in figure 8.7.

The velocity vectors (figure 8.8) return the characteristic signatures of the packets in the x,z and x,y plane. A single zone of low flow velocity ($u' < 0$) is clearly visible underneath the vortex heads. In front of the packet the low velocity interacts with the incoming high velocity flow along a curved interface, which is best seen in x,y plane (figure 8.8-bottom). On the interface a weak swirling motion is observed (indicated by the circle), which suggests the formation of a new vortex from an instability in the interface. Moreover preliminary results from a time-resolved tomographic-PIV measurement of a low Reynolds number turbulent boundary layer (Schröder et al. 2006 and section 9.3.2) reveal vortex formation upstream of an older vortex after a sweep event ($u' > 0, v' < 0$), which is seen in figure 8.8-bottom above and upstream of the circle. Furthermore a flow stagnation point is found at $x/\delta = 0.43, z/\delta = 0.75$.

The cross sectional area of the low speed zone decreases in upstream direction. To satisfy continuity strong outward motion in spanwise direction w (figure 8.8-top) and wall normal direction v (figure 8.8-bottom) is present between the vortices.

8.3.3

Ejections and sweeps

Ejection and sweep are defined respectively as the transport of low momentum away from the wall ($u' < 0, v' > 0$ also known as Q2 event) and the transport of high momentum fluid towards the wall ($u' > 0, v' < 0$ also known as Q4 event). Both events yield important contributions to the Reynolds shear stress $\overline{u'v'}$, as can be seen in a plot of the joint probability function of u' and v' multiplied by $u'v'$ at $y/\delta = 0.13$ (figure 8.9). The PDF is not fully converged due to the limited number of snapshots, but does provide an indication of the Q2 and Q4 events with maximum contribution to the Reynolds shear stress. For Q2 events a peak is returned at approximately $u' = -1.1, v' = 0.5$ and for Q4 events at $u' = 1.0, v' = -0.4$.

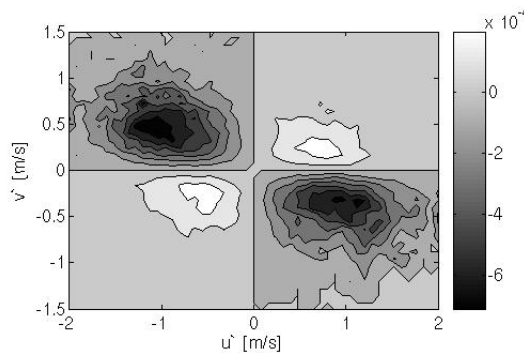


Figure 8.9. Joint PDF of u' and v' multiplied by $u'v'$ at $y/\delta = 0.13$ (m^2/s^2).

All snapshots are searched for a Q2 event $u' = -1.1, v' = 0.5$, corresponding to the event with the maximum contribution to the Reynolds shear stress, in a cubic control volume (length 0.07δ) around $(x;y;z) = (0.45;0.13;0.45)\delta$. The snapshots detected in this procedure account for 76% of the total Reynolds shear stress related to Q2 events in the control volume. Three examples of the vortex and low speed structure in a sub-volume around the detected event are presented in figure 8.10. The first volume (figure 8.10-top) shows a large

low speed zone enclosed by 3 large cane vortices extending down to the bottom of the measurement volume and a number of smaller vortices. Inside this packet a small scale vortex is detected at $x/\delta = 0.48$, $y/\delta = 0.13$ (marked blue in the corresponding vector plot, figure 8.10-top-right), which is relatively weak in terms of vorticity. However the perturbation in v' induced by the small vortex superimposed on the negative u' induced by the large-scale packet returns a relatively strong Q2 event as seen in the corresponding contour plot. In a similar way the three vortices in the packet shown in the second volume ($0.4 < x/\delta < 1$, $y/\delta < 0.2$, figure 8.10-middel) work together to produce significant Q2 events. The highest value for Q2 is found in front of the upstream vortex. It is interesting to note that the second sub-volume contains two additional packets, one at the top of the volume and one upstream $x/\delta < 0.2$, which again demonstrates that packets occur frequently.

The last example (figure 8.10-bottom) shows an individual cane vortex. Even though it is a strong vortex the induced Q2 (figure 8.10-bottom-right) is low compared to the previous examples. Therefore it is concluded that wall normal and streamwise alignment (packet) of hairpin or cane vortices provide an important mechanism for the Reynolds shear stress production by Q2 events. It is also a statistically relevant mechanism as in approximately 70% of the detected snapshots some form of vortex alignment is observed near the Q2 event. Moreover Ganapathisubramani, Longmire and Marusic (2003) found that vortex packets contribute 28% to the total Reynolds shear stress.

A similar procedure is followed to detect Q4 events. Two representative results are shown in figure 8.11. As seen from the Q4 contours (figure 8.11-right) sweeps are predominantly found on the outboard side of the hairpin or cane necks, which is consistent with Robinson (1991). Figure 8.11 also shows streamwise vortices of 0.2δ length (A, B and C) inducing downward motion.

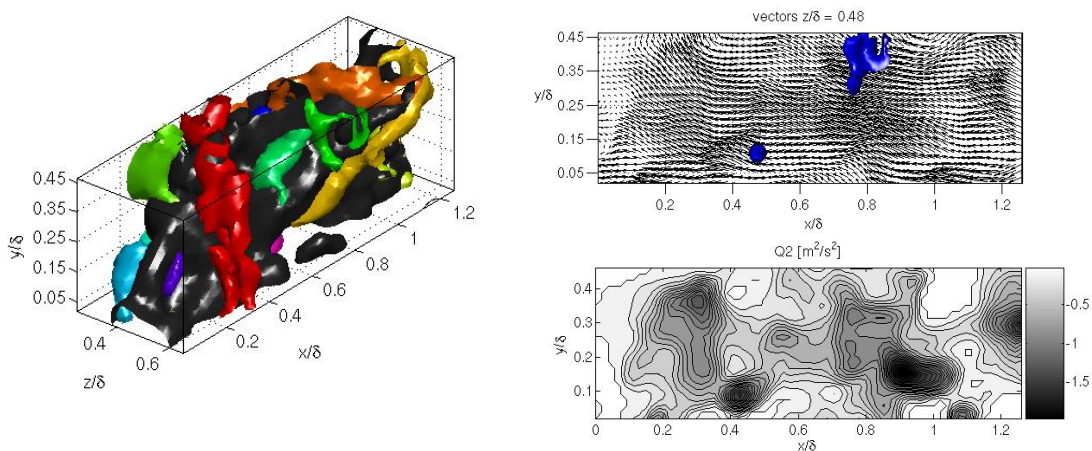


Figure 8.10. Vortex structures and low speed regions (gray) showing decreasing level of spatial vortex organization (left, from top to bottom) and corresponding vector and Q2 plots in the x,y plane (right).

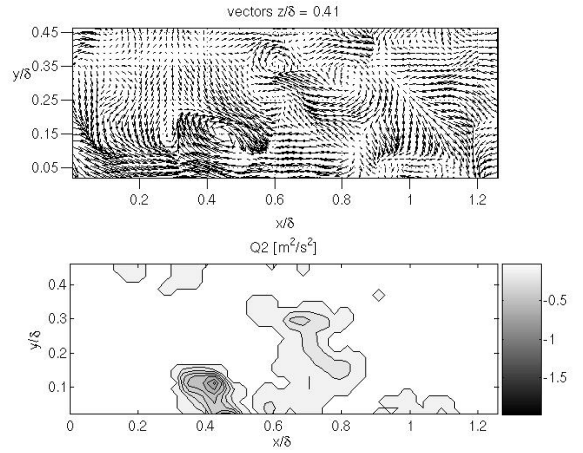
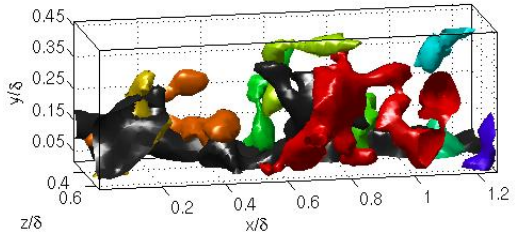
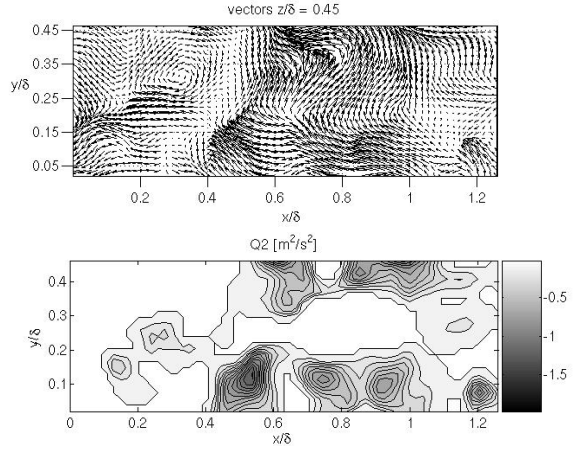
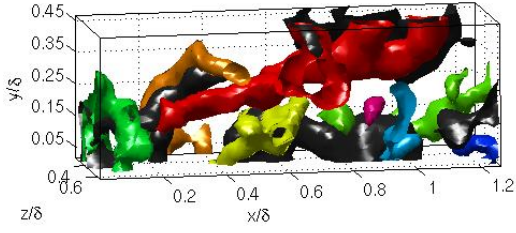


Figure 8.10 continued.

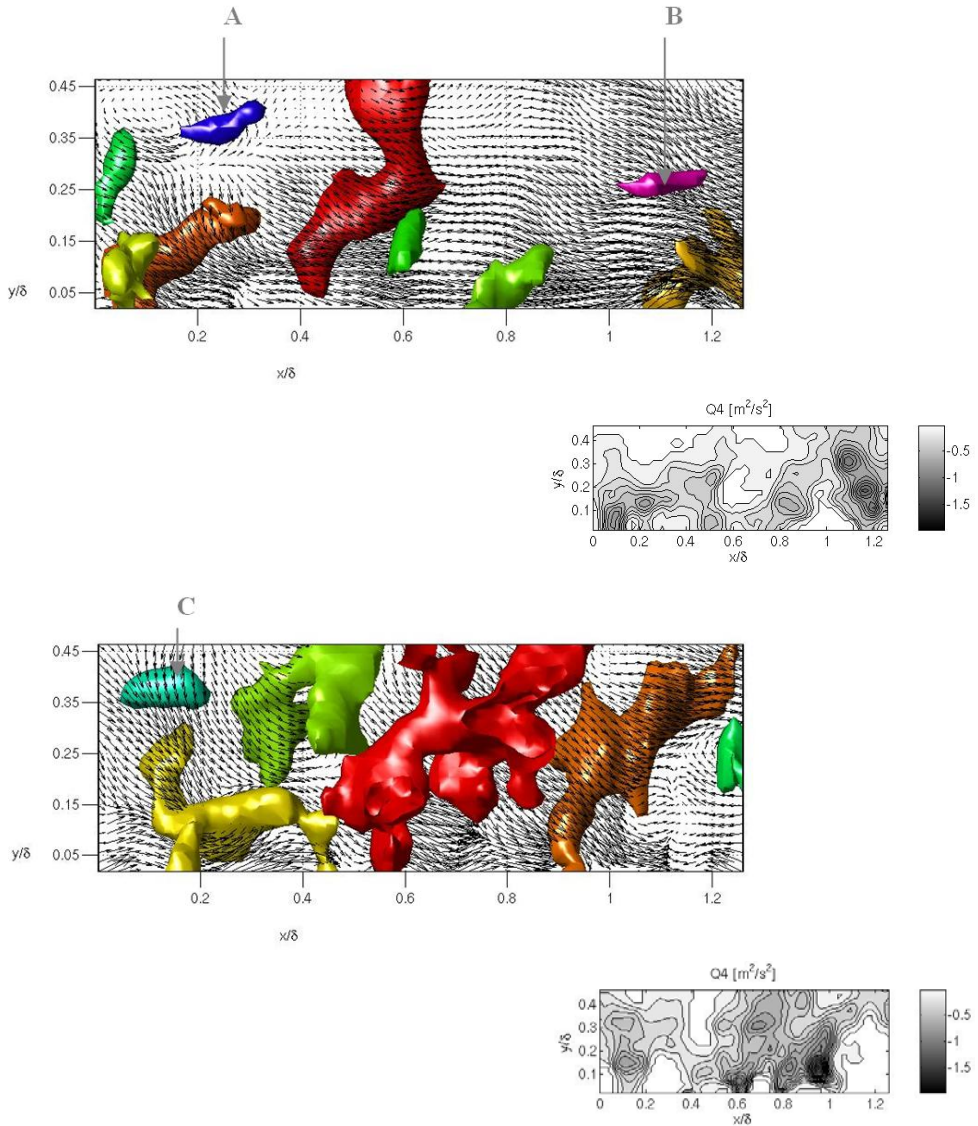


Figure 8.11. Examples of vortex structures near Q4 events with corresponding vector plot (left) and Q4 plots in the x, y plane (right).

8.4 Conclusions

The application of 3D tomographic-PIV to a turbulent boundary layer at $Re_\theta = 1900$ has been presented. The returned velocity statistics are in good agreement with stereoscopic-PIV and the instantaneous results clearly reveal the 3D coherent motion in the logarithmic layer and wake. The vortical structures are deduced applying the Q-criterion, which detects local

swirling motion as is shown by the vector plots. In the lower part of the boundary layer ($y/\delta < 0.5$) predominantly asymmetric hairpin vortices have been observed. Streamwise vortices are found near sweep events having a length of approximately 0.2δ . Furthermore hairpin packets containing 2 to 4 streamwise aligned vortices are observed to occur frequently at this height in the boundary layer. The packet upward growth rate in streamwise direction and inclination of the individual hairpin necks (or legs) agree well with reported values in flow visualization and planar PIV studies. The direct observation in the measured 3D velocity distributions provides additional experimental evidence for the existence of the hairpin and packet structures.

Hairpin packets and vortex alignment in wall-normal direction yield important contributions to the Reynolds shear stress production through Q2 events ($u' < 0, v' > 0$) as predicted by Adrian et al. (2000). The perturbation in wall-normal velocity v' induced by a single vortex superimposed on the large negative u' induced by a packet returns a relatively large $-u'v'$. Sweeps are predominantly found on the outboard side of the hairpin or cane necks.

Signs of vortex formation are observed in front of a packet on the interface between the low velocity induced by the packet and the incoming high velocity flow. However, more (statistical) evidence is needed to reach conclusions on the relevance of vortex formation upstream of packets.

Finally a broad range of vortex structures is returned in the wake region of the boundary layer (figure 8.4) such as deflected arches and large-scale canes.

Chapter 9

On the life of a hairpin

The Tomographic-PIV technique has been applied to time resolved particle image recordings for the study of the temporal growth of hairpin vortices within a tripped turbulent flat plate boundary layer flow. The experiments are performed around $Re_x^{1/2} = 630$ in a low speed wind-tunnel using four high speed CMOS cameras operating at 1.5 kHz (double frame). The volume illumination required a multiple-reflection system in order to increase light intensity within the measurement volume. The present measurement system yields a correlated time sequence of three-dimensional instantaneous velocity vector volumes, in which the time evolution of the coherent structures is visualized. Their development in time is dominated by convection and slow growth. The corresponding average velocities and growth rate are determined for a hairpin vortex using space-time correlations and feature tracking. Furthermore examples of hairpin vortex formation and death are given, which occur seldom, but exhibit a strong dynamic behavior with a relatively fast evolution.

9.1

Introduction

Considering the dynamics of the coherent structures most of the attention is directed to the near-wall region (e.g. Corino and Brodkey 1969, Kim et al. 1971, Smith and Metzler 1983, Smith et al. 1991, Jimenez and Simens 2001 among others), where especially the low speed streaks and the bursting phenomenon have been studied extensively using flow visualization and numerical simulations. Far less information is available on the dynamics of the structures in the outer part of a turbulent boundary, as described in the previous chapter, and it is generally assumed that rates of change are small, i.e. convection dominates over viscous diffusion and (vorticity) deformation. This assumption is the basis for Taylor's hypothesis of frozen turbulence (chapter 7), which finds wide application especially in probe measurements to relate time scales to length scales in the flow. Moreover the outer layer structures are often thought to have originated near the wall, after which they have increased in size by growth and merging processes (Tomkins and Adrian 2003).

The present chapter presents the application of Tomographic-PIV to time resolved particle image recordings for the investigation of the dynamics of hairpin structures in the outer part of a tripped turbulent boundary layer in air at low Reynolds number. The aim is twofold, firstly to illustrate the low degree of dynamics in this part of the boundary layer showing that hairpins are also coherent in time being essentially advected, and secondly to show that time-resolved three-dimensional velocity information can be obtained with the proposed method. The latter provides a technology demonstration. More specifically the growth rate and convective velocity will be established and rare, highly dynamic events as birth and death of hairpins will be touched upon. The discussion is restricted to hairpin type vortices, which are main features of the turbulent boundary layer, as has been shown in chapter 8. It is assumed that the time evolution of ejection and sweep events can be related to the growth of these vortex structures.

High-repetition rate PIV systems have recently appeared with technical specifications enabling to operate PIV in time-resolved mode for the study of the dynamics in low speed air flows. There is, however, a compromise between the repetition rate and the available laser pulse energy. Typically lasers pulse energy at 1 kHz is about one order of magnitude less than that for low rep-rate systems. Moreover CMOS sensors are lower quality imagers compared with CCD cameras, because of a larger pixel pitch and lower sensitivity (Hain et al. 2007). The tomographic technique poses even higher requirements in terms of illumination intensity and spatial resolution of the imaging system because the measurement volume is typically one order of magnitude larger than that for planar PIV due to the expansion of the sheet in depth. Moreover, the imaging system requires a finite depth of focus corresponding to the thickness of the illuminated region. This is usually achieved at the cost of a smaller optical aperture of the objectives, causing a further decrease of the particle image intensity. Below a specific illumination system will be described to improve the imaging conditions for the high-repetition rate system.

The experiments presented in this chapter were performed at the German Aerospace Centre DLR at Göttingen in cooperation with LaVision GmbH. The original work on a turbulent spot and a tripped turbulent boundary layer measured at 5 and 4 kHz respectively have been published in Schröder et al. (2006, 2008). Compared to these earlier works, the results shown here are for a tripped turbulent boundary layer at a higher Reynolds number measured at a lower repetition rate (1.5 kHz).

9.2 Experimental setup

The turbulent boundary layer flow has been generated in the 1m-wind tunnel of the German Aerospace Center, DLR, at Göttingen over a flat glass plate with elliptical leading edge at a free stream velocity of 10 m/s with zero pressure gradient (figure 9.1-right). A transparent plate is utilized to provide optical access from the bottom. The originally laminar boundary layer is tripped by a series of four wires placed at 3 mm intervals with the first located 180 mm downstream of the leading edge of the plate ($Re_x^{1/2} = 350$). The wire diameters are 0.5, 1.0, 0.5 and 1.5 mm in streamwise order. The tripped turbulent boundary layer is measured 580 mm downstream of the leading edge at $Re_x^{1/2} = 630$ in a volume spanning $34 \times 9 \times 40 \text{ mm}^3$ in streamwise (x), wall-normal (y) and spanwise (z) direction. At the measurement location the boundary layer thickness is estimated at 15 mm using a stethoscope and by fitting the $1/7^{\text{th}}$ power law to the average velocity profile obtained from Tomographic-PIV. From the same fit the Reynolds number based on momentum thickness is estimated at $Re_\theta = 960$.

The experimental arrangement and procedure is similar to the experiments presented in chapter 8, with two important modifications. First a high repetition rate PIV hardware is used, which consists of four Photron APX-RS CMOS cameras and a high repetition rate dual cavity diode-pumped Nd:YLF Pegasus laser from New Wave with a pulse energy of approximately 8 mJ at 1.5 kHz (pulse duration 180 ns). The high-speed cameras were equipped with 105 mm Nikon lenses ($f_\# = 5.6$) and Scheimpflug adapters and recorded 1024×1024 pixel double frame images at an image resolution of 19 pixels/mm and at repetition rate of 1.5 kHz (applying frame straddling). Consequently the time between consecutive velocity snapshots is 0.67 ms. The pulse separation was 100 μs resulting in a 19 voxel particle displacement between frames in the free stream.

The second modification involves the increase of the light scattered by the 1.5 μm oil particles by adding two coated and highly reflective dielectric mirrors to the laser optics,

which reflect the light back and forth through the test section (see sketch in figure 9.1-left) effectively increasing the laser pulse energy from 8 mJ to an equivalent of 60 mJ. The specific illumination arrangement has the additional advantage that all viewing directions collect scattered light both in forward and backward direction. The mirrors are placed on both spanwise sides outside the free stream as not to disturb the flow. Optimization of the particle illumination is crucial under the present conditions, since laser power and camera sensitivity are limited while the illuminated region is thick. The lower limit of the illuminated volume was realized by the lower mirror edge parallel to the flat plate at $y = 1$ mm. For a straight upper cut of the light volume a knife-edge filter was mounted in front of one of the dielectric mirrors parallel to the wall at $y = 10$ mm. The flow was seeded to an image concentration of approximately 0.06 particles per pixel.

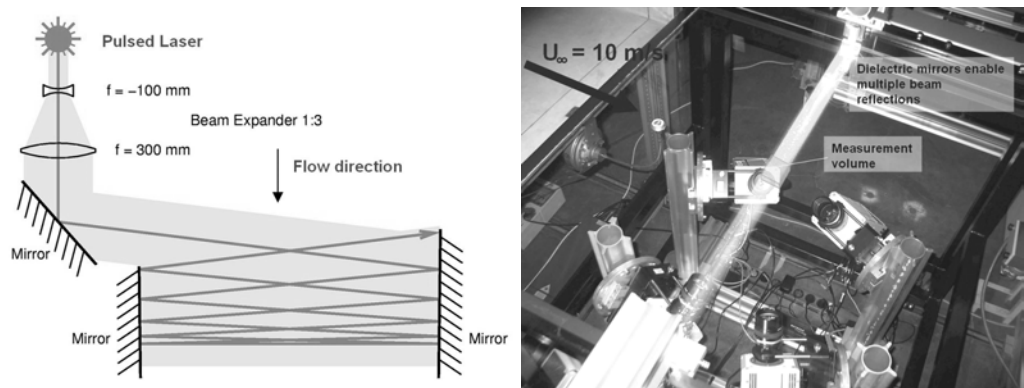


Figure 9.1: Sketch of the optical setup which enables the optimal usage of the laser pulse energy for illumination of the PIV measurement volume (left). Experimental arrangement (right). The 4 high-speed cameras are located underneath the glass plate with the measurement volume above the plate. (Schröder et al 2006, 2008)

The camera system was calibrated by recording images of a 3D-calibration target at three positions separated by 3 mm in depth. A linear translation stage with stepper motor has been used in order to ensure high accuracy of the several target positions in the wall-normal (y) direction. The self-calibration procedure outlined in section 3.4 was applied to evaluate the accuracy of the calibration a posteriori, but was not used to correct the original calibration. It was found that deviations of the calibration function were of the order of 0.2 pixels.

The particle image recordings require pre-processing in order to eliminate background illumination, reduce local inhomogeneities of light intensities (stripes) caused by the specific illumination technique and noise reduction. Sliding minimum subtraction and a Gaussian smoothing of the particle images are the applied operations. Then the volume intensity distribution is reconstructed at a resolution of 19 voxels/mm using the MART algorithm with 5 iterations.

The reconstructed intensity distribution in the volume has been analyzed with an iterative multi-grid volume deformation scheme reaching a final 48^3 voxels ($2 \times 2 \times 2$ mm³) interrogation box size with 75% overlap yielding the instantaneous three-dimensional velocity volume over a grid of $51 \times 12 \times 61$ in streamwise, wall-normal and spanwise direction. The number of spurious vectors based on the normalized median test (Westerweel

and Scarano 2005) was less than 3%. For the instantaneous velocity vector an uncertainty of about 4 % is estimated, which corresponds to a sub-pixel accuracy of the cross-correlation peak detection of 0.2 pixels. Finally a time series containing 1024 vector volumes was thus obtained.

9.3 Results

A typical example of the time evolution of vortex structures (green) and instantaneous Reynolds shear stress related to sweep ($u' > 0$ and $v' < 0$, magenta) and ejection ($u' < 0$ and $v' > 0$, blue) events is presented in figure 9.2. The time increment between consecutive volumes is 0.67 ms, in which the flow structures have convected by about 6 mm in x -direction. Note that in the plot and throughout this section dimensional time and space coordinates are used, because of the relative large uncertainty in the estimated boundary layer thickness. The returned vortex structures are mainly of arch/cane type or part of a hairpin neck in case the head extends beyond the height of the measurement volume. Moreover packets of, mostly two, streamwise aligned hairpins structures are observed frequently, see for example structure *A* in the right column of figure 9.2. From the time evolution of packet *A* it is seen that the basic shape of the vortices does not change significantly as they convect through the measurement volume. This also holds for the vast majority of structures in figure 9.2 and for the complete dataset in general. The two arches in packet *A* appear to have merged in the second plot from the top, but this must be interpreted as an artifact of the present visualization, because inside this blob still two arches are present only at slightly higher values of Q . As already stated in section 8.3.3 sweeps are found outboard of the hairpin type vortices and ejections occur below and upstream of the hairpin head and in between its necks.

The long temporal coherence of the above structures relative to the observation time can be explained by considering the time-scale for viscous diffusion T_{diff} , which may be estimated as:

$$T_{diff} = \frac{L^2}{\nu} \quad (9.1)$$

where L is the characteristic length representing the vortex core diameter and ν is the kinematic viscosity. For the present conditions $T_{diff} = 67$ ms assuming $L = 1$ mm, which is the smallest detectable core (as may be seen from figure 9.7 and 9.8). This shows that the decay of these vortex structures through diffusion extends beyond the observation time (3 ms). It should be noted that the smaller (Kolmogorov) scale structures, which are beyond the present spatial resolution, will decay by viscous diffusion at much faster rates, as can be seen from Eq. 9.1.

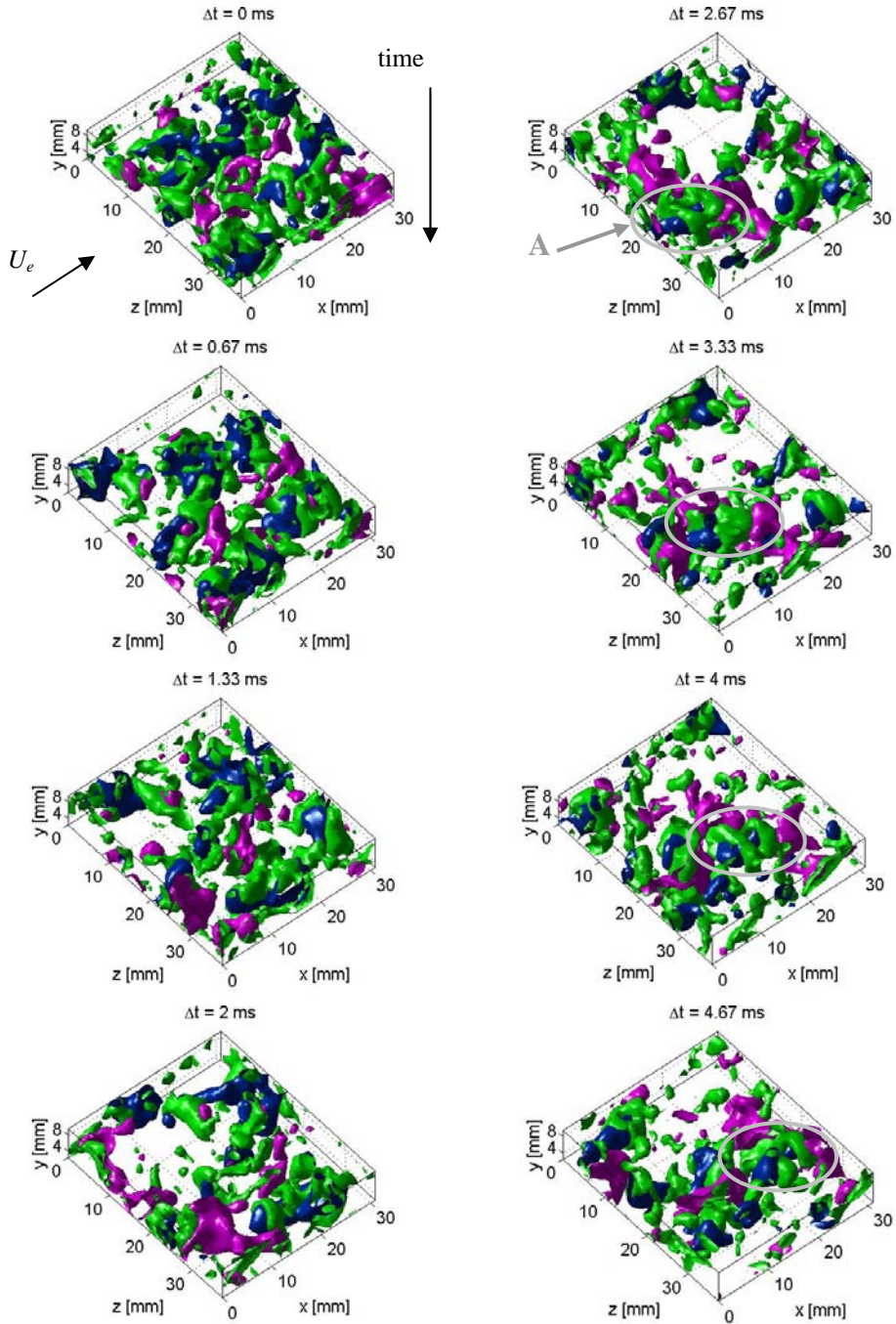


Figure 9.2: Time series showing evolution of vortical motion and ejection and sweep events. Q-criterion (green) isosurface value $1.5 \cdot 10^4 \text{ s}^{-2}$. Q2 (blue) and Q4 (magenta) event isosurface value -0.1 (m/s)^2 .

Additionally, a time scale for vorticity, hence vortex, deformation T_{deform} by velocity gradients may be defined as:

$$T_{deform} = \frac{L}{\Delta U} \quad (9.2)$$

where ΔU is a characteristic velocity difference. In case deformation is caused by the interaction of high and low speed zones, for which may be assumed $\Delta U = 0.1U_e = 1$ m/s, the related time scale is $T_{deform} = 1$ ms. When it occurs, this process may be observed in the present data up to the point where the dimensions of the structure decrease to below the spatial resolution.

9.3.1

Life

The motion (life) of hairpin structures is dominated by convection and simple growth, as shown above. Therefore the growth and convection rates of these hairpins will be discussed here first, before moving to more dynamic and less-frequent events such as the birth and death of these structures. The growth rates will be established below using conditional averaging and feature tracking approaches.

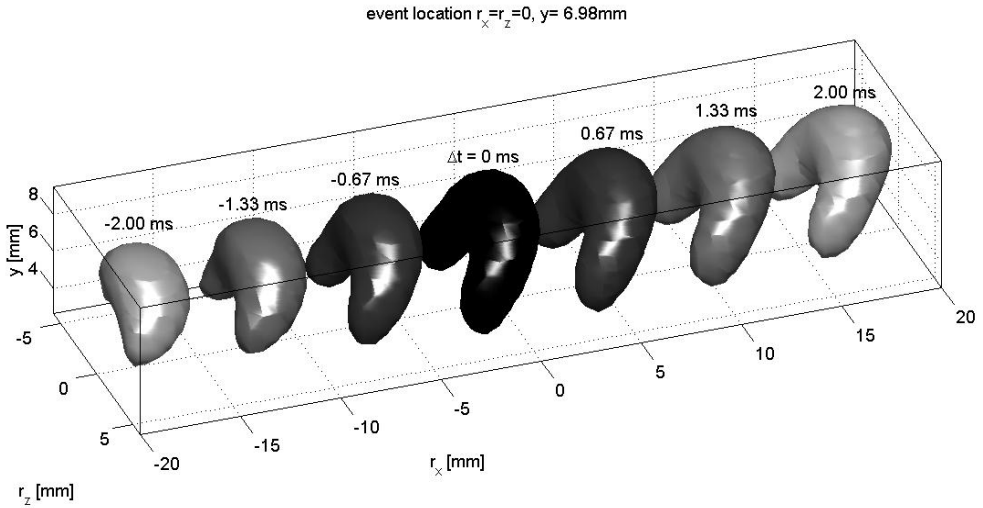


Figure 9.3: Conditional eddies given a negative spanwise swirling event at $y = 6.98$ mm for different time shifts Δt . Vortical motion is visualized using the Q vortex detection criterion with the same iso-surface level for all cases.

The conditional eddy is determined as before in section 8.3.1 using linear stochastic estimation with negative spanwise swirling motion as the specified event. For the present case the event is located at $y = 6.98$ mm distance from the wall at reference t_{ref} , which can be cross-correlated (according to Eq. 7.10) either with the velocity distribution at the same time instant ($\Delta t = 0$) or with the distribution shifted in time by Δt . The former may be interpreted as the average flow field associated with the spanwise swirling event and the latter as the evolution of that flow field in time. The conditional eddy for $\Delta t = 0$ (figure 9.3) shows a hairpin vortex similar to the one of figure 8.5. The shape of the conditional eddy is maintained when the time shift Δt is increased, which again is evidence that hairpins predominantly convect without deforming significantly over at least 2 ms. After approximately 2 ms the hairpin structures have traveled through the complete measurement volume, so no conclusion can be reached on the typical life time of the hairpins based on the present data. Interestingly for negative Δt the strength of the neck of the conditional eddy is reduced, which causes them to disappear over time in figure 9.3 with only the head remaining. A simple explanation for this phenomenon can be that the neck loses correlation with the specified event quicker for negative Δt , because of the larger distance to the event compared to the equivalent case with positive Δt . This is the result of the neck being located upstream of the head (inclined at approximately 45 degrees with the wall).

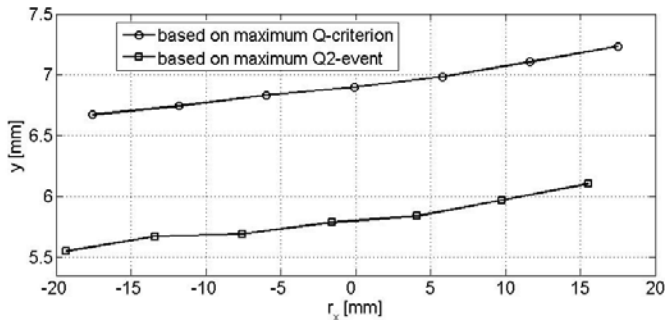


Figure 9.4: Growth rate of the Q-criterion and Q2-event maxima in conditional averages of figure 9.3.

To quantify the growth in size with time, the locations of the Q -maximum in the conditional eddies are plotted in figure 9.4. The maximum is found in the heads at $r_z = 0$ and its precise location is determined with sub-grid accuracy by fitting a 3D Gaussian through the neighborhood of the peak, where the maximum of the fitted function is taken as the final peak position. As seen from the figure, the distance from the wall of the hairpin head increases linearly with time over the range considered. The line is inclined at approximately 0.91 degrees with the wall in the x,y plane. Based on the same plot the convective and growth velocity are determined at 8.8 m/s in x -direction and 0.14 m/s in y -direction respectively. Identical results are found by tracking the maximum instantaneous Reynolds shear stress related to an ejection (Q2) event (figure 9.4). Even though the results presented here are for a 7 mm high hairpin, similar low growth rates have been observed between 5 and 9 mm distance from the wall. Finally, the increase in width of the conditional eddies is

much smaller than the increase in height as may be expected from the results in section 8.3.1 (eq. 8.1) and could not be determined with sufficient accuracy.

The second approach to establish the growth rate is based on detection and tracking of individual hairpin heads, which gives not only their average path but also standard deviations. In the first step the heads in each volume are detected using pattern recognition by cross-correlation with a template, for which the conditional eddy in figure 9.3 ($\Delta t = 0$) is chosen. The correlated quantity is the negative spanwise swirl, and a head is said to be detected when the cross-correlation coefficient exceeds 0.5. The head, i.e. negative spanwise swirl, of the conditional average is slightly elongated in the spanwise direction resulting in a larger uncertainty on the position of the heads in that direction. In the second step the detected heads in subsequent volumes are linked to produce tracks. A link is established with the head closest to the estimated position at the next time instant, which is determined using the average convective velocity. The track ends if no head can be found within the predefined search radius (2.5 mm).

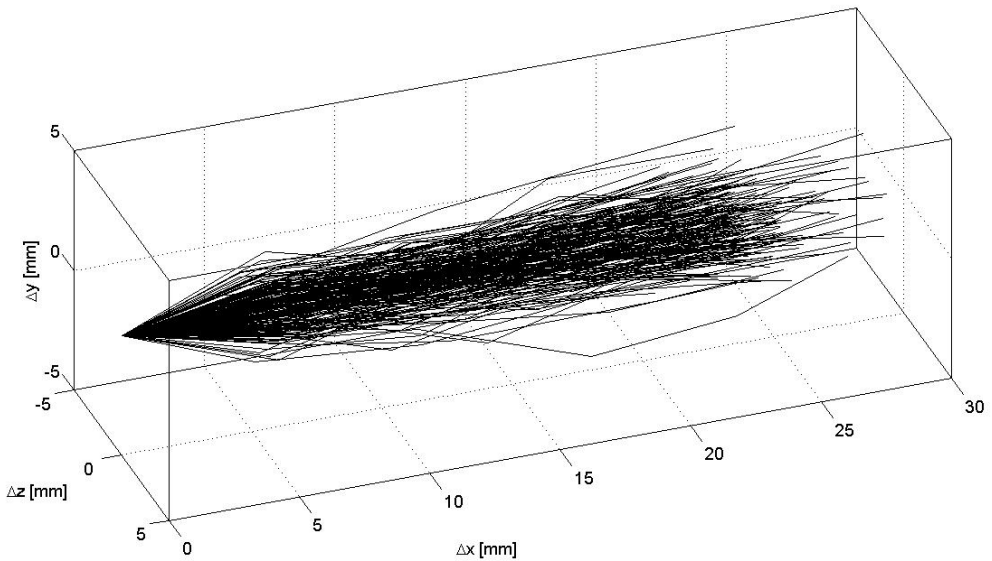


Figure 9.5: Negative spanwise swirl-event tracks (192 tracks extending over 5 or more time steps). Coordinate system is taken relative to initial position.

The resulting hairpin-head paths relative to the initial position ($\Delta t = 0$) are presented in figure 9.5, where only tracks have been considered that extend over at least 5 time steps, have an average distance to the wall between 4 and 6 mm and go through the center 27 mm of the measurement volume in spanwise direction. The tracks reveal a slowly increasing distance from the wall (growth), as expected. The relatively large scatter around the average track also increases over time. To better visualize the data, scatter plots of the relative position in the y,z plane in time are produced (figure 9.6). The mean position in each plane (time instant) is marked by a cross, while the standard deviation in y and z are represented

by the axes of the ellipse. The mean y -position is found to decrease from time $\Delta t = 0.67$ ms to 1.33 ms then to increase again to 0.24 mm at $\Delta t = 2.67$ ms. Below $\Delta t = 1.33$ ms the scatter in the data is much larger than the average displacement in y -direction resulting in low accuracy of the average. The growth rate is therefore based on average position at $\Delta t = 2.67$ ms returning 0.60 degrees, which is of the same order as the 0.91 degrees observed in the conditional averages (figure 9.4). Possible explanations for the difference between the methods may be the reduced accuracy of the average track resulting from the large scatter in the individual tracks and the fact that the conditional average is based on correlation, which includes a weighting of the individual vortices by their strength unlike the tracking procedure. Therefore the conditional average is biased towards the stronger vortices. Finally, the standard deviation increases uniformly, but it is not proportional to time Δt as expected, which must be ascribed to the finite accuracy of the detection and tracking procedure.

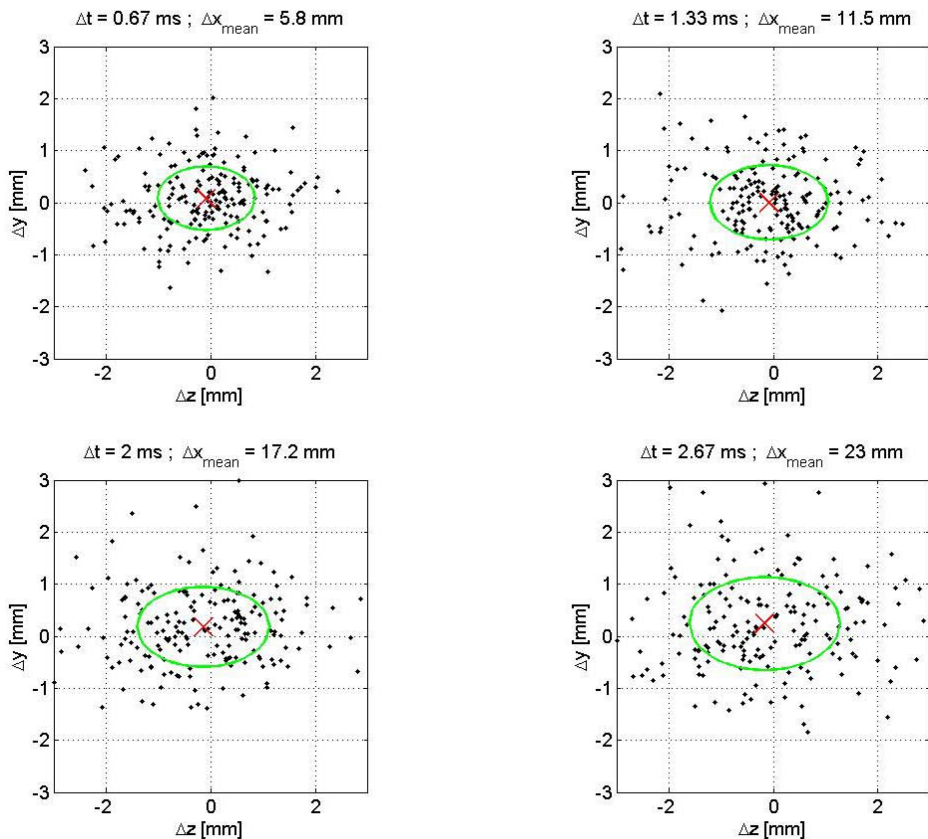


Figure 9.6: Scatter plot of the negative spanwise swirl tracks showing the relative y,z position in time. The mean position and standard deviation are indicated by the cross and the ellipse respectively.

9.3.2

Birth

Hairpin birth has been observed in approximately 3% of the snapshots based on the visual inspection of the first 200 volumes in the present dataset. Here a single example is given as an illustration of a possible mechanism for the creation of new hairpins. Other mechanisms may include splitting from an existing hairpin vortex, which has not been considered here.

Figure 9.7 shows a time series leading to the birth of a vortex with corresponding vector plots, in which the new hairpin is indicated by an arrow. The vortices, ejection and sweep events are color coded green, blue and magenta as before and the vectors shown are relative to convective velocity of 8.9 m/s. The sequence of events starts with a hairpin (labeled *A* in the top left volume) with an upstream low speed zone (as seen in top right vector plot). This low speed zone is approximately 6 mm high and 4 mm wide and is separated from the incoming high speed fluid by a shear layer. From the first to the second snapshot at $\Delta t = 0.67$ ms, the interface between the high and low speed fluid is observed to incline creating a sort of front, marked *B*. Furthermore the velocity in the low speed zone is reduced. Then the shear layer over the low speed zone starts to roll up in the last two snapshots, which is most clearly seen in the vector plots at $y = 7$ mm. A similar roll up is found at the side of the low speed zone (at $z = 14$ mm) resulting in the formation of a cane vortex (figure 9.7 bottom-left). The width and height of the new cane is approximately equal to the dimensions of the initial low speed zone (4 by 6 mm).

It remains uncertain if the presented sequence of events represents the dominant mechanism for hairpin vortex formation. However, it provides additional support to the observations by Zhou et al. (1999) and Schröder et al. (2006) who report formation upstream of an existing hairpin in numerical simulations and Tomographic-PIV experiments respectively. Moreover, the present results do indicate that hairpins can be generated away from the wall, in the present case at approximately $y/\delta = 0.4$, and do not necessarily need to grow starting from the wall. Furthermore an extended low speed zone seems to be a prerequisite for vortex formation, but unfortunately the present results do not reveal how it is formed upstream of a hairpin. Answering this question and describing the full chain of events requires following the structures over longer periods of time, even though the final roll up of the shear layer seems to be rather quick (within 1 ms).

9.3.3

Death

The death of a hairpin vortex, like birth, is a rare event also observed in approximately 3% of the volumes. Again a single typical example is presented here and the disappearance of individual hairpins through merging is not considered.

Figure 9.8 shows a time series leading to the death of a vortex, indicated by the arrow, with corresponding vector plots. The first snapshot shows the hairpin surrounded by two sweep events, labeled *A* and *B*, on either side in spanwise direction. The sweeps, most likely, are related to large hairpins further from the wall. A clear indication of a hairpin neck (green) associated to sweep event *B* is found in the second snapshot ($\Delta t = 0.67$ ms) at $z = 20$ mm. From the first to the second snapshot the necks of the dying hairpin reduce in strength, resulting in a reduced size of the ejection event induced by the hairpin. This can also be seen in the corresponding vector plot. The hairpin necks are deformed or stretched by the action of the sweep events and related high speed zones. Stretching will reduce the

width of the vortex and increase vorticity at first, which increases viscous diffusion leading to a final reduction of vorticity. Subsequently from the second to the third snapshot ($\Delta t = 1.33$ ms) the hairpin is further accelerated and loses its identity, i.e. the necks disappear. The remaining hairpin head is still visible in the vector plot, however, the low speed zone underneath is not present any longer. Furthermore the vectors reveal a source topology at location C with outflow also in spanwise direction (not shown), which creates unphysical 3D divergence at that location. Divergence indicates failure of the measurement to resolve the flow scales, hence reveals the presence of important small-scale motion. As to the nature of this motion, it is speculated that a small ejection of near wall fluid penetrates into the outer part of the boundary layer. Such ejections or eruptions have been observed by Corino and Brodkey (1969) and are explained by Smith et al (1991) as occurring after the viscous flow near the wall is exposed to a pressure field associated with a vortex for a period of time. Finally from the third to the last snapshot, the source C disappears and the remaining vortex head reduces slowly in strength. It is interesting to note that the hairpin 7 mm downstream of the one discussed above also seems to reduce in strength. When the two hairpins can be considered a packet, this means complete packets can disappear at once.

The presented result seems to indicate that hairpin death is rather sudden. Especially from step two to three in the above, the time and spatial resolution is insufficient to describe the full chain of events and the origin of structure C , as well as the interaction with near wall fluid.

9.4 Conclusions

The tomographic PIV technique has been applied to nearly time resolved PIV recordings for the study of the development of hairpin vortices within a tripped turbulent flat plate boundary layer flow with $U_e = 10$ m/s. The experiments are performed around $Re_x^{1/2} = 630$ in a low speed wind-tunnel using a diode-pumped laser and four high speed CMOS cameras operating at 1.5 kHz (double frame). The measurement volume is $34 \times 9 \times 40$ mm³ in streamwise (x), wall-normal (y) and spanwise (z) direction, in which $51 \times 12 \times 61$ velocity vectors are returned. Its illumination required a multiple-reflection system able to increase the light intensity within the volume. This aspect is deemed essential when a high-speed tomographic PIV system is applied in air flows. The results demonstrate that the technique yields 4D, space-time, capabilities and can be extended to fully time resolved measurements in air flow when the repetition rates of the cameras and laser permit.

Hairpin vortices and packets consisting of 2 streamwise aligned hairpin vortices are observed frequently in the vector volumes. Moreover ejection and sweep are found at the positions relative to hairpin as expected and discussed in chapter 8. Time sequences show that convection of the hairpin structures dominates, and that the structures are captured 4 to 5 times before leaving volume. Their growth and convection rate have been established using conditional averaging (space-time correlations) and tracking of individual hairpin heads. It is found that the height of hairpin, as defined by the distance of head from the wall, grow along average paths inclined at 0.60 to 0.90 degrees with the wall and convect at approximately 8.8 m/s in streamwise direction for hairpin heights around 7 mm (0.5δ).

Formation of a new hairpin (birth) and termination of a hairpin (death) are rare events observed in approximately 3% of the volumes. For both cases an example from the present dataset has been presented. The first example showed the birth of a hairpin as the roll-up of the shear layer over a low speed zone at 7 mm distance from the wall. This observation demonstrates that vortices can be formed away from the wall and do not need to grow from

the wall up. However, it does not exclude that the majority of hairpins is still formed in the near-wall region. The example of hairpin death showed a rapid deformation with decay of the hairpin necks under the action of large sweep events induced by larger hairpins. The necks then disappeared with only the head remaining, which decreased much more slowly in strength. Furthermore, both the roll-up of the shear layer during birth and the deformation of the hairpin neck during death happened so fast that they could not be resolved by the present measurement system.

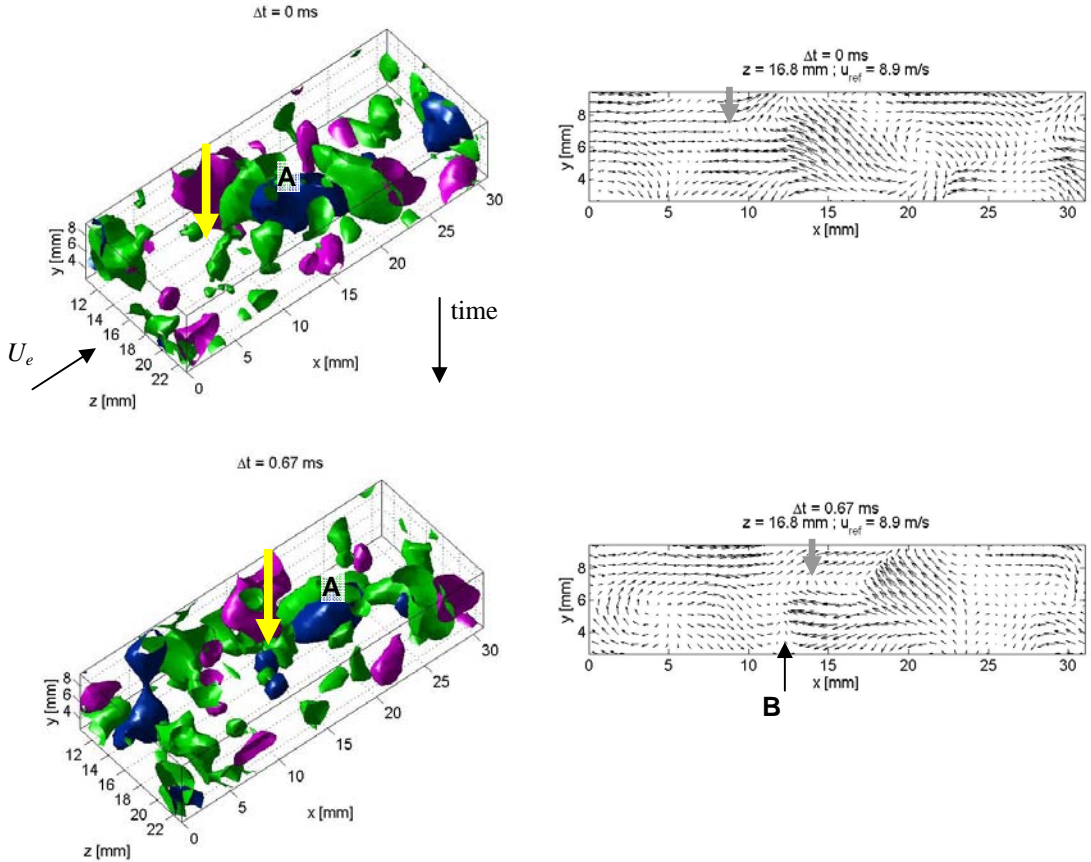


Figure 9.7: Time series showing the birth of a vortical structure. Isosurfaces (left) as in figure 9.2 and velocity vectors with respect to the average velocity (right).

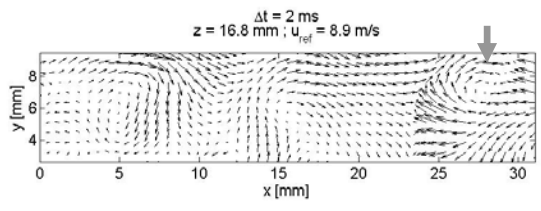
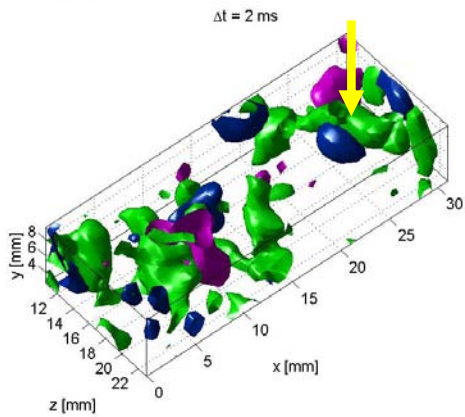
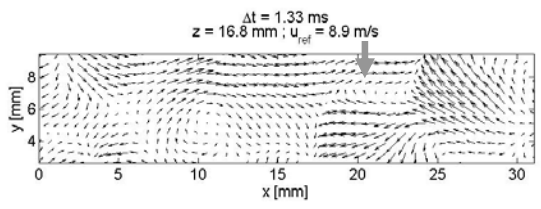
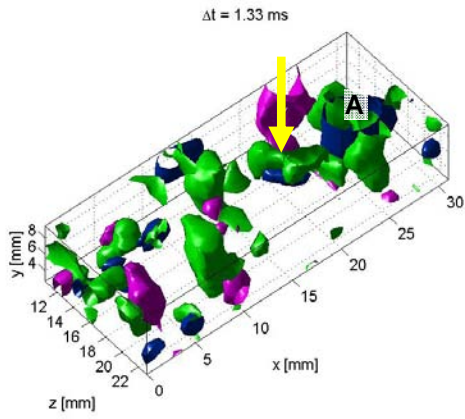


Figure 9.7 continued.

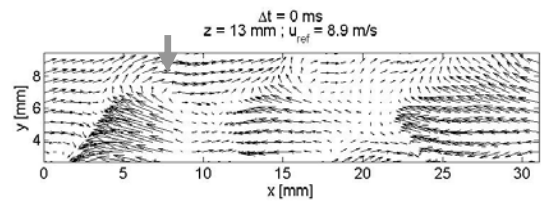
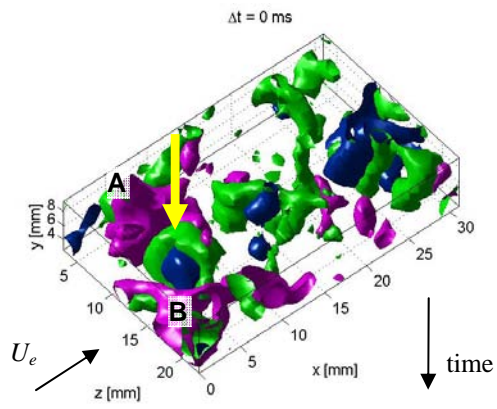


Figure 9.8: Time series showing the death of a vortical structure. Isosurfaces (left) as in figure 9.2 and velocity vectors with respect to the average velocity (right).

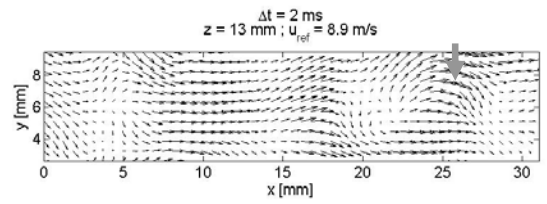
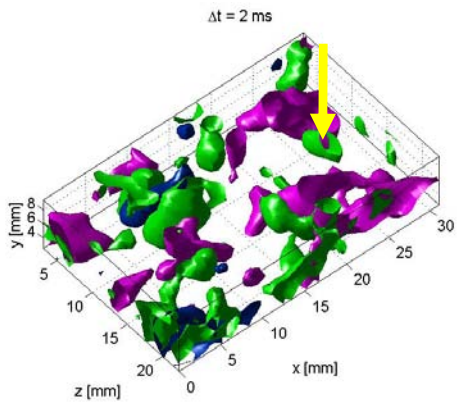
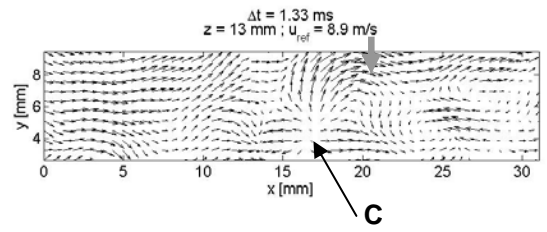
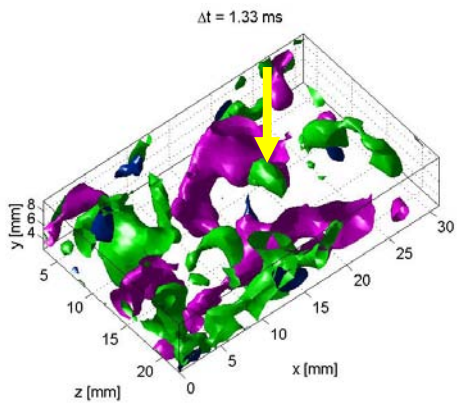
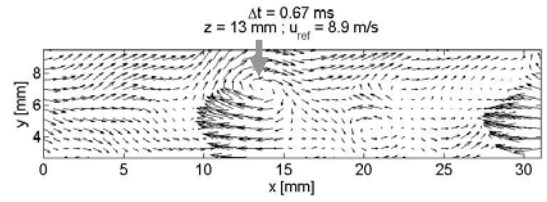
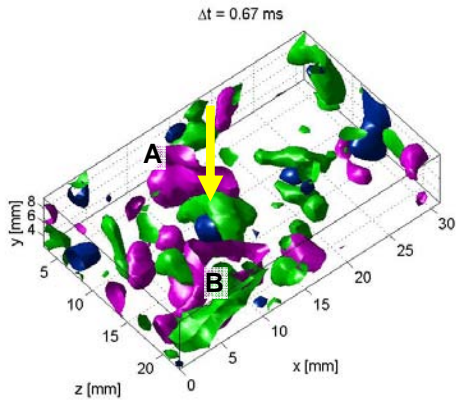


Figure 9.8 continued.

Chapter 10

Supersonic turbulent boundary layer ($Re_\theta = 34,000$, $M = 2.1$)

Tomographic-PIV was used to quantitatively visualize the 3D coherent structures in a Mach 2 supersonic turbulent boundary layer between $y/\delta = 0.15$ and 0.47 . The Reynolds number based on momentum thickness $Re_\theta = 34,000$. The instantaneous velocity fields show hairpin vortices aligned in streamwise direction forming very long zones of low-speed fluid. The observed hairpin structure is also a statistically relevant structure as is shown by the conditional average flow field associated to spanwise swirling motion. Low-pass filtering of the velocity field reveals streamwise vortices and signatures of large-scale hairpins (height $>0.5\delta$), which are weaker than the smaller-scale hairpins in the unfiltered velocity field. The large-scale hairpin structures in the instantaneous velocity fields are observed to be aligned in streamwise direction and along diagonal lines. Additionally the autocorrelation function of wall-normal swirling motion representing the large-scale hairpin structure returns positive correlation peaks in streamwise direction (at 1.5δ distance from the DC peak) and along the 45-degree diagonals, which also suggest a periodic arrangement in those directions. It is conjectured that the smaller-scale hairpins are formed on the low-speed zone associated to the leg and neck of a large-scale hairpin.

10.1

Introduction

Recent PIV studies of wall-bounded turbulent flows have shown that within the outer layer hairpin vortices are organized into packets (Adrian et al. 2000, Christensen and Adrian 2001), which can be thought of as a streamwise train of hairpins. Not only do these packets occur frequently, they also contribute significantly to the Reynolds shear stress (Ganapathisubramani et al. 2003). These reports were followed by PIV and hot-wire observations of even larger-scale motions ranging up to 40δ in streamwise direction (e.g. Kim and Adrian 1999, Hutchins and Marusic 2007, Ganapathisubramani et al. 2007). It has been conjectured that the elongated structures result from streamwise aligned hairpin packets based on their signatures in the 1D hot-wire signal.

The aim of the present study is to investigate the 3D spatial organization of hairpins, packets and the large-scale (vortex) structures. For this purpose the three dimensional velocity distribution in a supersonic turbulent boundary layer at $Re_\theta = 34,000$ is measured using Tomographic-PIV. At this high Reynolds number the packets are longer in streamwise direction, which is beneficial to the experimental investigation as they are detected more easily, while furthermore a large range of scales is expected. The experiments also serve to demonstrate that the Tomographic-PIV technique can be applied successfully in high-speed wind tunnel facilities.

Although the flow is supersonic, the Reynolds number is deemed to be the only dimensionless number relevant for the turbulence structure. Direct compressibility effects

are expected not to be important, as the fluctuating Mach number is less than 0.2 (Spina et al. 1994). Moreover the velocity average and fluctuation profiles collapse onto the incompressible profile when the variation of the fluid properties (i.e. temperature and density) across the boundary layer is taken into account in the scaling (Smits and Dussauge 2006). Concerning the instantaneous flow structures, Rayleigh scattering and oil droplet visualizations at high Reynolds number, although not easy to interpret, again have suggested a strong similarity between the subsonic and supersonic case (Spina et al. 1991). Furthermore, at relatively low Reynolds number, DNS of supersonic boundary layers has shown hairpin and packets comparable to those found in subsonic boundary layers (Ringuette et al. 2007).

In the first part of this chapter the implementation of Tomographic-PIV in the supersonic wind tunnel will be discussed. Then instantaneous results are presented and evidence for the existence of hairpins and packets in the supersonic boundary layer is given. In the discussion (following Adrian et al. 2000) the term hairpin will be used to represent cane, hairpin, horseshoe and omega shaped vortices, which are believed to be variations of the same basic structure. Although the occurrence of hairpins in the supersonic boundary layer has been suggested previously on the basis of flow visualization, a direct observation in velocity measurements is lacking presently. Finally the large-scale vortical motions will be presented and the spatial organization of the large- and smaller-scale vortices will be discussed.

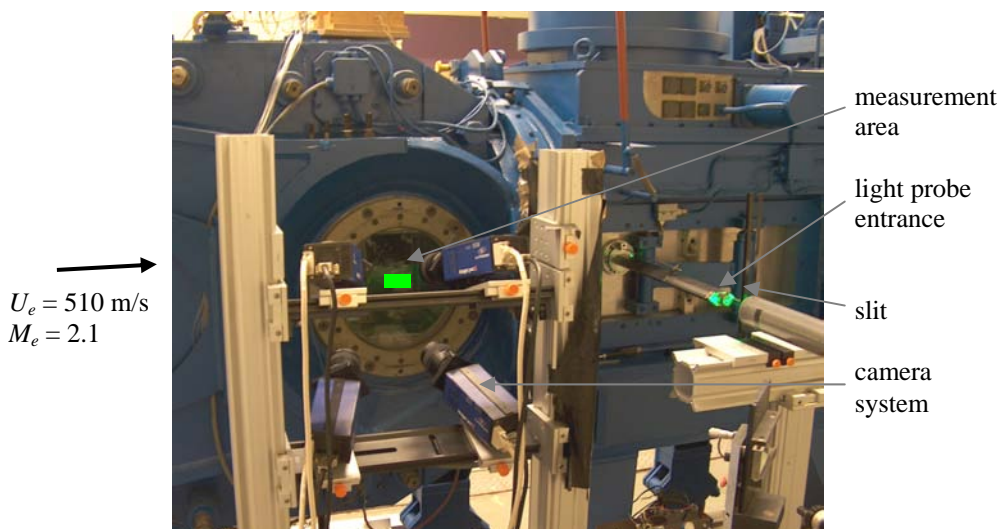


Figure 10.1: Optical arrangement at the TST-27 transonic/supersonic wind tunnel.

10.2 Experimental setup

The experiments have been performed in the transonic-supersonic wind tunnel TST-27 at Delft University of Technology, where the turbulent boundary layer over the tunnel side wall is measured at a free-stream velocity $U_e = 510$ m/s and Mach number $M_e = 2.1$. The flow in the boundary layer is optically accessible through the large optical window in this side wall. The boundary layer undergoes natural transition in the tunnel nozzle and develops

along the smooth flat tunnel wall over approximately 2m before reaching the 270×280 mm² test section. At the measurement location the boundary layer thickness δ_{99} and momentum thickness θ are 20 mm and 1.2 mm respectively (see table 10.1 and Humble et al. 2006, 2007 for more detail on the boundary layer statistical properties). The density variation necessary to calculate the momentum thickness was deduced from the measured velocity distribution using the adiabatic Crocco-Busemann relation with constant pressure and recovery factor ($r = 0.89$) across the boundary layer.

**Table 10.1. Supersonic turbulent boundary layer properties
(after Humble et al. 2006)**

U_e	510 m/s
M_e	2.1
δ_{99}	20 mm
δ^*	3.7 mm
θ	1.2 mm
$H = \delta^*/\theta$	3.1
u_τ	19.5 m/s
u_τ/ν_w	354 mm ⁻¹
δ^*	7080
c_f	1.65·10 ⁻³
Re_θ	34,000

The definition of the relevant Reynolds number is not trivial in the case of supersonic boundary layer flow, because of the significant temperature variations over the boundary layer height (Smits and Dussauge 2006). Perhaps the most commonly adopted is $Re_\theta = \rho_e U_e \theta / \mu_e$, which is based on the free-stream fluid properties. Alternatively, the Reynolds number can be based on the shear stress at the wall resulting in $Re_{\delta^*} = \rho_e U_e \theta / \mu_w$, where the subscripts e and w denote free-stream and wall conditions respectively. It is still unclear which of the two should be used for comparison with subsonic boundary layers, therefore both are given here: $Re_\theta = 34,000$ and $Re_{\delta^*} = 20,000$.

For the PIV measurements the flow is seeded with 240 nm TiO₂ particles to a particle image density of 0.05 particles per pixel, which is sufficiently low to yield an accurate particle reconstruction (chapter 5). The response frequency of these tracers is 420 kHz (section 6.1). The particles are illuminated by a Spectra-Physics 400 mJ double pulse Nd:Yag laser in a light ‘sheet’ that is oriented parallel to the wall and is expanded to 6.5 mm thickness in wall normal direction. The sheet formation optics are contained in the light probe located downstream of the test section (figure 10.1). Furthermore a slit is added to the light path to create a top-hat light intensity profile. Four high-resolution CCD cameras (LaVision Imager Pro X, 2048×2048 pixels, 14 bit) within a solid angle of approximately 30 degrees have been used to record the particle images (figure 10.1) with an average resolution of 23 pixels/mm. The lens $f_\#$ is set to 11 and 8.0 for the cameras in forward and backward scatter respectively. The time separation between subsequent exposures is set at 2 μs, which at the particular reconstruction settings yields a particle displacement of 20 voxels in the free stream. Both the light probe and camera system could be translated permitting to measure the velocity distribution at different heights in the boundary layer. However, the emphasis in

this chapter will be on the results for the laser sheet closest to the wall covering $3.0 < y < 9.5$ mm ($0.15 < y/\delta < 0.47$).

The camera system is calibrated by scanning a plate with 10×10 dots through the volume in steps of 4 mm in depth over a total range of 8 mm covering the light sheet. In each of the three calibration planes the relation between the physical coordinates and image coordinates is described by a 3rd order polynomial fit. Linear interpolation is used to find the corresponding image coordinates at intermediate depth positions. Then the volume self-calibration procedure described by Wieneke (2007, see also section 3.4) was used to improve the calibration accuracy. It was found that the triangulation disparity for one of the four cameras exceeded 0.4 pixels (approximately 1.2 pixels), which was corrected to less than 0.2 pixels for all cameras. The self-calibration correction was found to slightly increase the returned vorticity levels, but did not affect the appearance of the flow structures.

The intensity distribution in the volume is reconstructed from the recorded images using the MART algorithm with 5 iterations. The reconstructed volume dimensions in streamwise (x), wall-normal (y) and spanwise direction (z) are $70 \times 6.5 \times 35$ mm³, which is discretised at 20^3 voxels per mm³. In the cross-correlation analysis of the 3D reconstructed objects the interrogation box size is progressively decreased to 40^3 voxels resulting in approximately 24 tracers per box. The cross-correlation signal-to-noise ratio, defined as the ratio of the first and second correlation peak, is approximately 2.5. A 75% overlap factor is applied between neighboring boxes returning a vector spacing of 0.50 mm in each direction (corresponding to 177 viscous length scales based on the fluid properties at the wall) resulting in an overall measurement grid counting $142 \times 14 \times 77$ vectors. The complete dataset consists of 480 instantaneous 3D vector fields.

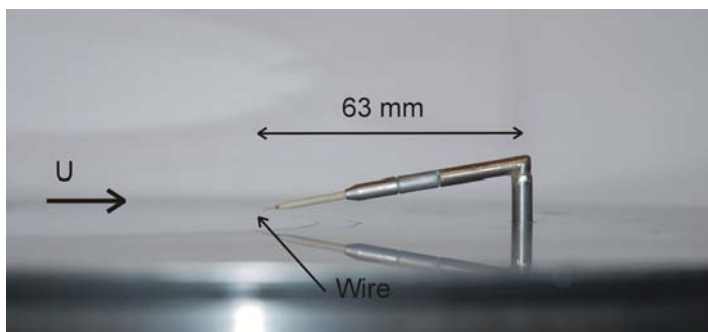


Figure 10.2: Hot-wire probe above the tunnel wall.

Additionally constant temperature hot-wire anemometry measurements have been performed to assess the large-scale-low-frequency motion in the boundary layer. The hot-wire system consists of a DISA 55M10 CTA bridge with a Dantec 55P11 single wire probe, which is made of 1.25 mm long and 5 μ m diameter tungsten wire. The equivalent wire length in viscous length scales is 443. The overheat ratio is set to 0.88, so that the hot-wire is mainly sensitive to momentum fluctuations $(\rho u)'$ and not so much to total temperature fluctuations (Smits et al. 1983). The wire response frequency is 50 kHz, however due to a tail in the response, the measured power spectrum is affected up to 20 kHz corresponding to a wavelength of 1.3δ using Taylor's hypothesis. The probe (figure 10.2) can be translated in

wall-normal direction to measure at different y/δ . The hot-wire system has been calibrated using the mean voltage at different heights in the boundary layer with the mass flow obtained from the measured velocity distribution by PIV in combination with the adiabatic Crocco-Busemann relation.

10.3 Results

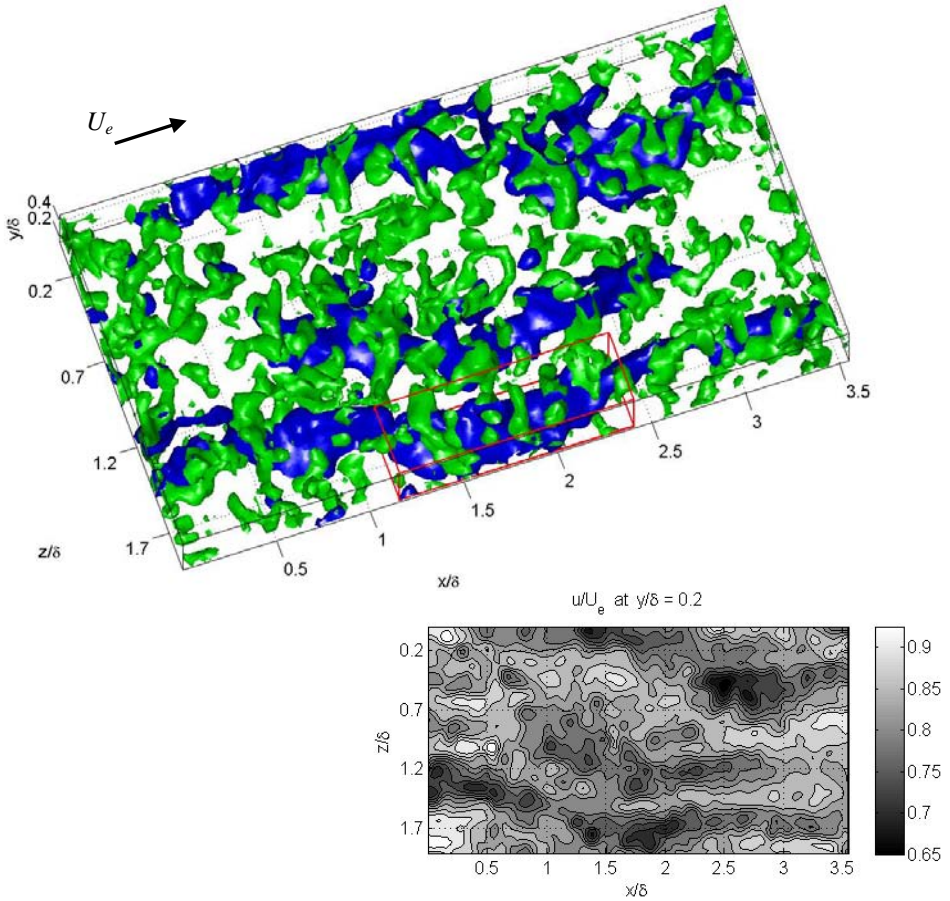


Figure 10.3: Instantaneous vortex distribution detected by the Q -criterion (green) and low speed zones (blue, $u < 0.80 \cdot U_e$) for $0.15 < y/\delta < 0.47$. The bottom-right inset shows a contour plot of the u -component of velocity.

10.3.1 *Instantaneous flow structure*

Figure 10.3 presents a typical example of the returned instantaneous flow field, where the x, y , and z axis correspond to the streamwise, wall-normal and spanwise direction

respectively. In the plot vortical motion (green) is visualized using the Q -criterion (the applied threshold is approximately $10^{-9} \left(\frac{\partial u}{\partial y} \right)_w^2$) and the zones of low velocity (blue) are

indicated by the iso-surface $u/U_e = 0.80$ corresponding to approximately 95% of the average velocity at this height in the boundary layer. Note that the visualization of the low speed zones is not very sensitive to the applied threshold, since they are separated from the higher velocity by regions of relatively high shear, as for instance can be seen in figure 10.3 bottom-right. The low speed zones are several boundary layer thicknesses long often extending beyond the measurement volume. Ganapathisubramani et al. (2007) even report lengths up to 40δ at $y/\delta = 0.2$ in their supersonic boundary layer based on high repetition rate PIV measurements and using Taylor's hypothesis. Long low speed zones have also been found in incompressible turbulent boundary layers using a single hot-film (Kim and Adrian 1999) or a spanwise array of 10 hot-wires to account for meandering of the low speed zones (Hutchins and Marusic 2007). The width of the low speed zones observed by visual inspection of the present results varies between 0.25δ and 0.4δ (see also Ganapathisubramani et al. 2006, Tomkins and Adrian 2003) and the spanwise spacing between low speed zones is between 0.5δ and 1.0δ .

At larger distances from the wall (figure 10.4) the low speed zones are observed to decrease in length, while their width remains approximately constant. These observations are in qualitative agreement with those in Ganapathisubramani et al. 2006, who report decreasing correlation lengths in streamwise direction with distance from the wall above $y/\delta = 0.16$ and an approximately constant correlation length in spanwise direction. Furthermore, near edge boundary layer ($y/\delta > 0.6$) the coherent structures, i.e. low speed zones and vortices, show intermittent behavior meaning that some snapshots contain only a couple of vortices while other snapshots appear similar to the example presented for $0.34 < y/\delta < 0.67$ (figure 10.4-top). Figure 10.4-bottom represents the intermediate case.

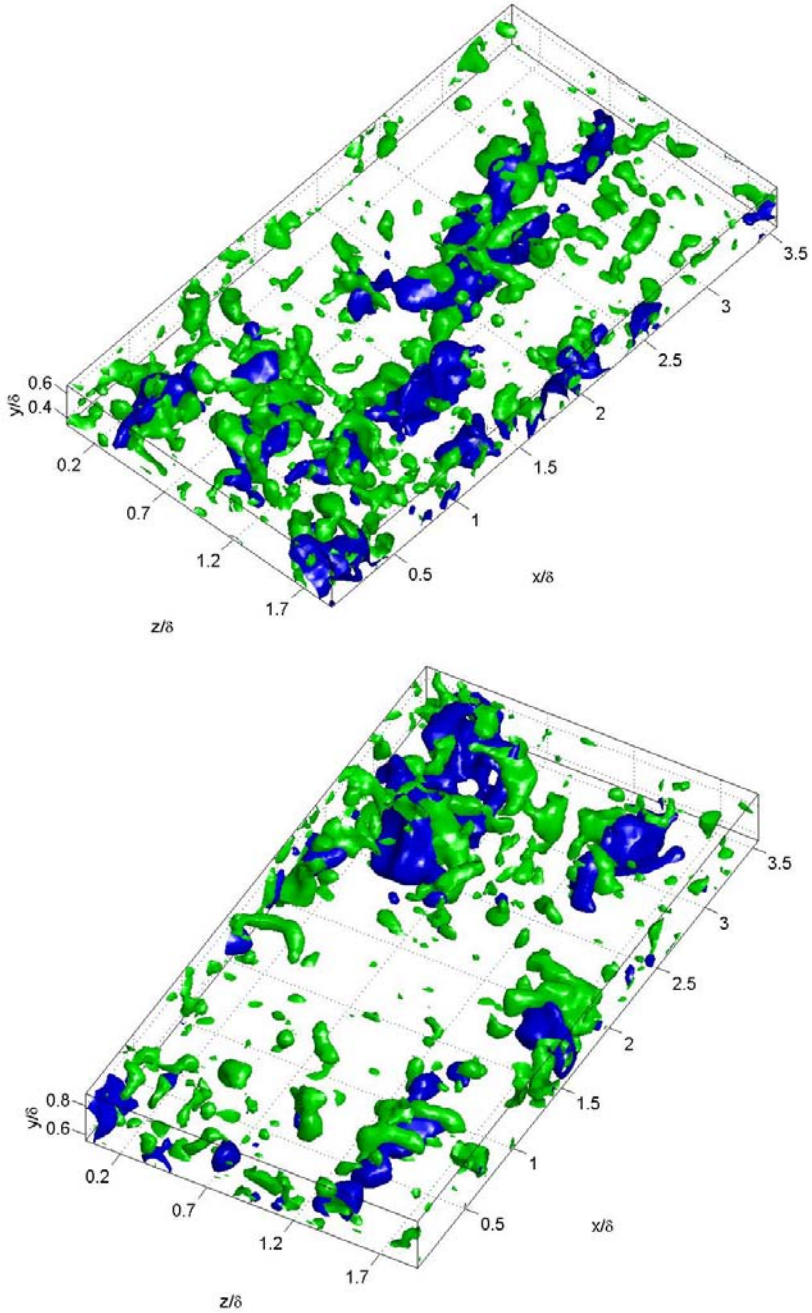


Figure 10.4: Instantaneous vortex distribution detected by the Q -criterion (green) and low speed zones (blue) for $0.34 < y/\delta < 0.67$ (top, blue $u < 0.89 \cdot U_e$) and $0.56 < y/\delta < 0.89$ (bottom, blue $u < 0.94 \cdot U_e$).

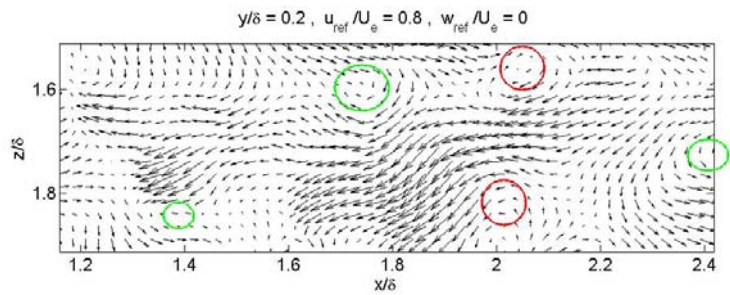
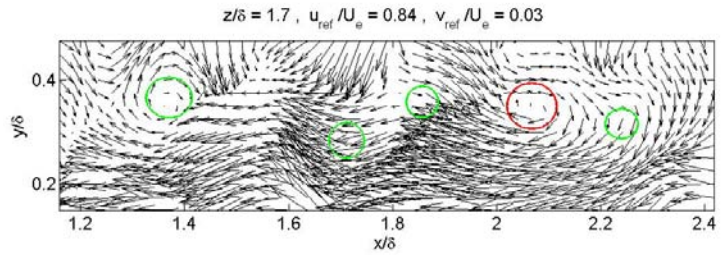
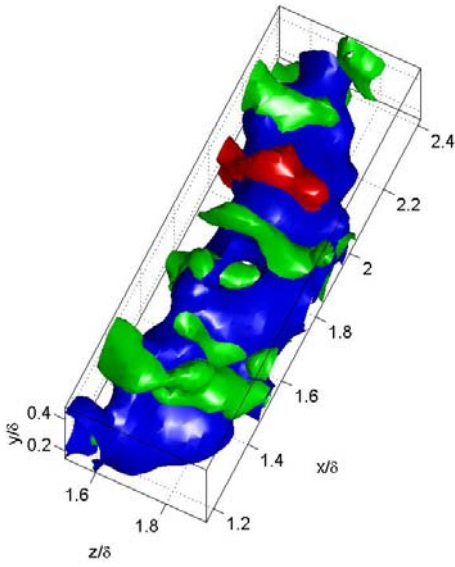


Figure 10.5: Arch vortices around a low speed zone in the sub-volume indicated in figure 10.3 (top-left) and corresponding vector plot in the x,y and x,z cross-sections (right). A detailed view of the vortex indicated in red is presented in figure 10.6. Other colors as in figure 10.3.

Plots of the complete measurement volume, such as figure 10.3 and 10.4, reveal that most of the vortical structures are found near the low speed zones. However at this scale of presentation the character of the individual vortices cannot be appreciated, therefore a detail taken from the volume of figure 10.3 is enlarged and shown in figure 10.5-top-left. Around the low speed zone a series of streamwise aligned hairpin (or arch) vortices are observed, which can be considered a hairpin packet (Adrian et al. 2000). The streamwise spacing of the vortices inside this packet is approximately 0.2δ . Figure 10.5-right presents the corresponding velocity vector field after subtraction of a convective velocity. The velocity distribution in the x,y plane (top diagram) shows swirling motion around the heads of the individual hairpins. For clarity the circles indicate the location of the vortices. It is also seen that the vortex heads convect with slightly different velocities, assuming the vortices travel with the average velocity inside the circle, which suggests that the vortices will interact or merge at a later stage. Furthermore, the vortices are of approximately the same size and do not appear to be aligned along a 12 to 20 degrees slope with the wall as in Head and Bandyopadhyay (1981) and Adrian et al. (2000). Near the top of the volume at $y/\delta = 0.45$ the velocity direction and magnitude is very irregular, which may indicate the presence of (vortical) flow structures just above this packet. Finally the distribution in the x,z plane (bottom diagram) shows swirling motion around the necks of the hairpins.

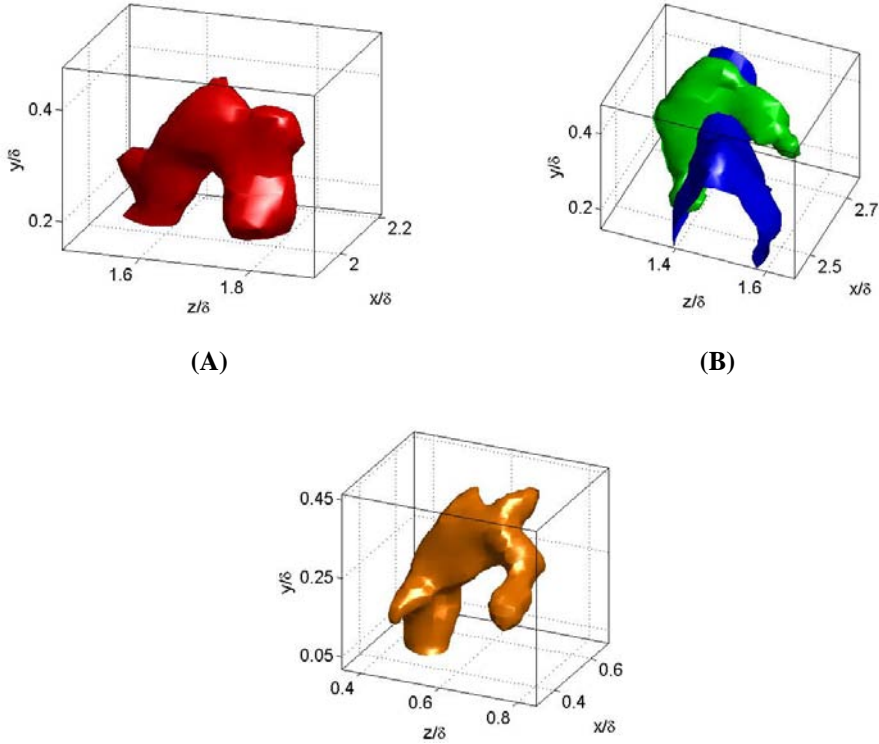
10.3.2

Hairpins

Two examples of individual hairpin vortex structures are shown in figure 10.6-A and B. The first one is the red colored vortex in the packet of figure 10.5 and has an asymmetrical arch shape. Its height and width are 0.33δ and 0.2δ respectively. The irregularities on the surface of this hairpin, i.e. the blobs attached to the arch, may be either due to measurement noise or due to smaller-scale motions near the arch that have not been resolved. It is well known that a local vortex detection scheme like the Q -criterion cannot distinguish between individual vortices in close proximity.

The second vortex (green, figure 10.6-B) is of a cane type and is also found near an extended low-speed zone (blue). It is slightly higher (0.4δ) compared to the previous example, but has approximately the same width (0.2δ). The width of both vortices corresponds to the width of the low-speed zones, as mentioned in section 10.3.1.

For comparison a hairpin structure returned by tomographic-PIV in an incompressible turbulent boundary layer at $Re_\theta = 1900$ (from Elsinga et al. 2007, chapter 8) is shown in figure 10.6-C. The shape is very similar to the hairpins found in the supersonic boundary layer, as is its size (height 0.35δ and width 0.25δ). It seems therefore that the asymmetric hairpin structure is a universal feature of the turbulent boundary layer above $y/\delta = 0.2$.



(C) $Re_\theta = 1900$ and $M_e \approx 0$

Figure 10.6: Individual vortices. *A*: arch extracted from the volume of figure 10.5. *B*: example of a cane vortex and low speed zone (color-coding as in figure 10.3). *C*: cane vortex observed in a low speed incompressible boundary layer (Elsinga et al. 2007, chapter 8 figure 8.3).

Additional evidence for the existence of hairpin vortices at the present Reynolds and Mach number is given by the conditional eddy obtained by linear stochastic estimation, which reveals an omega shaped hairpin (green, figure 10.7-left). The event used for the conditional average is the spanwise swirling strength $\lambda_{ci,z} \cdot \text{sign}(\omega_z)$ at $y/\delta = 0.35$ considering only negative values. As seen from figure 10.7 this event corresponds to a hairpin head at the specified location. The neck of the conditional eddy is at a 45-degree angle with the wall, as expected, and the eddy width is about 0.25δ consistent with the observed width of the instantaneous hairpins (figure 10.6) and the low speed zones. Underneath the eddy a 1.0δ long low speed zone ($u' < 0$, blue) ranging from $r_x/\delta = -0.4$ upstream of the hairpin to $r_x/\delta = 0.6$ downstream is observed, which may be considered short relative to the instantaneous low-speed zones (figure 10.3). The interface between the low speed zone and incoming high-speed fluid upstream of the eddy is inclined at approximately 25 degrees with the wall.

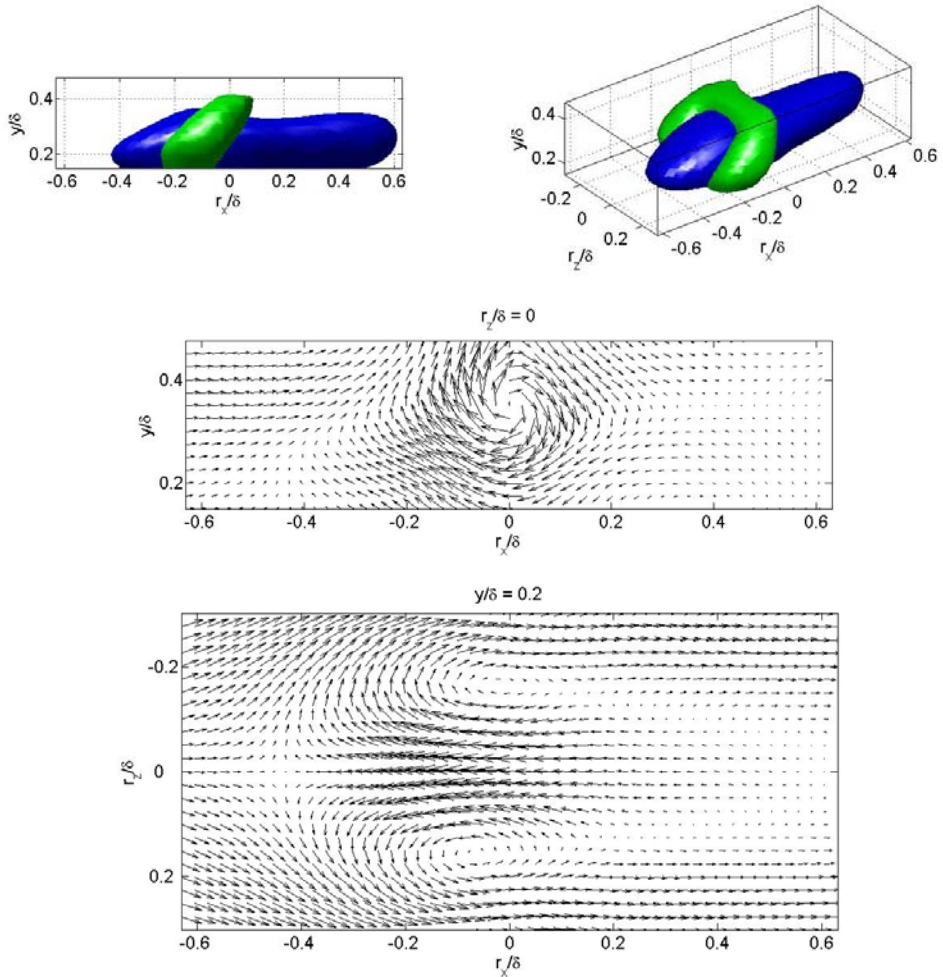


Figure 10.7: Conditional eddy (left) given a negative spanwise swirling event at $y/\delta = 0.35$ visualized using the Q vortex detection criterion (green) and low speed zones (blue, $u' < 0$) with corresponding velocity vector plot in the x,y and x,z cross-sections (right). The velocity vectors are relative to the local average velocity.

Figure 10.7-right presents the corresponding fluctuating velocity vectors in the x,y symmetry plane at $r_z = 0$ and the x,z plane parallel to the wall at $r_y/\delta = 0.2$. The vectors in the x,y plane show a shear layer upstream of the hairpin and a Q2 event ($u' < 0, v' > 0$) between the legs of the hairpin as expected. Furthermore the velocity vectors in the low speed zone downstream of the eddy $r_x/\delta > 0.2$ are small meaning that the velocity is close to the average value and that the downstream low speed zone is weakly related to the spanwise swirling event. The vectors in the x,z plane show a stagnation point in the symmetry plane at $r_x/\delta = -0.42$ and upstream high speed fluid flowing around the eddy.

Finally, conditional eddies were computed for negative spanwise swirl events at different distances from the wall. As it was found that the width and shape conditional eddy do not change significantly with height in this part of the boundary layer (well above the logarithmic layer), no further results of this will be shown here.

10.3.3

Large-scale and very large-scale motion

The pre-multiplied power spectrum is used to obtain the characteristic size of the large flow structures. In this representation the power spectrum for each velocity component $\Phi_{uu}(k)$, $\Phi_{vv}(k)$ and $\Phi_{ww}(k)$ is multiplied by the wavenumber k so that the area under the log-linear graphs of $k\Phi$ versus k corresponds to the kinetic energy for each velocity component. Hence the pre-multiplied power spectrum can be used to show the contributions of the different wavenumbers k , or alternatively wavelengths $\lambda = 2\pi/k$, to the kinetic energy. Figure 10.8 presents the pre-multiplied spectra for streamwise wavelengths λ_x and spanwise wavelengths λ_z in the present boundary layer at $y/\delta = 0.33$. In this figure the area under the plot is normalized, so only the relative contributions of the different wavelengths are shown. Furthermore wavelengths below three times the cross-correlation volume size are strongly affected by amplitude modulation due to insufficient spatial resolution; hence the data is unreliable for these wavelengths. They are, however, included in the plot (in gray) for completeness.

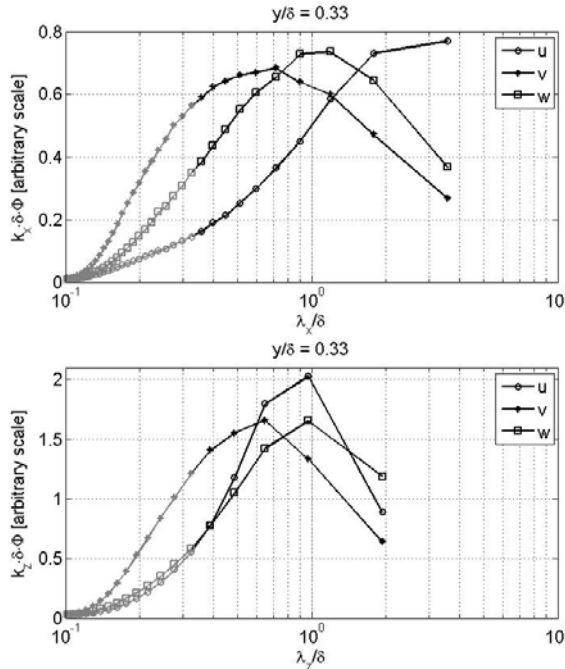


Figure 10.8: Pre-multiplied power spectra as a function of streamwise wavelength (top) and spanwise wavelength (bottom).

In the spanwise spectra (figure 10.8-bottom) a peak contribution is found between $\lambda_x/\delta=0.7$ and 1.0 for all velocity components, which is the wavelength associated to spanwise distribution of the low- and high-speed zones and their related (vortex) flow structures. In contrast the streamwise spectra (figure 10.8-top) show peaks at clearly different wavelengths for each velocity component. Most noticeably the u -component does not peak, but continues to increase beyond $\lambda_x/\delta=3$, which must be attributed to long streamwise lengths of the low- and high-speed zones extending beyond the measurement volume. The v -component of velocity returns a broad peak ranging from approximately $\lambda_x/\delta=0.4$ to 0.9. It is believed that the broad peak results from a combination of smaller wavelengths, say $\lambda_x/\delta=0.4$, related to the hairpins shown in section 5, and larger scales of the order $\lambda_x/\delta=1$. Finally the streamwise spectrum for the w -component has a more distinct maximum at $\lambda_x/\delta=1.2$.

To complete the pre-multiplied power spectrum for the u -component of velocity towards the larger streamwise length scales, hot-wire anemometry is used. The measured frequency information is converted to length scales by applying Taylor's hypothesis. Moreover, the effect of density variations across the boundary layer on the measured momentum fluctuations $(\rho u)'$ is removed from the data, to first order, by considering u^* , which is defined as:

$$u^* = \frac{(\rho u)'}{\bar{\rho}} \quad (10.1)$$

where $\bar{\rho}$ is the local average density obtained from the adiabatic Crocco-Busemann relation.

The resulting pre-multiplied power spectra are shown in figure 10.9 for several wall-normal coordinates y/δ . It is found that above $y/\delta=0.2$ all spectra show a peak around $\lambda_x/\delta=2$, which length scale is accessible within the present Tomographic-PIV measurement volume. Furthermore the energy contained in this length scale is approximately constant up to $y/\delta=0.7$, after which it decreases with distance from the wall. For $y/\delta=0.1$ a peak is observed near $\lambda_x/\delta=9$, which indicates the presence of very large scale motion at that height in the boundary layer (Kim and Adrian 1999). This scale is thought to be related to the long zones of uniform low or high momentum in the boundary layer, which actual length is underestimated by the hot-wire data due to meandering (Hutchins and Marusic 2007, Ganapathisubramani et al. 2007). The energy contained in the very large scales decreases with distance from the wall, so that they are visible only as a small bump near $\lambda_x/\delta=9$ in the power spectra up to $y/\delta=0.5$. This is in agreement with observations in section 10.3.1, where low speed zones extending beyond the measurement volume have been observed mainly below $y/\delta=0.5$. Finally below $\lambda_x/\delta=1.3$, the pre-multiplied power spectra are slightly affected by the response of the hot-wire. The data is, however, included in figure 10.9 in gray for completeness and to illustrate a trend.

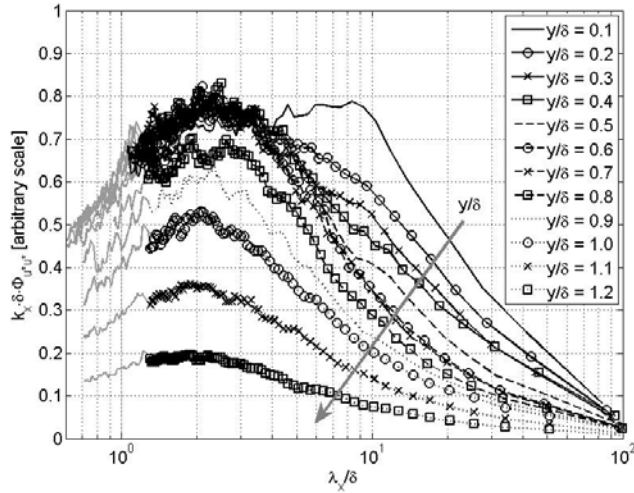


Figure 10.9: Pre-multiplied power spectra obtained by hot-wire anemometry as a function of streamwise wavelength.

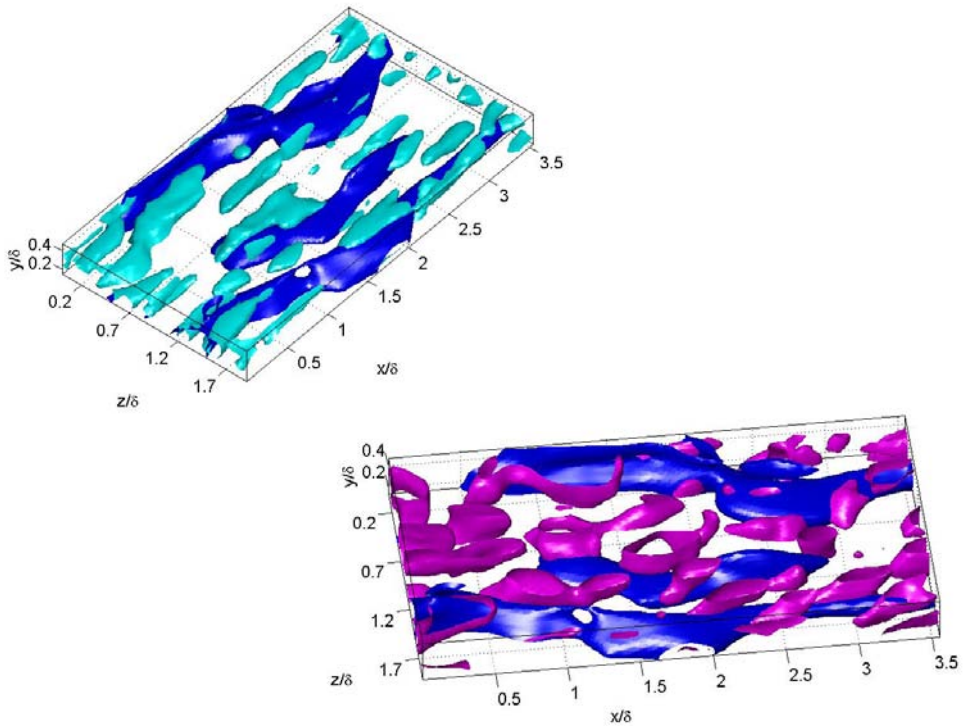


Figure 10.10: Streamwise (cyan, left), wall-normal swirling motion (magenta, right) and low speed zones (blue) in the low pass filtered velocity field of figure 10.3.

The second order regression of Eq. 7.8 (also known as Savitzky-Golay (1964) filter) is used to low-pass filter each velocity component with the purpose of bringing forward the large-scale flow structures in the Tomographic-PIV results. The second order polynomial is fit to the velocity in a volume measuring $0.78\delta \times 0.18\delta \times 0.28\delta$ in x, y and z direction. Because the regression is a non-linear filter, the modulation transfer function depends on the input signal and consequently there is no well-defined filter wavelength. However, the filter wavelength may be estimated as twice the fitted volume: $1.5\delta \times 0.35\delta \times 0.55\delta$. The filter wavelength in streamwise direction coincides with the peak in the pre-multiplied power spectrum $k_x \Phi_{ww}$, as shown above. Much longer vortical structures are not expected, because a coherent swirling motion always needs two velocity components at the same wavelength (e.g. ω_x is a function of v and w) and only the spectrum for u is seen to increase beyond $\lambda_x/\delta = 1.5$ while the other two drop off. The filter size in spanwise direction is chosen to match the width of the low-speed zones. Finally the filter wavelength in wall-normal direction is necessarily small to allow variation over the height of the measurement volume.

In the measurement volume closest to the wall, the low-pass filtered velocity fields return predominately streamwise and wall-normal vortices, which are visualized in figure 10.10 by the 2D swirling strengths $\lambda_{ci,x}$ and $\lambda_{ci,y}$ respectively. The strength of the vortices based on their peak Q -value is about 1/4 of the hairpins presented in section 10.3.2. It is seen in figure 10.10 that both type vortices occur next to low speed zones. Streamwise vortices are typically inclined at 5 degrees with the wall and are 0.8δ to 1.0δ long. Wall-normal vortices often occur in counter rotating pairs on opposite sides of the low speed zones, which is the typical hairpin signature in the x, z plane. Moreover streamwise vortices have been frequently observed to terminate in the wall-normal vortices, so that they may be considered as legs to cane or hairpin structures. It is important to note that applying the Q -criterion instead of the 2D swirling strength detects the same vortex structures but merged. Using Q , however, makes the interpretation of the visualizations more difficult.

Figure 10.11 presents the conditional eddy based on the wall-normal swirling strength event $\lambda_{ci,y} \cdot \text{sign}(\omega_y)$ in the low-pass filtered velocity fields at $y/\delta = 0.33$ considering only positive values. The Q -criterion (magenta) shows two counter-rotating vortices inclined at 45 degrees with the wall and with a low speed zone in between, which is shown by the iso-surface of the fluctuating streamwise component of velocity $u' = 0$ (blue). Together the vortices and low velocity constitute a hairpin vortex signature, where the vortices in figure 10.11 are part of a neck on either side of the hairpin head. As will be shown later, the hairpins are often skewed, which results in the reduced swirling strength in the second hairpin neck ($r_z/\delta = -0.4$) due to averaging. The conditional average shows furthermore that the large-scale hairpin is related to very long zones of relative low velocity approximately 0.4δ wide. This may suggest that these long low speed zones are actually formed by the large-scale vortices and that the smaller scale hairpins (section 10.3.2) are in turn more local features developing on or inside the low speed zones (see also section 10.4).

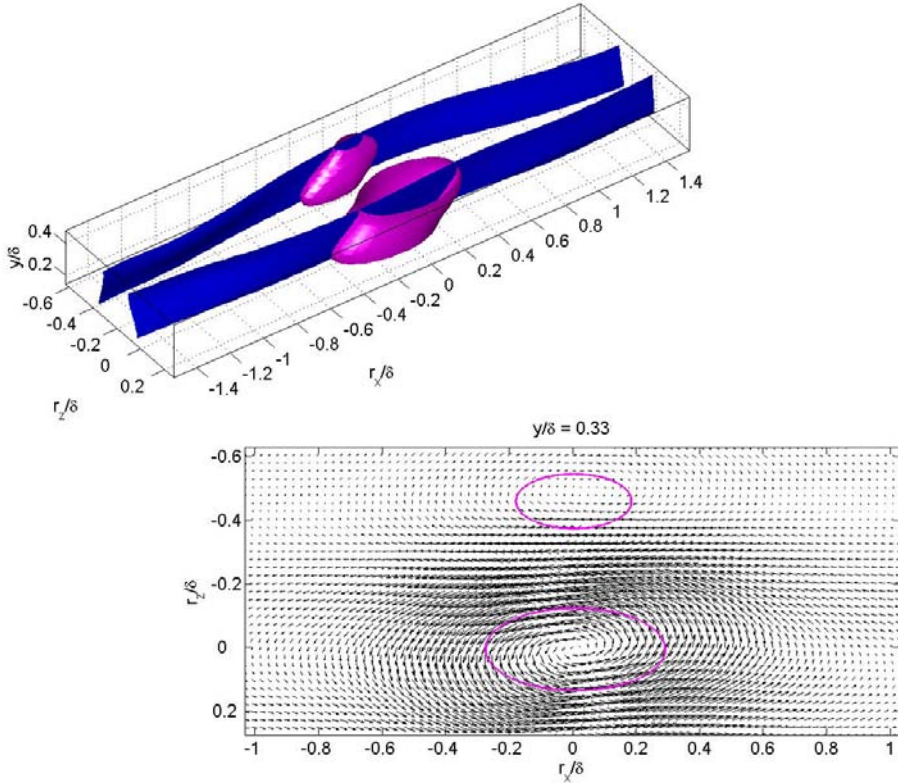


Figure 10.11: Conditional eddy (top) given a positive wall normal swirling event in the low pass filtered data at $y/\delta = 0.33$ visualized using the Q vortex detection criterion (magenta) and low speed zones (blue, $u' < 0$) with corresponding vector plot in the x,z cross-section (bottom). The velocity vectors are relative to the local average velocity.

Additional support for the existence of large-scale hairpins is given by the hairpin heads commonly observed in the volumes covering $0.56 < y/\delta < 0.89$. Two examples showing vortical motion (magenta) and low speed zones (blue) in the low-pass filtered velocity fields at that height are presented in figure 10.12. In the top volume isolated arches and canes are seen with a short low speed zone between the necks, as expected. The second volume (figure 10.12-bottom) reveals the streamwise arrangement of an arch vortex and a neck around an elongated low speed zone. The neck may belong to an even taller hairpin vortex structure. Assuming that the energy around $\lambda_x/\delta = 2$ in the pre-multiplied power spectrum $k_x \Phi_{uu}$ (figure 10.9) is directly related to the large-scale hairpins, the decreasing energy peak value for $y/\delta > 0.7$ may indicate that the large-scale hairpins are approximately 0.7δ tall, which agrees with the present observation that very few heads are returned in the low-pass filtered volumes closer to the wall. Furthermore it should be noted that at the upper half of the boundary layer large-scale streamwise vortices have rarely been observed.

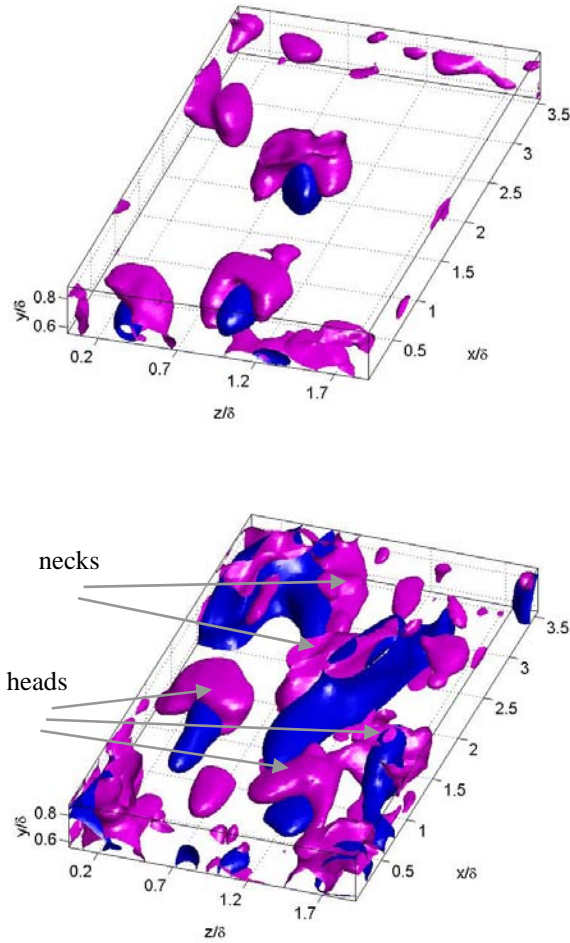


Figure 10.12: Hairpin heads observed in the low pass filtered velocity fields above $y/\delta = 0.6$ visualized using the Q -criterion (magenta) and low speed zones (blue, $u < 0.95 \cdot U_e$).

In the instantaneous low-pass filtered velocity field alignment of the large-scale hairpins is frequently observed along diagonal lines. One of the clearest examples of diagonal alignment is presented in figure 10.13-bottom showing velocity vectors and wall-normal swirl $\lambda_{ci,y}$ contours in the plane parallel to the wall at $y/\delta = 0.33$. The hairpin signatures have been indicated in the plot by circles and the dashed lines indicate the diagonals along which the hairpins appear to be aligned. Figure 10.13-bottom also shows that the hairpin vortices are skewed, which in the incompressible boundary layer has been observed typically for large-scale hairpins extending beyond $y/\delta > 0.5$ (section 8.3.1). For comparison the original (unfiltered) velocity distribution in the same plane is presented in figure 10.13-top. Between the filtered and unfiltered plots little difference is observed in the low speed zones. However the difference in vortical structures is profound appearing almost random in the unfiltered

data but more organized after filtering. It should be noted here that the applied filter has a relatively small local support (i.e. considers vectors only within the $0.78\delta \times 0.18\delta \times 0.28\delta$ size kernel), which makes it unlikely that the observed organized pattern is introduced by the filter.

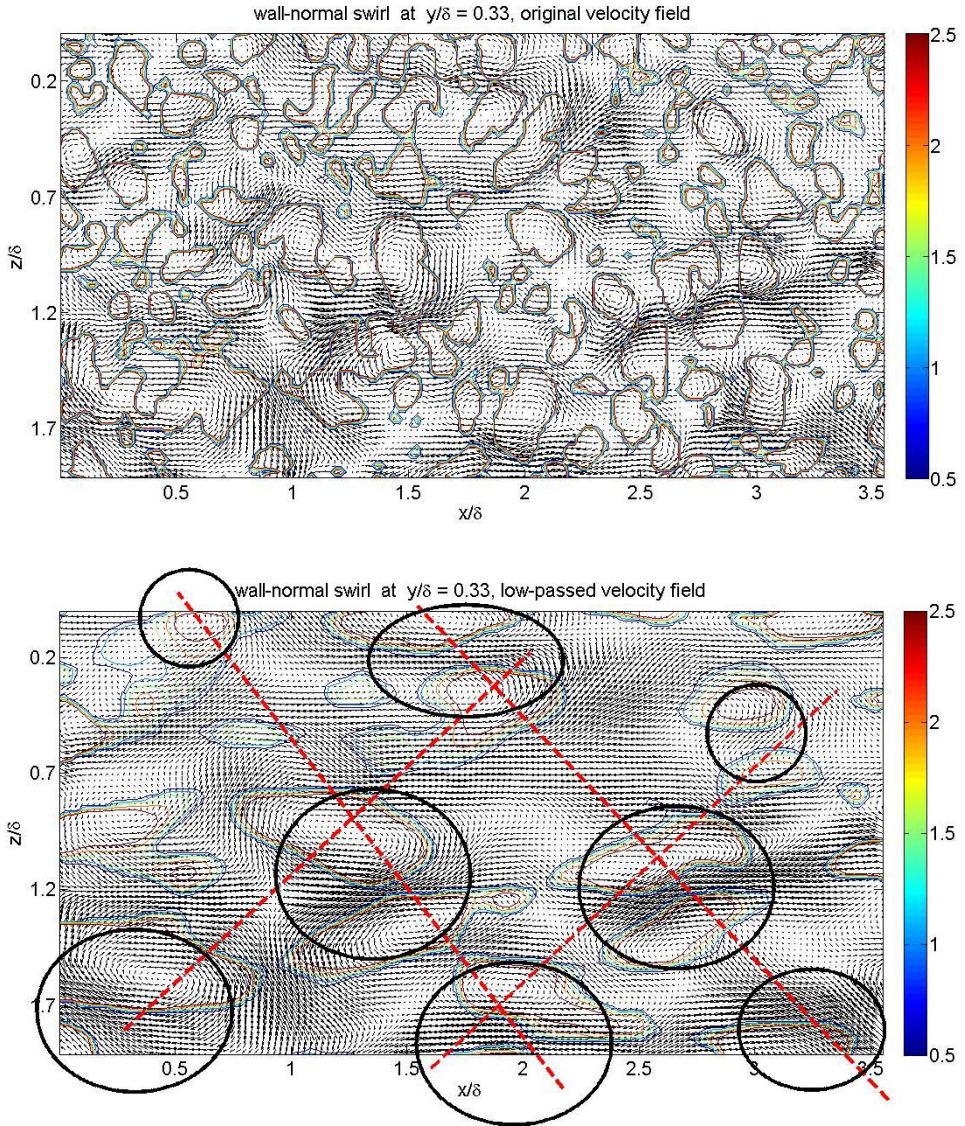


Figure 10.13: Velocity vectors in the x,z plane at $y/\delta = 0.33$ and wall-normal swirl $\lambda_{ci,y}$ contours, original measured velocity field (top) and low-pass filtered field (bottom). Hairpin and cane vortex signatures are indicated by the circles. The dashed lines show alignment of the hairpins along diagonal lines.

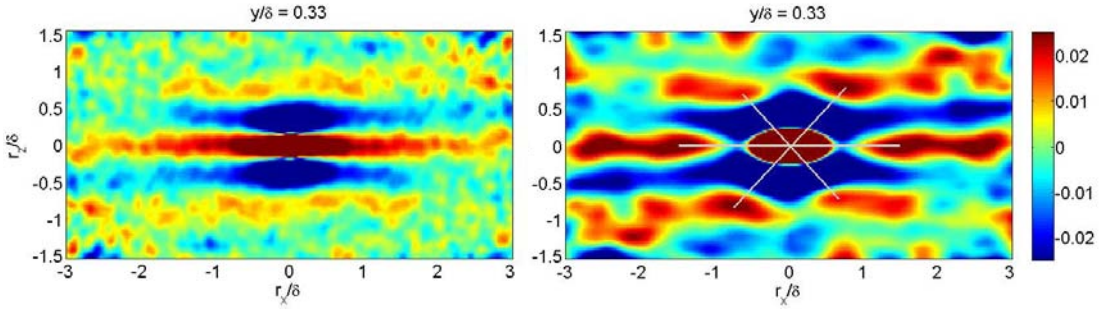


Figure 10.14: Autocorrelation coefficient of the directional wall normal swirl $\lambda_{ci,y} \cdot \text{sign}(\omega_y)$ in the plane $y/\delta = 0.33$ parallel to the wall. Left: original velocity field. Right: low pass filtered velocity field.

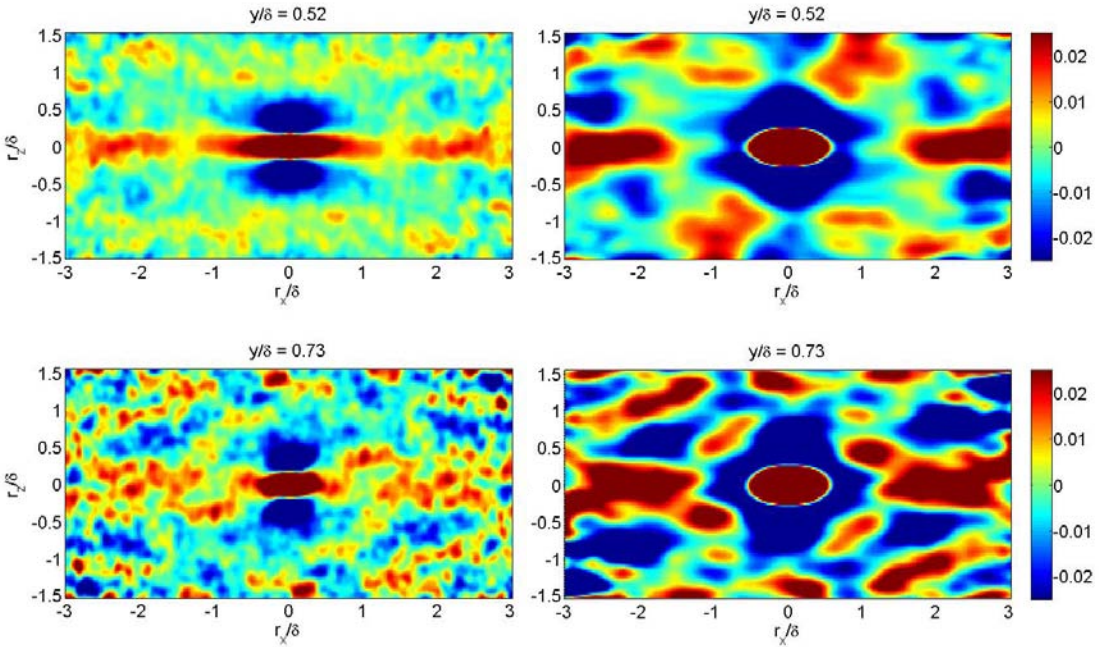


Figure 10.15: Autocorrelation coefficient of the directional wall normal swirl $\lambda_{ci,y} \cdot \text{sign}(\omega_y)$ in the planes $y/\delta = 0.52$ (top) and 0.73 (bottom). Left: original velocity field. Right: low pass filtered velocity field.

Statistical support for the diagonal alignment of the large-scale hairpins is found in the autocorrelation of wall-normal swirl strength $\lambda_{ci,y} \cdot \text{sign}(\omega_y)$ in a plane parallel to the wall (figure 10.14-right). Positive correlation peaks are found in streamwise direction at 1.5δ distance from the DC peak and along the 45-degree diagonals at 0.8δ distance from the DC

peak in both spanwise and streamwise direction (indicated by the gray lines). This means that starting from a wall-normal vortex on average co-rotating wall-normal vortices exists at these relative positions, as is approximately the case in the instantaneous results of figure 10.13. Furthermore the autocorrelation function shows local minima adjacent to maxima in spanwise direction at 0.4δ distance, most noticeably on either side of the DC peak, which can be explained by the large-scale hairpins having counter-rotating necks 0.4δ apart (figure 10.11). For comparison figure 10.14-left shows the autocorrelation of $\lambda_{ci,y}\text{sign}(\omega_y)$ based on the original unfiltered velocity fields, in which case no obvious diagonal alignment but only strong streamwise alignment is observed.

Figure 10.15 presents the autocorrelation coefficients of wall normal swirl $\lambda_{ci,y}\text{sign}(\omega_y)$ in the planes $y/\delta = 0.52$ and 0.73 , which have been determined from 480 and 120 snapshots respectively. The autocorrelation of the unfiltered velocity fields (left) reveals a decreasing width of the DC peak in streamwise direction with distance from the wall, which indicates a reduced streamwise alignment of hairpins, i.e. decreasing hairpin packet length, away from the wall confirming observations on the length of low speed zones in the instantaneous velocity fields (section 10.3.1). It is also seen from the figure that the correlation map for $y/\delta = 0.73$ is very noisy, which is mainly due to the reduced number of snapshots, but it is also due to the decreasing variance with distance from the wall (decreasing number of wall normal vortices). The autocorrelation map of the low pass filtered velocity fields at $y/\delta = 0.52$ (top-right) show positive correlation along the 45-degree diagonals at approximately the same location as before (figure 10.14). The positive peak in streamwise direction at 1.5δ distance from the DC peak found at $y/\delta = 0.33$ does not appear at $y/\delta = 0.52$, even though a positive correlation is returned, but seems to have shifted to approximately 2δ . It is not obvious what causes this peak to disappear or shift, but it may be related to the intermittency of the turbulent flow structures at this height in the boundary layer. Finally the lack of statistical convergence prohibits a conclusion on the alignment of the large scale hairpins at $y/\delta = 0.73$ (figure 10.15-bottom-right). Moreover, many of the large scale hairpins do not extend beyond $y/\delta = 0.7$, as discussed above (see also figure 10.12).

10.4 Discussion

In the above two scales of hairpin vortices have been observed: the large-scale hairpins (section 10.3.3) with a width typically of 0.4δ and a smaller-scale 0.25δ wide hairpin (section 10.3.2). The latter is at least 4 times stronger than the large-scale hairpin in terms of their peak Q -value (Eq. 7.7). Both types of vortices are found near the low-speed zones, and therefore the question arises how these vortices are organized relative to each other.

A possible answer to this question is given by the short δ -scale low-speed zones occasionally observed in the measured velocity volumes. An example is presented in figure 10.16, where the low-speed zone (blue) extends upstream of a single large-scale cane vortex with only part of the neck (magenta) inside the measurement volume. It must be noted that the low-speed zone extends down to $x/\delta = 2.6$, where u is just above the applied threshold for the blue iso-surface and is approaching the local average velocity. Over the low-speed zone several smaller-scale arch and cane shaped vortices (green) are seen. The most downstream vortices (denoted ‘canes’ in figure 10.16) appear slightly larger and more distorted compared to the upstream arches. This result suggests that the smaller scales occur

or are formed on the low-speed zone associated to the neck and leg of the large-scale cane (or hairpin).

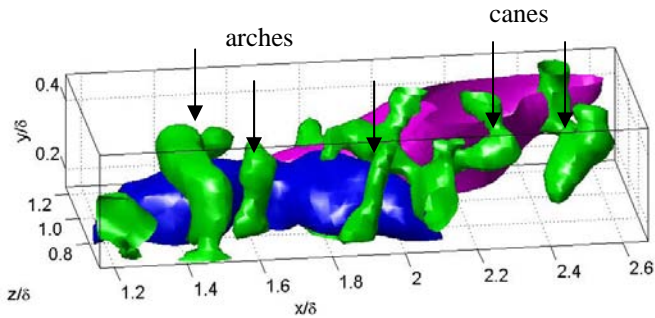


Figure 10.16: Large and smaller scale vortices observed around a short 1.4δ low speed zone. Blue represents part of a low speed zone ($u < 0.84 \cdot U_e$), green is a Q -isosurface indicating vortical motion in the unfiltered velocity and magenta is an isosurface of the wall-normal swirl in the low-pass filtered velocity, which indicates the neck of a large scale cane.

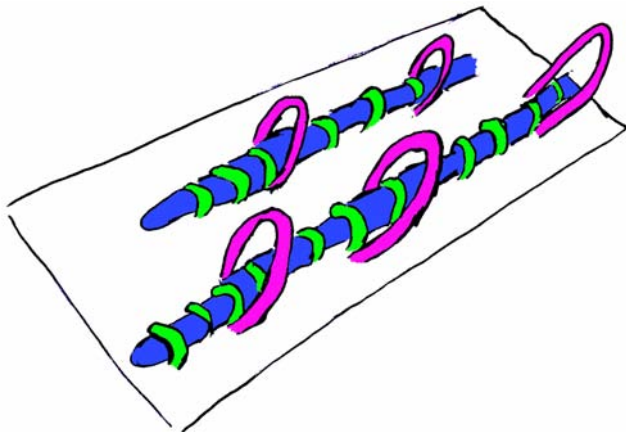


Figure 10.17: Conceptual sketch of the large-scale (magenta) and smaller-scale hairpins (green) around the long low-speed zones near the wall (blue).

The findings are summarized in the conceptual sketch of figure 10.17, in which the large-scale hairpins are aligned in streamwise direction and along the diagonals as suggested by the autocorrelations function (figure 10.14). Near the wall ($y/\delta < 0.5$), the neck and legs of these large-scale hairpins create long low-speed zones, as observed in the conditional eddy of figure 10.11, which then connect to form the very long low-speed zones reported in literature (e.g. Kim and Adrian 1999, Hutchins and Marusic 2007, Ganapathisubramani et al. 2007). The smaller-scale hairpins in turn are located on top or inside the low-speed zones.

Further from the wall, say $y/\delta > 0.5$, shorter hairpin packets are found near the heads and necks of the large-scale hairpins. These packets generally do not connect in streamwise direction and therefore do not form very long zones of uniform low velocity. Consequently

the streamwise coherence length decreases with distance from the wall, as has been observed for instance in the autocorrelation maps of the wall normal swirl (figure 10.15). Furthermore the presence of hairpin packets in each snapshot at all three heights investigated suggest that several uniform (low-) momentum zones (Meinhart and Adrian, 1995) or packets stacked on top of each other (figure 7.6, Adrian et al. 2000) can exist simultaneously within the envelope of retarded flow induced by the large-scale hairpins. In this picture the uniform momentum zone near the wall correspond to the observed very long low speed zones (figure 10.17), whereas the uniform momentum zones further from the wall are the shorter hairpin packets as seen in figure 10.4.

Moreover, it is conjectured that the large-scale hairpins have a regulating/ordering function. As observed in the time-resolved velocity volumes of a low Reynolds number flow (section 9.3.3), hairpin vortices can be destroyed under the influence of high speed fluid and sweep events ($u' > 0$ and $v' < 0$) outboard of the larger-scale hairpins. This may explain why so few hairpins are observed in the high speed flow regions, outside the envelope of retarded fluid induced by the large-scale hairpins (section 10.3.1). The conditions inside this envelope, however, seem favorable for the development and growth of hairpins, so that the observed flow organization is sustained for long periods of time.

10.5 Conclusions

Tomographic-PIV has been applied to investigate the instantaneous structure of a supersonic turbulent boundary layer with $Re_\theta = 34,000$, $M_e = 2.1$ and thickness $\delta = 20$ mm. The measurements return a quantitative visualization of 3D flow structures in the outer layer from 0.15δ to 0.89δ distance to the wall. However, the individual measurement volume ranges over $3.5\delta \times 0.32\delta \times 1.8\delta$ in streamwise, wall-normal and spanwise direction and contains $142 \times 14 \times 77$ velocity vectors, and consequently three measurement configurations have been used to cover different parts of the outer layer.

The instantaneous velocity fields for $0.15 < y/\delta < 0.47$ show long low-speed zones commonly extending beyond the measurement volume. Over these zones hairpin vortices are observed, aligned in streamwise direction forming so called packets. Statistical support for the existence of hairpins at the present Reynolds and Mach number is given by the conditional averaged eddy (figure 10.7).

The pre-multiplied power spectra for each velocity component indicate the presence of large-scale motion in the boundary layer. The velocity fields have been low-pass filtered using a second order regression to reveal streamwise vortices and signatures of large-scale hairpins. The latter are 0.4δ wide, at least 0.5δ high, and appear to occur periodic in streamwise direction (at 1.5δ spacing) and along the diagonals at 45 degrees with streamwise direction in the plane parallel to the wall.

Isolated short δ -scale low-speed zones suggest that the smaller-scale hairpins form a packet over the low-speed zone associated to the leg and neck of a large-scale hairpin. The long low-speed zones in turn are formed by several of these large-scale hairpins with packets aligned in streamwise direction (figure 10.17).

Chapter 11

Overall conclusions and outlook

11.1

Conclusions

Tomographic-PIV is a newly developed technique for 3D velocity measurements, in which the three-dimensional particle distribution within the measurement volume is reconstructed by optical tomography from particle image recordings taken simultaneously from several viewing directions. The optical arrangement for illumination and recording resembles that of stereoscopic-PIV and 3D-PTV. Velocity information results from three-dimensional particle pattern cross-correlation of two volume reconstructions obtained from subsequent exposures of the particle images. The measurement chain is therefore fully digital with the advantage of being instantaneous within a volume, which makes it suitable for the analysis of flows irrespective of the flow speed. The experimental parameters dominating the accuracy of the reconstruction procedure are the particle seeding density and the number of viewing cameras. Other relevant parameters affecting the reconstruction are volume depth, calibration error and image noise. The accuracy of the velocity measurement by cross-correlation, however, has been demonstrated not to be sensitive to the seeding density, hence reconstruction accuracy, which makes the technique particularly robust. The velocity accuracy is close to that of standard PIV as assessed through synthetic experiments and by direct comparison of the returned velocity statistics with stereoscopic-PIV in a real experiment. Moreover, the instantaneous velocity fields returned in the circular cylinder wake at $Re_D = 2700$ show the three-dimensional flow organization and the vorticity level as expected from literature.

Using high-repetition rate PIV equipment the requirements for time-resolved experiments in air flows at a moderate speed can be matched. A first application of this type was presented in Schröder et al. (2008) and in chapter 9 showing a turbulent boundary layer in air measured at 5 kHz and 1.5 kHz respectively. A specific illumination arrangement with multiple reflections of the light beam was needed to increase the local light intensity by a factor 7.

So far the technique has been applied to turbulent wake flows and boundary layers in both air and water. An overview of the measurement volumes, vector yields and related experimental parameters from the present study and recent literature is given in table 11.1. All applications have used a four-camera system typically returning 50k to 100k velocity vectors using $1k \times 1k$ cameras or up to 650k vectors using $2k \times 2k$ cameras. While early datasets contain approximately 100 instantaneous snapshots (e.g. the cylinder wake of chapter 5), recent experiments easily consist of 1000 (e.g. the time-resolved boundary layer study in chapter 9), which demonstrates the technique rapidly matures and is capable of returning flow statistics.

Table 11.1: Applications overview with some experimental parameters.

	Cylinder wake in air (chapter 5)	Time-resolved cylinder wake in water (Michaelis et al. 2006)	Turbulent boundary layer in air (chapter 8)	Supersonic turbulent boundary layer (chapter 10)	Time-resolved boundary layer in air (Schröder et al. 2008)
Image size [pixels]	1376×1040	2048×2048	1376×1040	2048×2048	800×768
Recording rate [Hz]	1	10	2	10	5000
Measurement volume, L×H×D [mm ³]	37×36×8	88×59×16	33×26×11	70×35×6.5	34×30×19
Spatial resolution [voxels/mm]	18.2	23.6	26.6	20.0	24
Particle concentration [particles/mm ³] (total number)	2.1 (23,000)	1.2 (98,000)	3.3 (32,000)	4.2 (65,000)	0.94 (18,000)
Number of vectors* (total)	77×79×15 (91,000)	174×117×32 (651,000)	69×54×25 (93,000)	142×77×14 (153,000)	46×41×24 (45,000)

* using 75% overlap between interrogation volumes

A 3D description of hairpins and arch vortices has been possible from the applications to the outer layer of turbulent boundary layers at $Re_\theta = 1900$ ($M \approx 0$) and $Re_\theta = 34,000$ ($M = 2.1$). These vortices are predominantly asymmetric and appear very similar in shape and size for both Reynolds numbers when plotted in outer (δ) scaling. Moreover, conditional eddies have been computed based on linear stochastic estimation using negative spanwise swirl as the specified event, which can be interpreted as the average flow field associated to a hairpin head. The conditional eddies are symmetric hairpins as a result of averaging where the hairpin necks are inclined at 45 degrees with the wall as expected. Furthermore a region of relatively low speed is found underneath the head and in between the two necks with a characteristic ejection event ($u' < 0$, $v' > 0$) just below and upstream of the head and sweep events ($u' > 0$, $v' < 0$) are found outboard of the necks in agreement with observations of Robinson (1991) in DNS data. Further upstream of the eddy a shear layer inclined at approximately 20 degrees with the wall is returned, which separates the incoming high speed flow from the low speed flow associated to the eddy. Again the eddies are very similar for both Reynolds number cases suggesting that the hairpin is a universal feature, also in supersonic turbulent boundary layers.

In the low Re_θ turbulent boundary layer hairpins are found aligned in streamwise direction forming so called packets, which are observed in more than 90% of the snapshots below $y/\delta = 0.5$. The hairpins in a packet are associated to a common zone of low speed flow having a width of typically 0.3δ and a length of around δ . The packets yield significant contributions to Reynolds shear stress as has been predicted by Adrian et al. (2000). For high Re_θ case the packets themselves also seem to align in streamwise direction forming very long streamwise zones ($> 3\delta$) of relatively low velocity.

The large-scale and very-large-scale motions in the high Re_θ supersonic boundary layer have been investigated further by low-pass filtering of the measured velocity distribution. The filtered data reveal large-scale hairpins and streamwise vortices, where the latter are believed to be the legs of the hairpins. Furthermore, large-scale hairpins are 0.4δ wide, at least 0.5δ high, and appear to occur periodic in streamwise direction (at 1.5δ spacing) and along the diagonals at 45 degrees with streamwise direction in the plane parallel to the wall, thereby displaying a staggered arrangement in that plane. This diagonal alignment indicates a very-large-scale spanwise organization exists together with the known very-large-scale streamwise organization.

The hairpin dynamics have been visualized in low Reynolds number transitional boundary layer using nearly time-resolved Tomographic-PIV. The results show predominantly convection with slow growth of the hairpins, where the hairpin heads describe a average path inclined at 0.60 to 0.90 degrees with the wall. The birth of a new hairpin and the death of old hairpins have been observed rarely (in approximately 3% of the volumes). Individual examples show birth as the roll-up of the shear layer over a low speed zone and death as a rapid deformation with decay of the hairpin necks under the influence of a large sweep event. Both birth and death are relatively dynamic with a fast sequence of events, which are not fully resolved by the 1.5 kHz system.

11.2

Outlook

One of the current limitations of Tomographic-PIV is the large processing time required for the reconstruction and interrogation (approximately 1 hour for 10^8 voxels on a Pentium 4 PC). Therefore further developments of the technique are expected to be directed towards the reduction of the computational load by advanced algorithms for reconstruction and 3D correlation exploiting the sparseness of the reconstructed volumes. Because the majority of the voxels intensities are zero (90 to 95% after the first MART iteration), they do not contribute in the computations and may be skipped. Furthermore, volume self-calibration is expected to become standard, which will reduce restrictions on the accuracy of the initial calibration and will increase robustness and user friendliness of the technique. On the part of the assessment of the technique, a detailed model describing the ghost particle contribution to the cross-correlation peak is desirable (even if measurements do not show an appreciable effect).

It is interesting to extend the application range from the simple flow geometries (e.g. flat plate and cylinder wake) to more complicated geometries and measurement volumes in close proximity of models, possibly with the model in background. This may require procedures masking or filtering out the model in the images or alternatively using non-rectangular reconstruction volumes.

Concerning the study of coherent structures in turbulent boundary layers, fully time-resolved information (compared with nearly time-resolved in chapter 9) is expected to increase the level of detail with which dynamic processes such as hairpin formation and bursting processes near the wall can be described. This will provide valuable information, since most studies (like the present) focus on a kinematic description. The experimental challenge related to the study of the dynamics (and at the same time perhaps responsible for the success of the kinematic description) is the long life-time of the coherent structures, which is commonly much longer than the time it takes for a structure to convect through a static measurement volume.

The staggered arrangement of the large-scale hairpins as observed in the present $Re_\theta = 34,000$ supersonic boundary layer, raises several questions that remain to be explored, such as what is its origin and what is the range of Reynolds (and Mach) numbers for which it occurs. Furthermore, can the proposed model of large-scale hairpins and smaller-scale hairpins around the long low-speed zones (figure 10.17) explain all the observed velocity and swirling strength statistics in turbulent boundary layers? Currently a modeling approach, similar to what has been described in section 7.2.3, is undertaken by Baltzer and Adrian (private communication) aiming at answering this last question.

Finally, what may be the relevance of the present observations in wall-turbulence to aerodynamics? It is speculated that drag reduction using (active) flow control strategies may become easier when boundary layer displays organization over large distances. For instance, control devices (e.g. jets, blowing and suction slots or passive vortex generators) can be spatially distributed according to the very-large scales. A more direct application of the results is related to shock wave turbulent boundary layer interactions, which occur frequently in for example air intakes of supersonic aircraft or over the wings of transonic aircraft. The shock position in the interaction fluctuates leading to problems of unsteady structural loading. Recent studies (e.g. Ganapathisubramani et al. 2007b, Humble et al. 2007b) have shown a correlation between the flow organization in the boundary layer immediately upstream of the interaction and the shock position. The description of the organization of the boundary layer therefore helps in the understanding of the mechanism and modes of the observed shock unsteadiness.

References

- Adrian RJ** (1991) Particle-imaging techniques for experimental fluid mechanics. *Ann Rev Fluid Mech*, Vol 23, 261-304
- Adrian RJ** (1996) Stochastic estimation of the structure of turbulent fields. In: *Eddy structure identification*. Ed. Bonnet J.P., Springer-Verlag, New York, 145-195
- Adrian RJ** (2007) Hairpin vortex organization in wall turbulence. *Phys Fluids*, Vol 19, 041301
- Adrian RJ; Liu ZC** (2002) Observation of vortex packets in direct numerical simulation of fully turbulent channel flow. *J Visualization*, Vol 5, 9-19
- Adrian RJ; Meinhart CD; Tomkins CD** (2000) Vortex organization in the outer region of the turbulent boundary layer. *J Fluid Mech*, Vol 422, 1-54
- Adrian RJ; Yao CS** (1985) Pulsed laser technique application to liquid and gaseous flows and the scatter power of seed material. *Appl Opt*, Vol 24, 44-52
- Anderson, JD** (1991) *Fundamentals of aerodynamics*. 2nd edition, McGraw-Hill, New York
- Antonia RA; Bisset DK; Browne LWB** (1990) Effect of Reynolds number on the topology of the organized motion in a turbulent boundary layer. *J Fluid Mech*, Vol 213, 267-286
- Arroyo MP; Greated CA** (1991) Stereoscopic particle image velocimetry. *Meas Sci Technol*, Vol 2, 1181-1186
- Arroyo MP; Hinsch KD** (2007) Recent developments of PIV towards 3D measurements. In: *Particle image velocimetry: New developments and recent applications*. Ed. Schröder A; Willert CE, Springer, Berlin Heidelberg New York
- Balakumar BJ; Adrian RJ** (2007) Large- and very large-scale motions in channel and boundary-layer flows. *Phil Trans R Soc A*, Vol 365, 665-681
- Brücker Ch** (1995) Digital-Particle-Image-Velocimetry (DPIV) in a scanning light-sheet: 3D starting flow around a short cylinder. *Exp Fluids*, Vol 19, 255-263
- Burgmann S; Brücker C; Schröder W** (2006) Scanning PIV measurements of a laminar separation bubble. *Exp Fluids*, Vol 41, 319-326
- Cantwell BJ** (1981) Organized motion in turbulent flow. *Ann Rev Fluid Mech*, Vol 13, 457-515
- Chakraborty P; Balachandar S; Adrian RJ** (2005) On the relationship between local vortex identification schemes. *J Fluid Mech*, Vol 535, 189-214
- Chan VSS; Koek WD; Barnhart DH; Bhattacharya N; Braat JJM; Westerweel J** (2004) Application of holography to fluid flow measurements using bacteriorhodopsin (bR). *Meas Sci Technol*, Vol 15, 647-655
- Chong MS; Perry AE; Cantwell BJ** (1990) A general classification of three-dimensional flow. *Phys Fluids A*, Vol 2, 765-777
- Christensen KT; Adrian RJ** (2001) Statistical evidence of hairpin vortex packets in wall turbulence. *J Fluid Mech*, Vol 431, 433-443
- Coëtmellec S; Buraga-Lefebvre C; Lebrun D; Özkul C** (2001) Application of in-line digital holography to multiple plane velocimetry. *Meas Sci Technol*, Vol 12, 1392-1397
- Corino ER; Brodkey RS** (1969) A visual investigation of the wall region in turbulent flow. *J Fluid Mech*, Vol 37, 1-30

- Delo CJ; Kelso RM; Smits AJ** (2004) Three-dimensional structure of a low-Reynolds-number turbulent boundary layer. *J Fluid Mech*, Vol 512, 47-83
- Elsinga GE; Van Oudheusden BW; Scarano F; Watt DW** (2004) Assessment and application of quantitative schlieren methods: Calibrated color schlieren and background oriented schlieren. *Exp Fluids*, Vol 36, 309-325
- Elsinga GE; Van Oudheusden BW; Scarano F** (2005) Evaluation of aero-optical distortion effects in PIV. *Exp Fluids*, Vol 39, 246-256
- Elsinga GE; Van Oudheusden BW; Scarano F** (2005b) The effect of particle image blur on the correlation map and velocity measurement in PIV. *SPIE optics and photonics 2005*, San Diego CA, USA, paper 5880-37
- Elsinga GE; Scarano F; Wieneke B; van Oudheusden BW** (2006) Tomographic particle image velocimetry. *Exp Fluids*, Vol 41, 933-947
- Elsinga GE; van Oudheusden BW; Scarano F** (2006b) Experimental assessment of tomographic-PIV accuracy. *13th Int. Symp. on Laser Techniques to Fluid Mech.*, Lisbon, Portugal, paper 20.5
- Elsinga GE; Kuik DJ; van Oudheusden BW; Scarano F** (2007) Investigation of the three-dimensional coherent structures in a turbulent boundary layer. *45th AIAA Aerospace Sciences Meeting*, Reno, NV, USA, AIAA-2007-1305
- Falco RE** (1977) Coherent motions in the outer region of turbulent boundary layers. *Phys Fluids*, Vol 20, S124-S132
- Ganapathisubramani B; Longmire EK; Marusic I** (2003) Characteristics of vortex packets in the turbulent boundary layer. *J Fluid Mech*, Vol 478, 35-46
- Ganapathisubramani B; Clemens NT; Dolling DS** (2006) Large-scale motions in a supersonic turbulent boundary layer. *J Fluid Mech*, Vol 556, 271-282
- Ganapathisubramani B; Clemens NT; Dolling DS** (2007) Effects of upstream coherent structures on low-frequency motion of shock-induced turbulent separation. *45th AIAA Aerospace Sciences Meeting*, Reno, NV, USA, AIAA-2007-1141
- Ganapathisubramani B; Clemens NT; Dolling DS** (2007b) Effects of upstream on the unsteadiness of shock-induced separation. *J Fluid Mech*, Vol 585, 369-394
- George WK** (2006) Recent advancements toward the understanding of turbulent boundary layers. *AIAA J*, Vol 44, 2435-2449
- Hain R; Kähler CJ; Tropea C** (2007) Comparison of CCD, CMOS and intensified cameras. *Exp Fluids*, Vol 42, 403-411
- Head MR; Bandyopadhyay P** (1981) New aspects of the turbulent boundary layer structure. *J Fluid Mech*, Vol 107, 297-338
- Hecht E** (1998) *Optics*. 3rd edition. Addison Wesley, Reading, MA, USA
- Herman GT; Lent A** (1976) Iterative reconstruction algorithms. *Compt Biol Med*, Vol 6, 273-294
- Herman GT** (1980) *Image reconstruction from projections: The fundamentals of computerized tomography*. Academic Press, London, New York
- Herrmann S; Hinrichs H; Hinsch KD; Surmann C** (2000) Coherence concepts in holographic particle image velocimetry. *Exp Fluids*, Suppl, S108-S116
- Hinsch KD** (2002) Holographic particle image velocimetry. *Meas Sci Technol*, Vol 13, R61-R72
- Hori T; Sakakibara J** (2004) High-speed scanning stereoscopic PIV for 3D vorticity measurement in liquids. *Meas Sci Technol*, Vol 15, 1067-1078
- Huang JF; Zhou Y; Zhou T** (2006) Three-dimensional wake structure measurement using a modified PIV technique. *Exp Fluids*, Vol 40, 884-896

- Humble RA; Scarano F; van Oudheusden BW; Tuinstra M** (2006) PIV measurements of Shock Wave/Turbulent Boundary Layer Interaction. 13th Int. Symp. on Laser Techniques to Fluid Mech., Lisbon, Portugal, paper 14.2
- Humble RA; Scarano F; van Oudheusden BW** (2007) Particle image velocimetry measurements of shock wave/turbulent boundary layer Interaction. *Exp Fluids*, Vol 43, 173-183
- Humble RA; Elsinga GE; Scarano F; van Oudheusden BW** (2007b) Instantaneous 3D flow organization of a shock wave/turbulent boundary layer interaction using Tomographic PIV. 37th AIAA Fluid Dynamics Conference & Exhibit, Miami, FL, USA, AIAA-2007-4112
- Hunt JCR; Wray AA; Moin P** (1988) Eddies, stream, and convergence zones in turbulent flows. Center for Turbulence Report, CTR-S88, 193-208
- Hussain AKMF** (1986) Coherent structures and turbulence. *J Fluid Mech*, Vol 173, 303-356
- Hutchins N; Marusic I** (2007) Evidence of very long meandering features in the logarithmic region of turbulent boundary layers. *J Fluid Mech*, Vol 579, 1-28
- Jeong J; Hussain F** (1995) On the identification of a vortex. *J Fluid Mech*, Vol 285, 69-94
- Jimenez J; Simens MP** (2001) Low-dimensional dynamics of turbulent wall flow. *J Fluid Mech*, Vol 435, 81-91
- Jischa M** (1982) Konvektiver Impuls-, Wärme- und Stoffaustausch. Vieweg & Sohn, Braunschweig, Wiesbaden
- Kähler CJ** (2004) The significance of coherent flow structures for the mixing in wall-bounded flows. PhD dissertation, DLR Forschungsbericht 2004-24, ISSN 1434-8454
- Kähler CJ; Kompenhans J** (2000) Fundamentals of multiple plane stereo particle image velocimetry. *Exp Fluids*, Suppl, S70-S77
- Kim KC; Adrian RJ** (1999) Very large-scale motion in the outer layer. *Phys Fluids*, Vol 11, 417-422
- Kim HT; Kline SJ; Reynolds WC** (1971) The production of turbulence near a smooth wall in a turbulent boundary layer. *J Fluid Mech*, Vol 50, 133-160
- Klebanoff PS** (1955) Characteristics of turbulence in a boundary layer with zero pressure gradient. NACA Report, No 1247
- Kline SJ; Reynolds WC; Schraub RA; Runstadler PW** (1967) The structure of turbulent boundary layers. *J Fluid Mech*, Vol 30, 741-773
- LaVision GmbH** (2006) Davis 7 manual, Göttingen, Germany
- Lüthi B; Tsinober A; Kinzelbach W** (2005) Lagrangian measurement of vorticity dynamics in turbulent flow. *J Fluid Mech*, Vol 528, 87-118
- Maas HG; Gruen A; Papantoniou D** (1993) Particle tracking velocimetry in three-dimensional flows. *Exp Fluids*, Vol 15, 133-146
- Martin MP** (2007) Direct numerical simulation of hypersonic turbulent boundary layers. Part 1: Initialization and comparison with experiments. *J Fluid Mech*, Vol 570, 347-364
- Marusic I** (2001) On the role of large-scale structures in wall-turbulence. *Phys Fluids*, Vol. 13, 735-743
- Melling A** (1997) Tracer particles and seeding for particle image velocimetry. *Meas Sci Technol*, Vol 8, 1406-1416
- Meinhart CD; Adrian RJ** (1995) On the existence of uniform momentum zones in a turbulent boundary layer. *Phys Fluids*, Vol 7, 694-696
- Michaelis D; Poelma C; Scarano F; Westerweel J; Wieneke B** (2006) A 3D time-resolved cylinder wake survey by tomographic PIV. 12th Int Symp on Flow Visualization, Göttingen, Germany, paper 12.1

- Mishra D; Muralidhar K; Munshi P** (1999) A robust MART algorithm for tomographic applications. *Num Heat Transfer, Part B*, Vol 35, 485-506
- Moin P; Kim J** (1985) The structure of the vorticity field in turbulent channel flow. Part 1: analysis of instantaneous fields and statistical correlations. *J Fluid Mech*, Vol 155, 441-464
- Mullin JA; Dahm WJA** (2006) Dual-plane stereo particle image velocimetry measurements of velocity gradient tensor fields in turbulent shear flow. I. Accuracy assessment. *Phys Fluids*, Vol 18, 035101
- Pan G; Meng H** (2002) Digital holography of particle fields: reconstruction by use of complex amplitude. *Appl Optics*, Vol 42, 827-833
- Pereira F; Gharib M; Dabiri D; Modarress D** (2000) Defocusing digital particle image velocimetry: a 3-component 3-dimensional DPIV measurement technique. *Exp Fluids, Suppl*, S78-S84
- Perry AE; Chong MS** (1982) On the mechanism of wall turbulence. *J Fluid Mech*, Vol 119, 173-217
- Perry AE; Marusic I** (1995) A wall-wake model for the turbulent structure of boundary layers. Part1: extension of the attached eddy hypothesis. *J Fluid Mech*, Vol 298, 361-388
- Prasad AK** (2000) Stereoscopic particle image velocimetry. *Exp Fluids*, Vol 29, 103-116
- Pu Y; Meng H** (2000) An advanced off-axis holographic particle image velocimetry (HPIV) system. *Exp Fluids*, Vol 29, 184-197
- Raffel M; Willert CE; Kompenhans J** (1998) Particle image velocimetry: A practical guide. Springer Verlag, Berlin, Heidelberg
- Richard H; Raffel M** (2001) Principle and applications of the background oriented schlieren (BOS) method. *Meas Sci Technol*, Vol 12, 1576-1585
- Ringuette MJ; Wu M; Martin MP** (2007) Coherent structures in DNS of turbulent boundary layers at Mach 3. 45th AIAA Aerospace Sciences Meeting, Reno, NV, USA, AIAA-2007-1138
- Robinson SK** (1991) Coherent motions in the turbulent boundary layer. *Ann Rev Fluid Mech*, Vol 23, 601-639
- Robinson SK** (1991b) The kinematics of turbulent boundary layer structure. NASA Technical Memorandum 103859
- Savitzky A; Golay MJE** (1964) Smoothing and differentiation of data by simplified least squares procedures. *Anal Chem*, Vol 36, 1627-1639
- Scarano F** (2002) Iterative image deformation methods in PIV. *Meas Sci Technol*, Vol 13, R1-R19
- Scarano F; David L; Bsibsi M; Calluad D** (2005) S-PIV comparative assessment: image dewarping + misalignment correction and pinhole + geometric back projection. *Exp Fluids*, Vol 39, 257-266
- Scarano F; Elsinga GE; Bocci E; Van Oudheusden BW** (2006) Investigation of 3-D coherent structures in the turbulent cylinder wake using Tomo-PIV. 13th Int Symp on Applications of Laser Techniques to Fluid Mech, Lisbon, Portugal, paper 20.4
- Scarano F; Riethmuller ML** (2000) Advances in iterative multigrid PIV image processing. *Exp Fluids, Suppl*, S51-S60
- Scarano F; Van Oudheusden BW** (2003) Planar velocity measurements of a two-dimensional compressible wake. *Exp Fluids*, Vol 34, 430-441
- Schimpf A; Kallweit S; Richon JB** (2003) Photogrammetric particle image velocimetry. 5th Int Symp on Particle Image Velocimetry, Busan, Korea, paper 3115
- Schrijer FFJ; Scarano F; Van Oudheusden BW** (2006) Application of PIV in a Mach 7 double-ramp flow. *Exp Fluids*, Vol 41, 353-363

- Schrijer FFJ; Scarano F** (2007) Particle slip compensation in steady compressible flows. 7th Int Symp on Particle Image Velocimetry, Rome, Italy
- Schröder A; Geisler R; Elsinga GE; Scarano F; Dierksheide U** (2006) Investigation of a turbulent spot using time-resolved tomographic PIV. 13th Int Symp on Applications of Laser Techniques to Fluid Mech, Lisbon, Portugal, paper 1.4
- Schröder A; Geisler R; Elsinga GE; Scarano F; Dierksheide U** (2008) Investigation of a turbulent spot and a tripped turbulent boundary layer flow using time-resolved tomographic PIV. *Exp Fluids*, Vol 44, 305-316
- Settles GS** (2001) Schlieren and shadowgraph techniques: visualizing phenomena in transparent media. Springer, Berlin Heidelberg New York
- Smith CR** (1984) A synthesized model of the near-wall behavior in turbulent boundary layers. Proc 8th Symp on Turbulence, ed J Zakin and G Patterson, University of Missouri-Rolla, pp 299-325
- Smith CR; Metzler SP** (1983) The characteristics of low-speed streaks in the near-wall region of a turbulent boundary layer. *J Fluid Mech*, Vol 129, 27-54
- Smith CR; Walker JDA; Haidari AH; Sobrun U** (1991) On the dynamics of near-wall turbulence. *Phil Trans R Soc Lond A*, Vol 336, 131-175
- Smith MW** (1989) Flow visualization in supersonic turbulent boundary layers. PhD thesis, Princeton University, USA
- Smits AJ** (1991) Turbulent boundary-layer structure in supersonic flow. *Phil Trans R Soc Lond A*, Vol 336, 81-93
- Smits AJ; Hayakawa K; Muck KC** (1983) Constant temperature hot-wire anemometry practice in supersonic flows; Part 1: The normal wire. *Exp Fluids*, Vol 1, 83-92
- Smits AJ; Dussauge JP** (2006) Turbulent shear layers in supersonic flow, 2nd edition. Springer, New York, NY, USA
- Soloff SM; Adrian RJ; Liu Z-C** (1997) Distortion compensation for generalized stereoscopic particle image velocimetry. *Meas Sci Technol*, Vol 8, 1441-1454
- Spalart PR** (1988) Direct simulation of a turbulent boundary layer up to $Re_\theta = 1410$. *J Fluid Mech*, Vol 187, 61-98
- Spalding DB** (1961) A single formula for the law of the wall. *J Appl Mech*, Vol 28, 455-457.
- Spina EF; Donovan JF; Smits AJ** (1991) On the structure of high-Reynolds-number supersonic turbulent boundary layers. *J Fluid Mech*, Vol 222, 293-327
- Spina EF; Smits AJ; Robinson SK** (1994) The physics of supersonic boundary layers. *Ann Rev Fluid Mech*, Vol 26, 287-319
- Svizher A; Cohen J** (2006) Holographic particle image velocimetry measurements of hairpin vortices in a subcritical air channel flow. *Phys Fluids*, Vol 18, 014105
- Theodorsen T** (1952) Mechanism of turbulence. Proc 2nd Midwestern Conference on Fluid Mech, Ohio State University, Columbus, Ohio, pp. 1-19
- Timmerman BH** (1997) Holographic interferometric tomography for unsteady compressible flow. PhD thesis, Delft University of Technology, Delft, NL
- Toh S; Itano T** (2005) Interaction between a large-scale structure and near-wall structures in channel flow. *J Fluid Mech*, Vol 524, 249-262
- Tomkins CD; Adrian RJ** (2003) Spanwise structure and scale growth in turbulent boundary layers. *J Fluid Mech*, Vol 490, 37-74
- Townsend AA** (1976) The structure of turbulent shear flow. Cambridge University Press, Cambridge, UK

- Tsai RY** (1986) An efficient and accurate camera calibration technique for 3D machine vision. Proc of IEEE Conf on Computer Vision and Pattern Recognition, Miami Beach, FL, USA, 364-374
- Verhoeven D** (1993) Limited-data computed tomography algorithms for the physical sciences. Appl Optics, Vol 32, 3736-3754
- Virant M; Dracos T** (1997) 3D PTV and its application on Lagrangian motion. Meas Sci Technol, Vol 8, 1539-1552
- Watt DW; Conery DG** (1993) Computational aspects of optical tomography for fluid mechanics and combustion. 3rd ASME Symp on Exp and Num Flow Visualization, New Orleans, LA, USA, 241-251
- Westerweel J** (1993) Digital particle image velocimetry: Theory and application. PhD thesis, Delft University of Technology, Delft, The Netherlands
- Westerweel J; Scarano F** (2005) A universal detection criterion for the median test. Exp Fluids, Vol 39, 1096-1100
- White FM** (1991) Viscous fluid flow. Second edition. McGraw-Hill, New York
- Wieneke B** (2005) Stereo-PIV using self-calibration on particle images. Exp Fluids, Vol 39, 267-280
- Wieneke B** (2007) Volume self-calibration for stereo-PIV and tomographic-PIV. 7th Int. Symp. on Particle Image Velocimetry, Rome, Italy
- Wieneke B; Taylor S** (2006) Fat-sheet PIV with computation of full 3D-strain tensor using tomographic reconstruction. 13th Int Symp on Applications of Laser Techniques to Fluid Mech, Lisbon, Portugal, paper 13.1
- Willert C** (1997) Stereoscopic digital particle image velocimetry for application in wind tunnel flows. Meas Sci Technol, Vol 8, 1465-1479
- Williamson CHK** (1996) Vortex dynamics in the cylinder wake. Annu Rev Fluid Mech, Vol 28, 477-539
- Zhou J; Adrian RJ; Balachandar S; Kendall TM** (1999) Mechanisms for generating coherent packets of hairpin vortices in channel flow. J Fluid Mech, Vol 387, 353-396

List of publications

Journal articles

- Schröder A; Geisler R; Elsinga GE; Scarano F; Dierksheide U (2008) Investigation of a turbulent spot and a tripped turbulent boundary layer flow using time-resolved tomographic PIV. *Exp Fluids*, Vol 44, 305-316
- Elsinga GE; Scarano F; Wieneke B; van Oudheusden BW (2006) Tomographic particle image velocimetry. *Exp Fluids*, Vol 41, 933-947
- Elsinga GE; Van Oudheusden BW; Scarano F (2005) Evaluation of aero-optical distortion effects in PIV. *Exp Fluids*, Vol 39, 246-256
- Elsinga GE; Van Oudheusden BW; Scarano F; Watt DW (2004) Assessment and application of quantitative schlieren methods: Calibrated color schlieren and background oriented schlieren. *Exp Fluids*, Vol 36, 309-325

Conference proceedings

- Elsinga GE; Adrian RJ; van Oudheusden BW; Scarano F (2007) Tomographic-PIV investigation of a high Reynolds number turbulent boundary layer, 7th Int Symp on Particle Image Velocimetry, Rome, Italy, 2007
- Elsinga GE; Kuik DJ; van Oudheusden BW; Scarano F (2007) Investigation of the three-dimensional coherent structures in a turbulent boundary layer. 45th AIAA Aerospace Sciences Meeting, Reno, NV, USA, AIAA-2007-1305
- Humble RA; Elsinga GE; Scarano F; van Oudheusden BW (2007) Experimental investigation of the three-dimensional structure of a shock wave/turbulent boundary layer interaction. 16th Australian Fluid Mechanics Conference, Gold Coast, Australia
- Humble RA; Elsinga GE; Scarano F; van Oudheusden BW (2007) Instantaneous 3D flow organization of a shock wave/turbulent boundary layer interaction using Tomographic PIV. 37th AIAA Fluid Dynamics Conference & Exhibit, Miami, FL, USA, AIAA-2007-4112
- Scarano F; Elsinga GE (2007) Three-dimensional velocity measurements using tomographic particle image velocimetry. In: *Proceedings Int Workshop on Digital Holographic Reconstruction and Optical Tomography for Engineering Applications*, Ed: Coupland J and Lobera J. ISBN 978 0 947974 56 5
- Elsinga GE; van Oudheusden BW; Scarano F (2006) Experimental assessment of tomographic-PIV accuracy. 13th Int Symp on Laser Techniques to Fluid Mech, Lisbon, Portugal, paper 20.5
- Schröder A; Geisler R; Elsinga GE; Scarano F; Dierksheide U (2006) Investigation of a turbulent spot using time-resolved tomographic-PIV. 13th Int Symp on Applications of Laser Techniques to Fluid Mech, Lisbon, Portugal, paper 1.4
- Scarano F; Elsinga GE; Bocci E; Van Oudheusden BW (2006) Investigation of 3-D coherent structures in the turbulent cylinder wake using Tomo-PIV. 13th Int Symp on Applications of Laser Techniques to Fluid Mech, Lisbon, Portugal, paper 20.4

- Elsinga GE; Scarano F; Wieneke B; van Oudheusden BW (2005) Tomographic particle image velocimetry. 6th Int Symp on Particle Image Velocimetry, Pasadena, CA, USA
- Elsinga GE; Wieneke B; Scarano F; van Oudheusden BW (2005) Assessment of Tomo-PIV for three-dimensional flows. 6th Int Symp on Particle Image Velocimetry, Pasadena, CA, USA
- Elsinga GE; Van Oudheusden BW; Scarano F (2005) Modeling of particle imaging through shock waves. SPIE optics and photonics 2005, San Diego CA, USA, paper 5867-22
- Elsinga GE; Van Oudheusden BW; Scarano F (2005) The effect of particle image blur on the correlation map and velocity measurement in PIV. SPIE optics and photonics 2005, San Diego CA, USA, paper 5880-37
- Elsinga GE; Van Oudheusden BW; Scarano F (2005) Challenges in particle imaging through compressible flows. PIVNET II International Workshop on the Application of PIV in Compressible Flow, Delft, NL
- van der Draai RK; van Schinkel R; Telesca A; Scarano F; Elsinga GE (2005) Application of PIV in DNW industrial supersonic wind tunnel SST. PIVNET II International Workshop on the Application of PIV in Compressible Flow, Delft, NL
- van der Draai RK; van Schinkel R; Telesca A; Scarano F; Elsinga GE; Feenstra GJ (2005) Application of PIV in (local) Supersonic flows in DNW wind tunnels. 41st AIAA Joint propulsion Conference, Tucson, AZ, USA, AIAA-2005-4082
- Scarano F; Elsinga GE; van Oudheusden BW (2005) Evaluation of aero-optical distortion effects in PIV. In: Advanced Measuring Techniques for Supersonic Flow, VKI Lecture Series, Rhode-Saint Genese, Belgium
- Elsinga GE; van Oudheusden BW; Scarano F (2004) Evaluation of aero-optical distortion effects in PIV. 12th Int Symp on Applications of Laser Techniques to Fluid Mech, Lisbon, Portugal
- Elsinga GE; van Oudheusden BW; Scarano F; Watt DW (2003) Assessment and application of quantitative schlieren methods with bi-directional sensitivity: CCS and BOS. 4th Pacific Symp on Flow Visualization and Image Processing, Chamonix, France
- Watt DW; Elsinga GE; van Oudheusden BW; Scarano F (2003) Theory and application of quantitative, bidirectional color schlieren for density measurement in high speed flow. Int Symp on Optical Science and Technology, SPIE, San Diego, CA, USA

Book contributions

- Scarano F; Elsinga GE; Wieneke B (2007) Principles of Tomographic-PIV. In: Particle Image Velocimetry, 2nd edition, Ed: Raffel M, Willert C, Kompenhans J and Wereley S, Springer-Verlag, Berlin Heidelberg New York
- Schröder A; Elsinga GE; Scarano F; Dierksheide U (2007) Volume PIV. In: Particle Image Velocimetry, 2nd edition, Ed: Raffel M, Willert C, Kompenhans J and Wereley S, Springer-Verlag, Berlin Heidelberg New York
- Elsinga GE; Wieneke B; Scarano F; Schröder A (2007) Tomographic 3D-PIV and applications. In: Particle Image Velocimetry, New developments and recent applications, Ed: Schröder A and Willert C, Springer-Verlag, Berlin Heidelberg New York

Acknowledgements

First of all I would like to take this opportunity to thank my supervisors Prof. Dr. Fulvio Scarano and Dr. Bas van Oudheusden for their valuable advice and for creating the opportunity to carry out this research within the Aerodynamics group at Delft University of Technology. I much appreciate the large amount of ideas they brought up, the sharing of their knowledge and the fact that both of them were always thinking with me about the direction of the research. At the same time they allowed me freedom to explore, which I enjoyed. Moreover, they made me aware of the importance of the presentation of the results. On the organizational side, they ensured there were always enough cameras and lasers to work with.

Furthermore I am grateful to Bernd Wieneke and LaVision GmbH for the continues support throughout this project. Discussing system requirements and implementation issues with a commercial partner has been helpful and motivating and it is something I would recommend to future developers of (experimental) techniques. I would also like to acknowledge Dirk Michaelis (LaVision) for implementing the Tomographic-PIV algorithms in DaVis and speeding up the code. Moreover, LaVision GmbH has provided hardware support for all experiments presented in this thesis.

Then, I would like to thank the German Aerospace Center (DLR) at Göttingen, and in particular Dr. Andreas Schröder, for the opportunity to join in their experiments and perform time-resolved measurements of a turbulent boundary layer.

My working visit to Prof. Dr. R.J. Adrian and his group at Arizona State University has contributed importantly to my understanding of coherent motion in boundary layers. I am grateful for, and have very much enjoyed, their cooperation, hospitality and companionship.

I thank Ray Humble and Dirk Jan Kuik for their contributions in setting up and performing the boundary layer experiments in Delft and for the discussions on the results. Furthermore, I thank Eric de Keizer, Frits Donker Duyvis and Peter Duyndam for the technical support in these experiments. Nico van Beek is acknowledged for the computer assistance.

During the research I spend much time with my colleague Ferry Schrijer. I wish to thank him for all his scientific, non-scientific and practical help, the coffees and the music. Furthermore, it was a pleasure organizing the Agora Aerodynamika-talks and BBQ together and initially also with David Lentink.

I would like to thank my family and friends for their interest, companionship and encouragements throughout the years.

Finally I want to express my sincere gratitude to Suzanne Petiet for her love and for her understanding and support in stressful times.

The work was sponsored by the Dutch Technology Foundation STW under the *VIDI-Innovation Impulse* program, Grant DLR.6198. My working visit was financially supported by Arizona State University.

Gerrit Elsinga
Melbourne, April 2008

Curriculum Vitae

Gerrit Einte Elsinga was born on April 22, 1978 in Groenlo, The Netherlands. After finishing secondary school (VWO) at the Scholengemeenschap Marianum in Groenlo in 1996, he started studying Aerospace Engineering at Delft University of Technology obtaining his Master of Science degree with Honours in 2003. The Master thesis work was carried out at the Aerodynamics Group and concerned the development and assessment of quantitative schlieren methods for application to supersonic flows. In September 2003 he started his Ph.D. research within the same group under supervision of Dr. F. Scarano and Dr. B.W. van Oudheusden. The research topic was the development of a three-dimensional velocimetry technique for turbulence research and the investigation of the coherent structures in turbulent boundary layers. The results of this work are presented in this thesis. The development of the experimental technique was performed in a collaboration between the Aerodynamics Group at Delft University of Technology and LaVision GmbH, Göttingen, Germany. As part of this research he paid a short working visit to DLR Göttingen, Germany, in April 2006. And in 2007 he spent one month as a visiting scholar in the group of Prof. R.J. Adrian at Arizona State University.

In the period of his Ph.D. research, he also participated in two research projects involving the implementation of PIV in the SST large-scale supersonic wind tunnel of the German-Dutch Wind Tunnel Association DNW and the measurement and characterization of the wake vortex behind a generic aircraft model in a towing tank as part of the European project FARWAKE.

He is furthermore a member of the Scientific Advisory Committee of the 13th International Symposium on Applications of Laser Techniques to Fluid Mechanics, Lisbon, Portugal, 2008.